PERFORMANCE OF GFRP-RC CIRCULAR COLUMNS UNDER MONOTONIC LOADS

By

SHISIR BARUA

A Thesis submitted to the Faculty of Graduate Studies of

The University of Manitoba

in partial fulfillment of the requirements of the degree of

MASTER OF SCIENCE

Department of Civil Engineering

University of Manitoba

Winnipeg, MB, Canada

ABSTRACT

In this study, a total of thirteen full-scale reinforced concrete (RC) circular columns were constructed and tested to failure. The columns were divided into Series I and Series II, based on the slenderness ratio. All columns had a 355-mm diameter and were reinforced with six longitudinal bars and continuous spirals. Series I included seven short columns, 1,750-mm long, while Series II included six slender columns, 2,450-mm long. The test variables were reinforcement type (GFRP and steel), GFRP spiral pitch (50 and 85 mm), and eccentricity of axial load (0, 30, 60, and 120 mm) in addition to flexural loading. In each series, one steel-RC column having 85-mm spiral pitch was tested under an eccentric axial load with 30-mm eccentricity. The columns were tested to failure under either axial or four-point bending loads. The obtained capacity of the GFRP-RC short column tested with 30-mm eccentricity was approximately 17% less than the steel-RC counterpart. However, the GFRP-RC short column tested with a lesser spiral pitch (50 mm) exhibited approximately 10% more capacity than that with a larger pitch (85 mm). However, for the slender columns with same eccentricity (30 mm), the obtained capacity was approximately 3% higher than the steel-RC counterpart.

Interaction diagrams for GFRP-RC short and slender circular columns were developed from experimental results in which axial capacity decreased and flexural capacity increased until the inflection point was reached, then both axial and flexural capacity decreased simultaneously. For short columns (Series I), as the axial load eccentricity increased from 0 to 30, 90 then to 120 mm, the axial capacity decreased by 32, 39, and 70% from the capacity of the concentric column, respectively. Similarly, for slender columns (Series II), these reduction percentages were 30, 37, and 70% from the capacity of the concentric column, respectively. As an effect of slenderness ratio, the GFRP-RC slender columns showed a peak load of approximately 21 to 25% less than the short counterpart columns.

To my beloved parents and sister

Thanks for your continuous prayer, support and care

ACKNOWLEDGEMENTS

I would like to take this opportunity to express my sincere gratitude to Dr. Ehab El-Salakawy, Ph.D., P.Eng., Professor and Canada Research Chair in Durability and Modernization of Civil Structures (2006-2016), Department of Civil Engineering, University of Manitoba, for his continuous guidance and encouragement during this program. I would also like to thank him for all I have learned from him, and for encouraging and helping me to shape my ideas and interests.

I would like to express my deep gratitude to my colleagues, whose suggestions for my work were phenomenal.

I would like to gratefully acknowledge the financial support received from the Natural Science and Engineering Research Council of Canada (NSERC) as well as the government of Manitoba through Manitoba Graduate Scholarship (MGS) program.

The outcome of this project would not have been possible without the help and assistance of the W. R. McQuade structures laboratory technical staff, Dr. Chad Klowak and Mr. Samuel Abraha.

Thanks to my special friend Syed Abdullah Mohit for being there for me, during both good and bad times.

Lastly, and most importantly, I would like to thank my parents and my sister. Words cannot describe the sacrifices my parents have made for me, to ensure a bright future; without them, I would not have been here.

TABLE OF CONTENTS

LIST OF TABLES

LIST OF FIGURES

LIST OF NOTATIONS

A_b	Area of GFRP rebar, mm^2
A_c	Area of core of spirally reinforced compression member, mm^2
A_F	Total area of longitudinal GFRP reinforcement, mm^2
A_g	Gross area of cross-section, mm^2
A_{ft}	Total area of longitudinal GFRP tension reinforcement, mm^2
A_{sp}	Cross-sectional area of spiral reinforcement, mm^2
A_{st}	Total area of longitudinal steel reinforcement, mm^2
C_b	Distance from extreme compression fibre to neutral axis at balanced condition, mm
d	Effective depth of section, mm
D	Section diameter for circular column, mm
D_c	Core diameter of spirally reinforced compression member, mm
D_r	The diameter of the circle passing through the centers of the longitudinal bars, mm
e	Eccentricity, mm
E_c	Modulus of elasticity of concrete, GPa
E_F	Modulus of elasticity of GFRP reinforcement, GPa
E_s	Modulus of elasticity of steel bar, GPa
f_c'	Specified compressive strength of concrete, MPa
f_f	Average stress in FRP tension reinforcement, MPa
f_y	Specified yield strength of steel reinforcement, MPa
f_{fb}	Average stress in the GFRP tension reinforcement at balanced condition, MPa
f_{Fh}	Design stress in the spiral reinforcement in a column, MPa

f_{Fu}	Ultimate strength of GFRP reinforcement, MPa
k	Effective length factor
K_n	Normalized axial force
l_u	Unsupported length, mm
M_1	Smaller factored end moment on a compression member associated with the same loading case as M_2 (positive if member is bent in single curvature, negative if bent in double curvature)
M_2	Larger factored end moment on a compression member (always positive)
M_{n1}	Primary moment or nominal bending moment due to initial eccentricity, kN.m
M_{n2}	Secondary moment or nominal bending moment due to additional lateral displacement, kN.m
M_n	Total nominal moment, kN.m
P	Applied concentrated load, kN
P_f	Factored axial load, kN
P_n	Nominal axial force or peak load, kN
P_o	Nominal unconfined axial load capacity, kN
$P_{r,max}$	Maximum factored axial load resistance of compression member, kN
P_{ro}	Factored axial load resistance of column at zero eccentricity, kN
r	Radius of gyration, mm
R	Section radius of circular cross section, mm
R_n	Normalized bending moment
s	Spiral pitch, mm

$\bar{y}$	Distance of the C.G. of concrete area under compression from the center of cross section of the column, mm
α_1	Ratio of average stress in rectangular compression block to the specified concrete strength
β_1	Ratio of depth of rectangular stress block to depth of neutral axis
δ_n	Mid-height lateral displacement at peak load, mm
Δ_n	Total axial displacement at peak load, mm
ε_y	Yield strain of steel bars
ε_{cu}	Ultimate strain of concrete
ε_{fb}	Average strain in the GFRP tension reinforcement at balanced condition
ε_{Fu}	Ultimate strain of GFRP reinforcement
ρ_f	Percentage of longitudinal reinforcement ratio
ρ_s	Ratio of volume of steel spiral reinforcement to total volume of core confined by the spiral (measured out-to-out of spirals)
ρ_{fb}	Balanced reinforcement ratio
ρ_{Fs}	Ratio of volume of spiral FRP reinforcement to total volume of core (center-to-center of spirals) of a spirally reinforced compression member
ρ_{ft}	Longitudinal FRP tension reinforcement ratio
θ	Angle created at the centre of column cross section by area under compression at, rad
θ_b	Angle created at the centre of column cross section by area under compression at balanced condition, rad
ϕ_c	Material resistance factor for concrete

ϕ_F Material resistance factor for FRP reinforcement

ϕ_s Material resistance factor for steel reinforcement

CHAPTER 1 – INTRODUCTION

1.1 BACKGROUND AND PROBLEM DEFINITION

Reinforced concrete (RC) circular columns often used in civil structures because of their pleasant appearance, higher confinement efficiency, uniform strength, and stiffness along all directions. Usually, circular columns are reinforced with conventional steel bars and spirals. The major problem with steel-RC columns is the reinforcement corrosion when exposed to the harsh or marine environment. This results in deterioration of structures, which will require costly repair work or even replacement. Estimates indicate that the United States spends billions of dollars annually to repair and replace bridge substructures such as pier columns ($2 billion) and marine piling systems ($1 billion) (NACE 2013). Corrosion of steel reinforcement reduces the structural strength and ductility of RC columns, which eventually decreases the service life of the whole structure. In North America, harsh environments such as freeze-thaw cycle, wet-dry cycles, marine conditions, and the use of de-icing salts and chemicals accelerate the corrosion process of steel reinforcement resulting in gradual deterioration that decreases the life expectancy of RC structures. The use of glass fibre-reinforced polymer (GFRP) reinforcement in RC structures becomes popular because of many desirable properties that are superior to those of conventional steel. The benefits of using GFRP reinforcement include high strength-to-weight ratio, high resistance to corrosion, electromagnetic transparency, and free-form tailored design characteristics. Moreover, availability and cost-effectiveness of GFRP reinforcement make it an ideal alternative to steel as a construction material.

Significant research and field applications carried out in the past two decades have proven that GFRP reinforcements can be effectively used in RC structures instead of steel to avoid the corrosion of steel (Rizkalla et al. 2003; El-Salakawy et al. 2003; Benmokrane et al. 2007). Recent years have seen significant research work on GFRP-RC continuous beams, beam-column joints, and slab-column connections (Mahmoud and El-Salakawy 2016; Ghomi and El-Salakawy 2016, El-Gendy and El-Salakawy 2018). However, the behavior of GFRP-RC circular columns under axial and flexural loads has not yet fully defined. So, valuable investigations are required in this area to establish appropriate design provisions in codes and guidelines for GFRP-RC compression members.

In general, structural behaviour of RC circular-shaped columns subjected to axial and flexural loads are different from square or rectangular shaped columns in terms of stress distribution and confinement efficiency. The confinement provided by ties or spirals to the concrete core is activated after the concrete cover is cracked or spalled off. Usually, a tied column exhibits some deformability beyond the peak load, but there is not much strength gain (Park and Paulay 1975). On the other hand, a spiral column exhibits a significant strength gain as well as deformability after the peak load. This can be attributed to the uniform confinement applied by continuous spirals, while the confinement is mainly applied at corners in square and rectangular columns (Saatcioglu and Razvi 2002), which results in less confinement efficiency. Also, the relatively smaller pitch of spiral reinforcement controls the buckling of longitudinal reinforcement. On the other hand, replacing steel with GFRP reinforcement in circular columns may affect the overall structural performance of the column because of their different material properties. GFRP reinforcing materials possess linear-elastic stress-strain behavior up to the failure, whereas steel yields and exhibits a well-defined yielding plateau, which will affect the failure mode for RC columns and the efficiency of confinement. Besides, GFRP materials can sustain higher tensile stresses and strain than the steel, which will eventually contribute to the column's capacity and deformability. However, GFRP bars have lower compressive strength and modulus of elasticity than steel, which raise concerns among design engineers on using GFRP bars in compression members. Hence, research is required to evaluate the structural performance of GFRP-RC columns. In North America, design standards and guidelines for steel-RC structures have well-established design provisions, whereas, standards and guidelines for FRP-RC structures are still under development and continuous update. Steel-RC design standards include axial load-bending moment interaction diagrams that are often used by engineers to efficiently design steel-RC circular columns. However, due to the different material properties of GFRP materials, as mentioned earlier, these diagrams cannot be used for the design of GFRP-RC circular columns. Therefore, axial load-bending moment interaction diagrams for GFRP-RC circular columns need to be developed through research work.

1.2 RESEARCH SIGNIFICANCE

Due to limited research data, current American design guideline ACI 440.1R-15 (ACI 2015) for FRP-RC structures do not recommend using FRP longitudinal bars in compression members and encourage that further research is needed for FRP-RC columns. Also, the Canadian standards for FRP-RC buildings, CSA S806-12 (CSA 2017), and bridges, CSA S6-19 (CSA 2019a), allow the use of FRP longitudinal bars in RC short columns but suggest neglecting their contribution to compressive strength for columns subject to either concentric or eccentric axial loads. Furthermore, the Canadian standards for FRP-RC buildings (CSA 2017) do not permit using FRP longitudinal reinforcement in slender columns. This research aims at evaluating the performance of full-scale GFRP-RC circular short and slender columns under axial and flexural loads. This study will contribute to fill research gaps and to better understand the behaviour of GFRP-RC short and slender columns with circular sections under different loading conditions.

1.3 RESEARCH OBJECTIVE

The main objectives of this study are to:

- Investigate the structural performance of GFRP-RC short and slender circular columns in terms of load-carrying capacity, axial and lateral displacements, slenderness effects, strains in GFRP bars, spirals, and concrete, and mode of failure under axial and flexural loads.
- Develop axial load-bending moment interaction diagram from experimental results for GFRP-RC short and slender circular columns.

The following specific parameters were investigated in this study to achieve the above main objectives.

- Type of reinforcing materials (GFRP or steel).
- Slenderness ratio (20 or 28).
- Spiral pitch (50 or 85-mm).
- Type of loading (Axial or flexural load)
- Axial load's eccentricity-to-column diameter ratio (0, 0.085, 0.17, or 0.34).

1.4 SCOPE OF WORK

The scope of this study is limited to testing full-scale circular RC short and slender columns under axial or four-point bending loads until failure. Normal strength concrete of approximately 35 to 40 MPa is used in the construction of all columns. Only two slenderness ratios were considered 20 and 28. All test columns, except control ones, were reinforced with sand-coated GFRP bars and continuous spirals. Control specimens were reinforced with deformed steel bars and continuous spirals.

1.5 METHODOLOGY

Based on the objectives mentioned in the previous sections, the experimental program divided into two series, Series I and Series II, based on the slenderness ratio (20 or 28). All columns had a 355-mm diameter and were reinforced with six longitudinal bars and continuous spirals. Series I included seven short columns, 1,750-mm long, while Series II included six slender columns, 2,450-mm long. The test variables were reinforcement type (GFRP and steel), GFRP spiral pitch (50 and 85 mm), and eccentricity of axial load (0, 30, 60, and 120 mm) in addition to flexural loading. The columns were tested to failure under either axial or four-point bending loads.

Performance of all tested columns was evaluated in terms of load-carrying capacity, axial and lateral displacements, slenderness effects, strains in GFRP bars, spirals, and concrete, and mode of failure. Also, from the experimental results, normalized axial load-bending moment interaction diagrams were developed for circular GFRP-RC short and slender columns.

1.6 THESIS OUTLINE

This thesis comprises six chapters as follows:

Chapter 1 introduces problem definition, research objectives, scope, and the methodology that was followed to achieve the research objectives.

Chapter 2 provides the information about FRP composites and their constituent materials, mechanical properties of FRP reinforcements, and a review of previous research on GFRP-RC columns subjected to axial and/or flexural loads.

Chapter 3 illustrates the experimental program with schematic drawings and reinforcement details of test columns, material properties, and construction steps. It also describes the instrumentation, test set up, and testing procedure.

Chapter 4 and **Chapter 5** present the analysis and discussion of the experimental results of the test Series I and II. The structural performance based on cracks pattern, load-carrying capacity, axial and lateral displacements, slenderness effects, strains in GFRP bars, spirals and concrete, and mode of failure was evaluated and compared with one another to understand the effect of the variables on the performance of test columns.

Chapter 6 presents significant findings and conclusions regarding the test results. Also, recommendations for future work are included in this chapter.

The design of the test columns of Series I and II are demonstrated in Appendices A, B, and C, using the provisions of code and guideline as applicable.

CAHPTER 2 – LITERATURE REVIEW

2.1 GENERAL

Columns are the main supporting and load transferring elements in any RC structure. All codes and guidelines handle the design of RC columns with great care to ensure a gradual failure. Steel is utilized for concrete reinforcement due to its favorable properties, especially its plasticity and yielding, which are the primary source for ductility under any loading condition. Recently, more increasing troubles and detrimental effects of steel corrosion noticed for steel-RC structures, around which economic and safety concerns arise. Treatment of steel bars against corrosion was not found as a beneficial solution, neither economically nor technically.

On the other hand, Fibre-Reinforced Polymer (FRP) materials were introduced to the construction industry, which gained engineers' attention due to its non-corrodible nature, lightweight, and good mechanical properties. During the last two decades, a significant research effort was given to studying the properties of FRP materials and FRP-RC members. However, the current American design guideline ACI 440.1R-15 (ACI 2015) for FRP-RC structures does not recommend using FRP longitudinal bars in RC columns and advises that further research needed for FRP-RC columns. Also, the Canadian standards for FRP-RC buildings, CSA S806-12 (CSA 2017), and bridges, CSA S6-19 (CSA 2019a), suggest neglecting the contribution of FRP bars to the compressive strength for short columns, while do not permit using them in RC slender columns. More research is needed to have a better understanding of the behaviour of FRP-RC columns. In this chapter, constituents and mechanical properties of FRP reinforcements are presented. Also, a review of previous research on GFRP-RC columns subjected to axial and flexural loads are summarized in this chapter.

2.2 FIBRE-REINFORCED POLYMERS (FRPs)

Fibre-Reinforced Polymers (FRPs) are composite materials comprising of continuous fibres impregnated into another material called the matrix or the resin, then hardened into a specific shape and characteristics. Also, other materials are included to complete the process, such as additives and fillers. The properties of the FRP products are dependent on the properties of each component, as well as the manufacturing process (ACI 2015). Four types of FRP reinforcement are commercially produced for the construction industry: Glass-fibre reinforced polymers (GFRP); carbon fiber reinforced polymers (CFRP); aramid fiber reinforced polymers (AFRP), and basalt fiber reinforced polymers (BFRP).

Glass fiber reinforced polymers (GFRP) are more favorable for internal reinforcement. Its relatively low cost, high strain capacity, high chemical resistance, and sound insulation properties concerning the other available types are the reasons why GFRP is more preferred in the construction industry. Hence, GFRP reinforcement is used in this study. It is worth mentioning also that there are some disadvantages also concerning GFRP, which are its relatively low modulus of elasticity, high density, high susceptibility to creep rupture and low fatigue strength (ACI 2015).

2.2.1 Fibres

High strength and stiffness, toughness, durability, and low cost are the main characteristics of the fibres used in manufacturing FRP composite materials. The performance of fibres depends on the fibre length, cross-sectional shape, and chemical composition. Different types, cross-sectional shapes, and sizes of fibres are available. To increase the bond strength fibres are coated with coupling agents (the chemical compound which provides a bond between dissimilar materials). The most common fibres used are aramid, carbon, and glass fibres. Other commercially available fibres are boron, nylon, polyethylene, polypropylene, and basalt. Aramid fibres provide high tensile strength and high stiffness. They have low density and good resistance to hydrocarbon, solvents, lubricants, wear, and vibrations. However, the drawbacks are aramid fibres are difficult to impregnate by the resins, low resistance at high temperature, sensitive to UV rays and absorb moisture at elevated temperatures. Carbon fibres have high resistance to tension, compression, and fatigue. They exhibit excellent resistance to moisture and chemical products and have high stiffness and low coefficient of thermal expansion.

On the contrary, carbon fibres are expensive and difficult for impregnation by the resins. They are also sensitive to impact and abrasion and have high electrical and thermal conductivity. As a result, they are susceptible to galvanic corrosion. Comparing other types, glass fibres are inexpensive and have high tensile strength. They are highly chemically resistant and shows excellent impregnation when embedded into the resins.

Moreover, glass fibres are excellent in impact resistance and have very low thermal and magnetic conductivity. Four types of glass fibres are available, namely type E (electricity neutral), type S (high strength), type C (chemically resistant), type AR (alkali resistance). Among all of them, type E (electricity neutral) are most commonly used. The problems associated with glass fibres are higher density, weak stiffness, lower fatigue resistance, sensitivity to abrasion, and corrosion due to alkaline solutions and moisture absorption. Basalt fibre is relatively new material. It has a similar chemical composition as glass fibre but shows better strength characteristics. Glass fiber-reinforced polymers bars are commonly used in the construction industry due to their desirable properties in addition to relatively low cost compared to other FRP products (carbon and aramid).

2.2.2 Resin

The physical and thermal properties of the matrix significantly affect the final mechanical properties as well as the manufacturing process of FRP composites. So, the selection of the proper matrix is vital for the manufacture of FRP composites. The matrix should be able to develop a higher ultimate strain than the fibres to attain full strength of the fibres (Phillips, 1989). The resin provides a coating to the fibres to resist corrosion and protects from mechanical abrasion and environmental damage. Other significant roles of the matrix are the transfer of inter-laminar and in-plane shear in the composite, and provision of lateral support to fibres against buckling when subjected to compressive loads (ACI 1995). Two major groups of resins available are thermoset and thermoplastic. When heated, thermoplastic resins become soft and may be moulded into the desired shape while in a semi-fluid state. They become rigid when cooled.

On the other hand, thermoset resins are usually liquids in their original form. These thermosetting resins are cured with a catalyst, heat, or a combination of the two when used to produce finished products. However, solid thermoset resins cannot be converted back to their original shape once cured. In general, thermoset resins are more commonly used for the manufacturing of FRP products. The most common thermosetting resins used in the composites industry are unsaturated polyesters, epoxies, vinyl esters, and phenolics.

2.3 MECHANICAL PROPERTIES OF FRP REINFORCEMENT

2.3.1 Tensile Strength

Tensile behaviour of FRP composites greatly depends on its unidirectional nature as the fibres, which are the source of strength, are oriented in the longitudinal direction only. FRP composites exhibit linear elastic behaviour up to failure whereas steel reinforcement shows a yielding plateau in the stress-strain diagram as shown in Fig. 2.1, and thus, FRP reinforcing materials are known for their relative brittleness comparing to steel. However, FRP composites have much higher tensile strength than regular steel. The axial stiffness of GFRP is much lower, while CFRP possesses similar axial stiffness to steel (Fig. 2.1). However, GFRP has higher strain capacity comparing to CFRP, which is more beneficial in terms of showing signs of degradation before failure. Tensile properties of FRP materials with same constituents may vary according to the fibre volume fraction and manufacturing process. Therefore, the final properties of FRP reinforcements should be provided by the manufacturer. No bends can be applied to the finished products if thermosetting resins are used. However, bent bars and ties can be shaped during manufacturing, but a reduction in tensile strength of around 40 to 50% shall be expected at the bend portion due to stress concentration (ACI 2015).

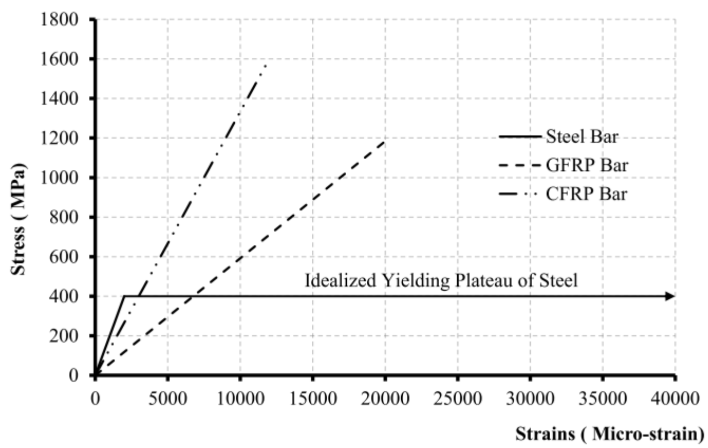

Fig. 2.1: Schematic stress-strain relationship of FRP and steel reinforcement

2.3.2 Compressive Strength

The compressive strength of FRP materials is much lower than their tensile strength as FRP materials tend to buckle under compression, either as a whole element or as individual fibres. Some recent studies suggested reducing the value of compressive strength of FRP materials to

50% of its tensile strength while keeping the modulus of elasticity same under both cases of loading (Deitz et al. 2003). Tavassoli et al. (2015) also concluded similar observations from compression tests on two types of GFRP reinforcement, sand-coated and deformed bars, with free length equal to the spiral pitch of the column specimens to be studied within the same program. Shear Strength FRP materials are well known for their anisotropic nature. Therefore, FRP bars possess relatively weak shear strength because there is usually no reinforcement across layers and the inter-laminar shear strength is governed by the relatively weak polymer matrix. Also, interface problem between vinyl ester resin and carbon fiber was found and resulted in very low inter-laminar shear strength compared to glass fiber (Xiao 2004). Moreover, carbon fibers are more brittle than glass fibers with ultimate strain of 1.32% and 2.56% for carbon and glass fibers, respectively. However, orientation of the fibers in an off-axis direction across the layers of fiber will increase the shear resistance, depending upon the degree of offset. For FRP bars, this can be accomplished by braiding or winding fibers transverse to the main fibers. Off-axis fibers can also be placed in the pultrusion process by introducing a continuous strand mat in the roving or mat creel. Like all other mechanical properties, shear strength of FRP materials should be provided by the manufacturer (ACI 2015). Recently, standard test methods for measuring the compressive strength of FRP bars has been published (CSA 2019b; ASTM 2015 & 2016); however, current FRP design codes do not provide enough guidance, if any, to design FRP bars in compression members.

2.3.3 Bond Strength

Physical and mechanical properties of the FRP bars, as well as the environmental conditions, are all primary factors impacting the bond strength of FRP materials with concrete. For GFRP bars, the surface can be prepared by chemicals to transfer bond stress by adhesion (ACI 2015), sand-coating to transfer bond by friction, or ribbing to have bond transferred mechanically. Generally, bond strength of AFRP and GFRP was reported to be significantly less than the bond strength of steel reinforcement, which was attributed to another finding that bond strength is dependent upon the modulus of elasticity (Mosley et al. 2008). However, with recent developments in the production of FRP materials, bond strength similar to steel reinforcement was found by Alves et al. (2010) for GFRP reinforcement under different environmental conditions. Usually, FRP bars with different diameters would have different bond properties.

2.4 PLAIN CONCRETE BEHAVIOUR

In the last century, extensive research has been carried out on the axial behaviour of plain concrete and was found to be greatly dependent on the specifications of concrete. The water-cement ratio, cement, and aggregate characteristics, concrete unit weight, type of curing and age, all play a significant role in the behaviour (Carreira and Chu 1985). The plain concrete behaviour is best understood from the axial compression of concrete cylinders taken from the concrete mix. Concrete gains most of its ultimate strength in the first 28 days after construction. During that time, the type of curing system will affect the overall strength. The testing of the cylinders at 28 days will result in a stress-strain plot that will rise to a point where ultimate strength is reached and then descend quickly when the concrete crushes.

2.5 BEHAVIOUR OF STEEL-RC COLUMNS UNDER AXIAL AND FLEXURAL LOADS

For an axially-loaded steel-RC column, whether tied or spiral, the axial load-axial deformation relation exhibits an ascending portion up to a peak load, *Po*, which is expressed as (ACI 2014):

$$P_o = 0.85 f_c' \left(A_g - A_{st}\right) + f_y A_{st} \qquad \text{Eq. 2.1}$$

where f_c' is the concrete compressive strength from cylinder tests, A_g is the gross cross-sectional area, A_{st} is the area of longitudinal reinforcement and f_y is the yield strength of that reinforcement. The factor 0.85 is introduced to account for the difference between the shapes and sizes of the column and cylinders tested for compressive strength (Park and Paulay 1975). The failure of steel-RC columns under axial loading is usually preceded by spalling of concrete cover, usually at peak load, especially for normal-strength concrete (NSC) columns. In high-strength concrete (HSC) columns, however, the spalling of concrete cover may occur earlier compared to the normal strength concrete (NSC), as the transverse reinforcement creates a plane of weakness between the concrete cover and the core, resulting in early spalling of the concrete cover. Failure is often commenced by buckling of the longitudinal reinforcement for the square and rectangular columns, while in spirally-reinforced columns, failure commences by crushing of the concrete core as the small spiral pitch can secure the longitudinal reinforcement against buckling (Park and Paulay 1975).

It is rare for columns to be subjected to pure axial loading. The load applied from beams and slabs on columns will usually involve some eccentricity. Also, the frame action and continuity of the structure results in some moment on columns. The combination of an axial load P_u and bending moment M_u is equivalent to a load P_u applied at eccentricity $e = M_u/P_u$. The axial load capacity and moment capacity of eccentrically loaded columns are best represented by axial load-bending moment interaction diagram, as shown in Fig. 2.2. To develop such diagram, a number of assumptions are usually considered by the different design codes for steel-RC structures such as: (1) plane sections remain plane under bending, so that the strain in concrete and reinforcement is proportional to the distance from the neutral axis; (2) there is a perfect bond between the reinforcement and concrete; (3) the tension strength of concrete can be neglected; (4) failure of concrete is characterized by reaching a limiting value of 0.003 and 0.0035 as considered by ACI 318-14 (ACI 2014) and CSA A23.3-14 (CSA 2014), respectively; and (5) idealized stress-strain behaviour of steel is considered, in which the strain keeps increasing without any strain hardening once the steel has yielded.

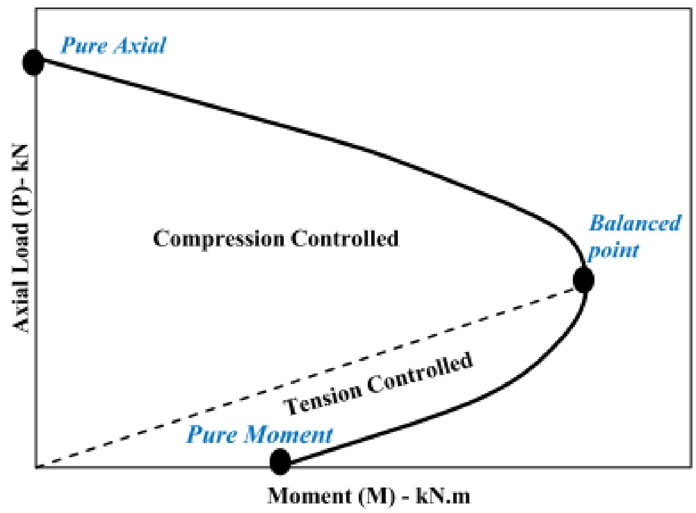

Fig. 2.2: Axial load-bending moment interaction diagram for a steel-RC column

Based on the aforementioned assumptions, the axial load-bending moment interaction diagram can be developed. The hypothetical case of "balanced failure" is usually located on the diagram, in which the concrete reaches its limiting strain at the same time when steel is yielded. The axial load capacity at such hypothetical case is denoted as P_b, or balanced load capacity. The behaviour of an eccentrically-loaded steel-RC column may depend on the eccentricity, that is, if the eccentricity is lower than the eccentricity of the balanced case, or $P_u > P_b$, the column may exhibit a compression-controlled failure, characterized by concrete crushing in the compression zone and a possibility for longitudinal bars buckling, before the longitudinal bars in tension zone yield. On the other hand, if the eccentricity is higher than the eccentricity of the balanced case, or $P_u < P_b$, a tension-controlled failure may occur, in which the longitudinal bars in tension zone yield before the concrete in the compression zone reaches the limiting strain. In practice, the tension-controlled type of failure is more favorable as it offers more ductility, while the compression-controlled type is more sudden and brittle (Park and Paulay 1975; Wight and MacGregor 2012).

2.6 BEHAVIOUR OF FRP-RC COLUMNS

2.6.1 Behaviour of FRP-RC Columns Under Concentric Loads

The low compressive strength of FRP material compared to its tensile strength was a major concern regarding adopting FRP in compression members. One of the earliest studies regarding replacing steel reinforcement with FRP was the one carried out by Alsayed et al. (1999), who concluded that a reduction of ultimate axial capacity equal to 13 and 10% was observed when steel bars were replaced by GFRP longitudinal and lateral reinforcement, respectively. Similar conclusion was reached by Lotfy (2010) who stated that using steel as longitudinal reinforcement had the advantages of more ductility and higher ultimate load compared to GFRP-RC counterpart. De Luca et al. (2010) found no harm to the behaviour of RC columns by longitudinal GFRP bars, though, the contribution of the GFRP bars to the column capacity was found to be negligible. Lotfy (2010) concluded that GFRP bars can be used as an alternative for steel longitudinal reinforcement, especially if the column was cast using high strength concrete and closely spaced stirrups. The peak load of circular GFRP-RC column specimens tested by Afifi et al. (2014) was reported to be 7% lower than the steel-RC counterparts. They also added that the contribution of GFRP bars to the axial capacity ranged between 5 to 10%. Pantelides et al. (2013) also reported that the axial load capacity of hybrid circular columns (longitudinal steel and GFRP spirals), and all-GFRP-RC columns were 87 and 84%, of the all-steel-RC columns' capacity, respectively. Nevertheless, when subjected to corrosive conditions, corroded hybrid columns exhibited similar axial capacity and ductility to the corroded all-steel columns, and the all-GFRP-RC specimens performed in a more ductile manner than the all-steel counterparts. Even with FRP as confinement reinforcement, the columns reinforced longitudinally with steel bars still need an extra 10 mm over the usual cover to avoid corrosion and exhibit acceptable performance in terms of strength and ductility (Tobbi et al. 2014). The feasibility of incorporating FRP as reinforcement for axially-loaded RC columns was also proven through the study conducted by that study. Moreover, Tobbi et al. (2012) found the contribution of GFRP longitudinal bars to the column capacity to be similar to the contribution of the steel bars in steel-RC specimens, which implied that GFRP bars could be used in compression members as long as adequate confinement is provided. Mohamed et al. (2014) also proved from tests carried out on circular FRP-RC columns that the GFRP as well as CFRP bars had a considerable contribution in resisting compressive stresses, even after the crushing of concrete, by reaching a compressive strain up to 0.4% and 0.7%, respectively. It was concluded by Brown (2015), that the use of GFRP longitudinal and transverse reinforcement in compression members instead of traditional steel reinforcement is technically and financially viable. Nevertheless, the replacement of steel reinforcement with GFRP one resulted in a lower axial capacity for the tested RC columns.

Lotfy (2010) reported that increasing the longitudinal reinforcement ratio for GFRP-RC specimens resulted in an increase of ductility, toughness, ultimate load, ultimate strain and initial cracking load of the columns. Moreover, more effectiveness was observed for increasing longitudinal GFRP reinforcement ratio from 0.723 to 1.08% rather than from1.08 to 1.45%, in terms of increasing ultimate load. Increasing GFRP longitudinal reinforcement ratio was found by Afifi et al. (2014) to have a significant effect on the mode of failure, resulting in a more ductile failure. However, a slight effect on the strength gain was observed. Tobbi et al. (2014) stated that the longitudinal reinforcement ratio was effective for FRP-RC specimens, especially in the pre-peak phase, resulting in an increase for the peak load. Karim et al. (2017) concluded that longitudinal GFRP bars improved the first and second peak loads of GFRP spirally-reinforced concrete columns, ductility and confined concrete strength of the GFRP-RC specimens. This was attributed to the longitudinal bars' effect, reducing the area of unconfined concrete core and increasing the hoop strain in the spirals, particularly for the specimens with large GFRP spiral pitch. Prachasaree et al. (2015) reported that the amount of GFRP longitudinal and lateral reinforcement slightly affected the columns' strength. De Luca et al. (2010) concluded from testing columns reinforced longitudinally with two different types of surface prepared bars, ribbed and sand coated, that GFRP bars of comparable quality exhibit similar behaviour when used in RC columns.

Regarding the behaviour and modes of failure, De Luca et al. (2010) reported that when the longitudinal reinforcement ratio is kept as 1.0%, the behaviour of steel as well as GFRP-RC columns is very similar**,** while the main difference is the failure mechanism. For instance, the steel RC specimen failed due to buckling of the longitudinal bars, whereas the GFRP-RC specimens exhibited higher axial strains than steel-RC counterpart and crushing of the concrete core occurred at failure. Similar findings were found by Tobbi et al. (2014), who reported that the failure of FRP-RC columns involved buckling or crushing of FRP longitudinal bars and rupture of the FRP ties, while for the steel-RC columns excessive buckling of the steel bars triggered the failure of those specimens. It was also added that FRP-RC specimens experienced less axial strain by 30% with respect to the columns longitudinally reinforced with same ratio of steel. Mohamed et al. (2014) concluded that up to 85% of the peak loads, steel, GFRP and CFRP-RC columns exhibited quite similar behaviour. Afifi et al. (2014) also observed similar ascending branch of the load-strain relationship for both steel and GFRP-RC column specimens up to 85% of their peak loads. Pantelides et al. (2013) observed the failure modes for circular spirally reinforced columns, in which the all-steel control columns failed by buckling of the longitudinal steel bars, while for all-steel corroded column the failure was also accompanied by rupture of steel spirals. The failure of all hybrid columns was triggered by the buckling of the steel bars, with shorter length though, followed by tensile rupture of the GFRP spirals. Buckling and compressive rupture of GFRP bars, and tensile rupture of GFRP spirals were the main remarks of the failure mode of the all-GFRP columns. Afifi et al. (2014) related the failure of the GFRP-RC specimens to its confinement. For instance, longitudinal bars buckling controlled the mode of failure for the poorly confined specimens, while crushing of the concrete core and rupture of the GFRP spirals triggered the failure for the well confined specimens.

Furthermore, Tobbi et al. (2014) related the mode of failure of FRP-RC specimens to the confinement degree, type and configuration of transverse reinforcement. The GFRP-RC specimens with lower confinement volumetric ratio suffered from tie slippage, which resulted in significant strength degradation prior to failure, while this was not the case for the well confined specimens, which failed by the successive crushing of longitudinal GFRP bars. In addition, tie rupture was observed for the specimens with closed ties. For the CFRP-RC columns, rupture of the CFRP tie was recorded for all tie configurations. Brown (2015) stated that with replacement of steel reinforcement by GFRP, the failure mode of the column was more sudden due to the lower modulus of elasticity of GFRP bars compared to steel ones.

Alsayed et al. (1999) observed a significant effect for the type of transverse reinforcement on the ascending branch of the load-axial deformation relationship. For instance, the GFRP ties were found to be ineffective up to 80% of the peak load, while the steel ties were active from the beginning of the loading. De Luca et al. (2010) reported that the smaller spacing of the GFRP ties (3 in.) did not enhance the axial capacity, but it did affect the failure mode as it delayed the buckling of the longitudinal bars, initiation of unstable crack propagation, and crushing of the concrete core.

Moreover, enhancements of ductility, toughness, ultimate load, ultimate strain and initial cracking load of the columns were found by Lotfy (2010) as a result to increasing of lateral reinforcement volumetric ratio or concrete compressive strength for the GFRP-RC specimens. He also stated that using longitudinal GFRP reinforcement with less tie spacing gives more toughness and ductility than using longitudinal steel bars and normal tie spacing. Tobbi et al. (2012) concluded that the effect of lateral confinement was evident just after the concrete cover had completely spalled off, resulting in significant gains in strength, ductility and toughness for the concrete cores of well-confined specimens, which clarified the effectiveness of GFRP as transverse reinforcement. For all-steel circular columns, Pantelides et al. (2013) observed corrosion more often for the steel spirals, reducing the confinement to the concrete core and resulting in a brittle failure. That justified the use of non-corrodible GFRP spirals, which were found also to minimize the cracking of concrete cover as they did not expand, keeping the corrosion rate for the hybrid columns less than one-third the value for all-steel corroded columns. In addition, it was recommended to increase both the longitudinal and transverse reinforcement for the all-GFRP-RC columns in order to achieve a comparable behaviour to the all-steel non-corroded columns. In terms of confinement efficiency, FRP tie configuration and spacing were found to be the most affecting parameters (Tobbi et al. 2014). The observed results shown the superiority of closed ties rather than C-shaped ties in terms of lateral restraint. Moreover, GFRP ties were observed to be more cost effective than CFRP ties only in case of high volumetric ratio with closer spacing. On the other hand, CFRP performed better for the large spacing with lower volumetric ratio. Generally, more stabilizing post-peak behaviour was noticed for less tie spacing. It was also concluded that under good confinement conditions, the FRP-RC columns could reach an ultimate axial compressive strain almost equal to the FRP ultimate tensile strain. Mohamed et al. (2014) suggested volumetric ratio of 1.5% to be a threshold between the poorly confined FRP-RC circular column specimens, which failed in a brittle and explosive manner, and the well confined ones whose failure was characterized by crushing of the concrete core and rupture of the FRP spirals. In addition, a spiral volumetric ratio less than 1.5% or spiral pitch larger than 80 mm resulted in a brittle explosive failure for the tested GFRP-RC specimens (Afifi et al. 2014). Furthermore, adopting closer spaced spirals with smaller diameter was found to be more effective than larger spaced spirals with larger diameter, for better confinement of the concrete core and lateral restraint for the longitudinal bars. For circular hoops, a splice length of 20 times the hoop diameter was found sufficient to avoid pullout or slippage premature failure of FRP hoops Mohamed et al. (2014). Prachasaree et al. (2015) concluded that increasing the confining pressure resulted in increasing both concrete strength and deformability in the inelastic range. Also, the lateral reinforcement affected the confining pressure and inelastic deformation, and hence, its contribution to the confined concrete strength increased with the GFRP transverse reinforcement ratio. On the other hand, the concrete cover mainly affected the early confinement effects, but not the maximum load capacity or late stage deformation.

Alsayed et al. (1999) reported that the available equations by the code back then to predict the axial capacity of the columns overestimate the capacity for the GFRP-RC columns by 12%. De Luca et al. (2010) proposed some considerations for GFRP bars to include them in the design of compression members, such as: (1) the strength-reduction factor for pure compression adopted for steel-RC columns can be adopted for GFRP-RC ones as well; (2) the contribution of GFRP bars in the column’s pure axial capacity is to be neglected; (3) the use of GFRP bars as internal reinforcement is economical as long as the equivalent axial load is within the kernel of the section; and (4) GFRP ties cannot be designed based on the same guidelines for steel transverse reinforcement in the steel-RC columns, as they resulted in a brittle failure for the GFRP-RC specimens. The predicted values of ultimate axial capacity for the experimentally tested GFRP-RC columns by Lotfy (2010), computed based on the first principles of the ultimate theory, were found to be in acceptable agreement with the experimental results. Tobbi et al. (2012) suggested using the same strength reduction factor of steel-RC columns, equals to 0.85, for GFRP-RC columns. Furthermore, using the GFRP compressive strength as 35% of its tensile strength resulted in a satisfactory estimation of ultimate capacity when compared to the experimental results. Moreover, a proposed equation was developed by Pantelides et al. (2013), taking confinement stress by internal GFRP spirals as a modified form of the confinement provided by externally bonded FRP jackets as given by the ACI 440.2R-08 model. This equation gave a satisfactory result comparing to the experimental results, yet more conservative. The reduction factor of 0.35 suggested for compressive strength of GFRP bars by Tobbi et al. (2012), resulted in reasonably accurate and conservative prediction of the axial capacity of the columns tested by Afifi et al. (2014). It was also added that neglecting the contribution of the GFRP bars in compression underestimated the axial capacity of the GFRP-RC columns. Similarly, Tobbi et al. (2014) proposed an equation based on elastic theory, which had reasonably predicted the axial capacity when compared with the experimental results, indicating that the contribution of FRP longitudinal reinforcement in the axial capacity of the FRP-RC columns should not be neglected. Furthermore, Mohamed et al. (2014) proposed a reasonably accurate design equation to predict the ultimate axial capacity of FRP-RC columns, limiting the compressive strain of the CFRP and GFRP bars to 0.002. This provides a basis for bridge-design provisions to utilize FRP reinforcement as longitudinal and transverse reinforcement for bridge piers and piles.

2.6.2 Behaviour of FRP-RC Column Under Eccentric loads

Choo et al. (2006) conducted an analytical study on the behaviour of concrete columns reinforced with longitudinal FRP bars. For longitudinal reinforcement ratios of 1%, 3%, 5% and 8%, the axial load-bending moment interaction curves were developed for AFRP, GFRP and CFRP-RC columns. It was concluded that, unlike steel RC columns which exhibit balanced points on axial load-bending moment interaction diagrams, at which steel reaches its yield strain at the same time as concrete crushes; FRP-RC columns do not exhibit such balanced points, for longitudinal reinforcement ratio's limits of 1% to 8%, as defined by the ACI 318-05. This was attributed to the well-defined yield point and plateau of steel, whereas FRP bars exhibit linear-elastic stress-strain behaviour until failure. In some cases, FRP-RC columns experienced brittle tension failure by exhibiting a failure point on the strength interaction diagrams before reaching a pure bending condition. This type of failure occurred when the extreme concrete compression fibre reached its ultimate strain of 0.003, according to ACI standards, and at the same time the outermost FRP reinforcing bars reaches its limiting tensile strain. FRP-RC columns are susceptible to this kind of failure when reinforced with low percentage of longitudinal reinforcements such as 1%.

Issa et al. (2011) investigated the response of eccentrically loaded GFRP-RC columns. Six specimens with 150 x 150 mm cross-sections, with extensions at both ends for the eccentric loading, and 1200 mm height were cast and tested under monotonic eccentric compression up to failure. Four specimens were reinforced with 12 mm GFRP longitudinal rods, while the rest were steel-reinforced for comparing purposes. All the ties were 8 mm steel ties for all specimens. The main studied parameters were the reinforcement type, compressive strength of concrete, tie spacing, and eccentricity. It was reported that in general, GFRP-RC columns exhibited more deformations than steel-RC counterparts in terms of axial deformation, and bar strains. In addition, the increase of tie spacing proportionally affected the axial deformation, especially for GFRP-RC specimens, and bar strains for both types of reinforcement, while it adversely affected the ductility, especially for steel-RC specimens. On the other hand, tie spacing had no obvious effect on the maximum lateral deformation, or axial deformation for steel-RC columns, nor on the ductility of the GFRP-RC columns. Also, the concrete strength adversely affected the GFRP bar strains. The maximum stress for the GFRP-RC column with an eccentricity-to-total depth ratio of one-third was about 60% of the concrete compressive strength. Moreover, interaction diagrams for GFRP-RC specimens were generated based on equilibrium and strain compatibility, as well as assumptions from previous studies. The resulted diagrams, when compared to the experimental results, represented a lower limit.

Zadeh and Nanni (2013) studied the available RC and FRP-RC design codes and literature. They showed that with the existing knowledge, it is possible to develop a methodology for the design of concrete columns with rectangular or circular cross-section using GFRP bars as longitudinal and transverse reinforcement. It was concluded that the ultimate tensile rupture strain should not exceed 1% to avoid excessive deformations. For GFRP-RC columns, it was also suggested to use a spacing of transverse reinforcement as the least dimension of the column, 12 times the diameter of longitudinal bars, or 24 times the tie bar diameter, whichever is less. It was also suggested to neglect the slenderness effect for GFRP-RC columns in a non-sway frame when the slenderness ratio is less than 40.

A parametric study performed by Mirmiran et al. (2001) reported that FRP-RC columns are more susceptible to slenderness effects than steel-RC columns due to lower stiffness and compressive strength contribution of FRP longitudinal bars, and advised to reduce the current slenderness limit of 22 for steel-RC columns bent in single curvature to 17 for FRP-RC columns. Tikka et al. (2010)

conducted an experimental study on rectangular GFRP-RC slender (kl_u/r = 41.6) columns under eccentric loads and concluded that columns showed excessive deformation providing warning prior to failure. Xue et al. (2018) tested fifteen slender (kl_u/r = 20.8 to 41.6) rectangular GFRP-RC columns under eccentric loads and concluded that all columns failed by concrete crushing and no rupture of FRP bars were noticed. Recently, Maranan et al. (2016) reported that concentrically-loaded slender (kl_u/r = 16) geopolymer-concrete circular column reinforced with GFRP bars and spirals failed at 18% lower loads than that of the short column.

Hadi et al. (2017) reported for GFRP-reinforced HSC circular columns that axially loaded GFRP-reinforced HSC columns exhibited similar axial capacities to the steel-reinforced HSC counterparts. The contribution of the GFRP longitudinal bars in the total axial capacity of GFRP-reinforced HSC columns was about half that of the steel-reinforced HSC counterparts. Taking the contribution of the GFRP longitudinal bars in the total axial capacity into account provided in good agreement between the analytical and the experimental results. For the poorly-confined GFRP-reinforced columns, the axial capacity dropped suddenly by 50% and a sudden and catastrophic failure occurred, triggered by rupture and buckling of GFRP bars. On the other hand, well-confined GFRP-reinforced columns exhibited a second peak load higher than the first peak, yet lower by 12% than the steel-reinforced counterpart. In addition, the ductility of GFRP-reinforced columns was 30% lower than that of their steel-reinforced counterparts. It was reported that the ductility can be improved by reducing the GFRP spiral pitch, yet the stability of concrete cover would depend on the thickness of that cover.

Hadhood et al. (2017a) investigated the behaviour of GFRP-RC circular columns under monotonic concentric and eccentric loading. Ten circular RC columns reinforced with GFRP bars and spirals, with a 305 mm diameter and 1500 mm length were constructed with high strength concrete (HSC) and tested. The tested variables were the eccentricity-to-diameter (*e/D*) ratio and the longitudinal reinforcement ratio. They concluded that the high deformability of FRP contributed to the enhancement of the stiffness of cracked concrete sections in the columns constructed using HSC. Compression failure characterized by concrete crushing was observed for the specimens tested under concentric to moderate eccentric loading (*e/D* ratios of 8.2 and 16.4%). On the other hand, excessive cracks, axial deformations and lateral deflections on the tension sides resulted in a flexural-tension failure for the high to extreme eccentrically loaded specimens (*e/D* ratios of 32.8 and 65.6%), which was supposed to be followed by a secondary compression failure due to the strain limitations of concrete. In addition, for the specimens with eccentricity-to-diameter ratios of 8.2, 16.4, 32.8, and 65.6%, ultimate load loss of 30, 50, 75, and 90% were observed, respectively, with respect to the concentrically loaded counterpart. For the longitudinal reinforcement ratio, the increase from 2.2 to 3.3% did not affect the concentrically-loaded column, while it slightly affected the eccentrically-loaded specimens, specially the post-peak behaviour, decreasing the strength decay after the peak load. It was also reported that GFRP bars could carry around 5% of the maximum load of the column. The experimental results observed indicated that the adopted GFRP reinforcement, which satisfies CSA S806-12 (CSA 2017) requirements could maintain the integrity of the columns up to the estimated nominal axial-flexural strength. The predicted interaction diagrams were developed using the code assumptions of ACI 440.1 R-15 or CSA S806-12, as well as strain compatibility, and force equilibrium, against experimental results. The axial and flexural capacities of the tested specimens were predicted with conservative but reasonable values when compared with the experimental results. Hadhood et al. (2017b) reported for NSC specimens similar to the aforementioned study and concluded that columns tested under concentric and low eccentric loads failed due to crushing of concrete whereas flexural-tension failure started in columns under high eccentric loads resulting from excessive axial and lateral deformations and cracks until secondary compression failure occurred due to strain limitations in concrete and degradation of the concrete compressive block.

2.6.3 Behaviour of FRP-RC Members Under Flexural Loads

Theriault and Benmokrane (1998) found that the ultimate flexural capacity of GFRP-RC rectangular beams increases as the longitudinal reinforcement ratio increased. However, this increment is limited by the concrete crushing strain of over-reinforced RC beams. Kassem et al. (2011) reported that FRP-RC beams failed due to concrete crushing because the actual longitudinal reinforcement ratio was higher than the balanced reinforcement ratio. A reinforcement ratio more than $1.4\rho_{fb}$ is recommended to ensure compression failure. El-Nemr et al. (2013) reported that increasing the reinforcement ratio and concrete strength resulted in a significant number of cracks with smaller crack widths. RC beams reinforced with sand-coated GFRP bars produced a significant number of cracks with smaller crack widths than those reinforced with helically grooved GFRP bars, which tends to confirm the better flexural bond characteristics of the sand-coated bars. Nanni (1993) studied the flexural behaviour of concrete beams reinforced with different GFRP bars (smooth or sand-coated) and steel deformed bars. It was mentioned that the sand-coated FRP bars increased the ultimate flexural capacity by approximately 25% compared with the equivalent uncoated rebars. The authors stated that the ultimate strength could be predicted based on the material properties of the concrete and reinforcement. Kassem et al. (2011) reported that surface texture played no role in enhancing the flexural capacity when sand-coated bars and ribbed- surface bars were used. Recently, Mousa et al. (2018) investigated the flexural strength of GFRP-RC circular members under four-point bending loads and reported that GFRP spirals were able to prevent buckling of GFRP longitudinal bars and effectively confined the concrete core at increased strain level in the post-peak stages. In addition, the flexural strength of GFRP-RC circular members at ultimate concrete strain was almost two times higher than that of the counterpart steel-RC specimen while having the same amount of reinforcements (Mousa et al. 2018).

2.7 AVAILABLE PROVISIONS FOR DESIGN OF FRP-RC COLUMNS

2.7.1 Design for Axial Capacity

Steel and FRP-RC members behave quite similarly under axial and flexure loading even though they possess different mechanical properties. Steel possesses high tensile and compressive strength, and also exhibits a definite yielding plateau which makes it a ductile material. On the other hand, FRP has high tensile but low compressive strength compare to steel and exhibits linear stress-strain behaviour until failure, which makes it a brittle material. Due to this brittleness, the Canadian code CSA S806-12 (CSA 2017) requires all FRP-RC compression members to be designed as compression-controlled rather than tension-controlled. This means failure should happen by crushing of concrete before rupture of FRP bars in RC compression members, as it will ensure deformability of concrete due to the plastic deformation. In addition, CSA S806-12 (CSA 2017), clause 8.4.3.1 states not to include the contribution of FRP bars in compression zones because of their lower compressive strength, which is a conservative approach. Clause 8.4.3.7 specified a minimum usable longitudinal reinforcement limit of 1% of the gross cross-section for FRP-RC columns. This limit was established based on the minimum reinforcement ratio of steel-RC columns, but later, it was kept the same to avoid brittle tension failure under simultaneous axial load and bending, and to account for sustained load developed from concrete creep and shrinkage and transferred to the reinforcement. Moreover, for FRP-RC compression members, the maximum limit for usable longitudinal reinforcement is 8% specified in clause 8.4.3.9, which is similar as used for the steel ones. Clause 8.4.3.10 mentioned about the minimum number of FRP longitudinal bars as four, three and six that should be confined by rectangular or circular ties, triangular ties and spirals, respectively. Also, the minimum FRP longitudinal bar diameter should not be less than 15 mm. Clause 8.4.3.3 have set two equations to take into account the effect of slenderness and also stated not to use FRP longitudinal bars in slender columns.

For compression members braced against side sway:

$$\frac{kl_u}{r} \geq 34 - 12\left(\frac{M_1}{M_2}\right) \geq 40 \qquad \text{Eq. 2.2}$$

For compression members not braced against side sway:

$$\frac{kl_u}{r} \geq 22 \qquad \text{Eq. 2.3}$$

Where, k is the effective length factor, l_u is the effective length of column, r is the radius of gyration of the column section, M_1 and M_2 are the smaller and larger factored end moments and $\left(\frac{M_1}{M_2}\right)$ is positive if the column is bent in single curvature and negative if the member is bent in double curvature.

Clause 8.4.3.6 has mentioned an equation to calculate the maximum factored axial load resistance for spirally reinforced circular columns.

$$P_{r,max} = 0.85P_{ro} = 0.85\alpha_1 f'_c\left(A_g - A_F\right) \qquad \text{Eq.2.4}$$

Where, f'_c is the compressive strength of concrete; A_g is the gross area of the column section; A_F is the gross area of longitudinal FRP bars and α_1 is the rectangular stress block factor which is determined according to clause 8.4.1.5 as follows:

$$\alpha_1 = 0.85 - 0.0015f'_c \qquad \text{Eq.2.5}$$

According to clause 8.4.1.4, the maximum usable concrete strain is 0.0035.

2.7.2 Design for Confinement

To avoid buckling of longitudinal FRP bars and to provide sufficient confinement, CSA S806-12 (2017) has established design provisions for confinement of FRP-RC compression members. For spirally confined compression members, clause 8.3.4.13 specified the selection criteria for size and spacing of spirals as (a) spiral reinforcement shall have a minimum diameter of 6 mm, (b) spiral pitch should not exceed 1/6 of the core diameter, (c) clear spacing of successive turns of spirals should not be less than 25 mm or exceed 75 mm and (d) volumetric ratio of spiral reinforcement should no be less than the following equation:

$$\rho_{Fs} = \frac{f'_c}{f_{Fh}}\left(\frac{A_g}{A_c} - 1\right)\left(\frac{P}{P_o}\right) \qquad \text{Eq.2.6}$$

Where, f_{Fh} is the design stress level in FRP transverse confinement reinforcement taken as the least of $0.006E_F$ or $\Phi_F f_{Fu}$, A_g is the gross cross-sectional area of the column, A_c is the cross-sectional area of column core, P is the specified axial load on column section, P_o is the nominal unconfined axial load capacity of column calculated as $\alpha_1 f_c'(A_g - A_F)$ for columns with FRP longitudinal reinforcement. Minimum ratios of $\frac{A_g}{A_c}$ and $\frac{P}{P_o}$ are set to be 0.3 and 0.2, respectively.

2.8 SUMMARY OF LITERATURE AND RESEARCH GAPS

Limited research has been conducted on the behaviour of GFRP-RC circular members subjected to axial and flexural loads (Hadhood et al. 2017b; Mousa et al. 2018). The most recent research relevant to this area was conducted by Hadhood et al. (2017b). The authors have investigated the behaviour of GFRP-RC circular short columns under monotonic concentric and eccentric loading as described above in Section 2.6.2 of this thesis. Even though important findings were reported, the contribution of GFRP spirals was completely ignored in this research, which is very important for circular column's confinement, deformability, and the overall performance. Another gap of that research is the pure flexural strength of GFRP-RC circular columns was not evaluated experimentally, which is necessary to develop a complete P-M interaction diagram. In addition, relatively high longitudinal reinforcement ratios, which is uncommon in practice, were used. As concluded by the authors, the behaviour of these columns depended significantly on the longitudinal reinforcement ratio and thus testing columns, with minimum reinforcement ratio (commonly used in practice), deemed necessary.

The following questions arise out of the research carried out by Hadhood et al. (2017b):

- What is the contribution of GFRP spirals on column's confinement and the overall performance subjected to axial and flexural loads?
- What is the effect of varying spiral pitch on column's capacity, deformability, and modes of failure?
- Why the pure flexural strength of GFRP-RC circular columns was not evaluated experimentally to complete the P-M diagram?
- What is the effect of using minimum longitudinal reinforcement ratio on column's capacity, deformability, and modes of failure?

Based on the above identified research gaps, the following test parameters are selected for short columns in this study.

- GFRP spiral pitch (50 and 85-mm),
- Minimum longitudinal reinforcement ratio (1.2%),
- Testing under pure flexural loads to develop a complete normalized P-M interaction diagram for GFRP-RC circular columns,
- Evaluating the contribution of GFRP spirals for columns tested under axial and flexural loads through strain measurements.

Furthermore, Mousa et al. (2018) investigated the flexural strength of GFRP-RC circular members under four-point bending. The parameters selected type of reinforcement (steel vs. GFRP) and the longitudinal reinforcement ratios (1.2, 2.3, and 3.5 %) as described above in Section 2.6.3 of this thesis. However, the authors only considered pure flexural loads and totally ignored the effects of axial loads (both concentric and eccentric), which is normally the main load on columns. Therefore, this work was investigating the behaviour of GFRP-RC circular flexural members (beams) and not columns.

In addition to filling out the above-mentioned research gaps, the performance of circular GFRP-RC slender columns is also evaluated in this study through experimental investigation. Up to the author's knowledge, this is the first study to experimentally evaluate the performance of large-scale circular GFRP-RC slender columns.

Based on the presented literature on steel-RC columns, the following parameters are selected to carry out the experimental investigation:

- Type of reinforcing materials (GFRP or Steel),
- High slenderness ratio of 28,
- Type of loading (Axial or flexural load),
- Axial load's eccentricity-to-column diameter ratio (0, 0.085, 0.17, or 0.34).

It is expected that testing the above parameters for slender columns will lead to the following:

- Develop P-M interaction diagram for GFRP-RC circular slender columns,
- Provide longitudinal GFRP bar and spiral strain profiles for slender columns,
- Provide load-lateral deflection curves for slender columns.

CHAPTER 3 – EXPERIMENTAL PROGRAM

3.1 GENERAL

In this study, thirteen full-scale short and slender circular concrete columns reinforced with steel and GFRP bars and spirals were designed, constructed, and tested to failure under axial and flexural loads. The experimental program was divided into two phases. In the first phase, experimental work was conducted to evaluate the performance of circular GFRP-RC short (Series I) column, and in the second phase performance of GFRP-RC slender (Series II) columns was evaluated. The following sections of this chapter describe the properties of materials used, specimen details, construction process, instrumentation, test setup, and testing procedure.

3.2 MATERIAL PROPERTIES

Sand-coated GFRP bars and spirals were used to reinforce GFRP-RC columns, while conventional G400 deformed steel bars and spirals were used to reinforce the control specimen. The mechanical properties of GFRP bars and spirals were provided by the manufacturer in a certificate of compliance (Pultrall Inc. 2019). However, the mechanical properties of the used steel bars were obtained through standard tensile tests carried out in the laboratory. The properties of GFRP and steel reinforcement are given in Table 3.1. All thirteen columns were cast with normal-weight, ready-mixed concrete with a specified 28-day compressive strength of 35 MPa. The actual compressive strength was determined on the day of testing each column based on testing three standard concrete cylinders (100 × 200 mm) according to CSA/A23.1-14 (CSA 2014a), as listed in Table 3.2. Columns were cast vertically to simulate the typical construction practice.

Table 3.1: Mechanical properties of GFRP and steel reinforcement

Bar size	Type	Nominal diameter (mm)	Area (mm^2)		Elastic tensile modulus (GPa)	Tensile strength (MPa)	Ultimate strain (%)
			Nominal	CSA S806-12 Annex A			
No.16	GFRP (straight)	15.9	199	235	64	1,558	2.4
No.10	GFRP (spiral)	9.5	71	83	58	667	1.14
15M	Steel (straight)	16.0	200	-	200	460[a]	0.23[b]
10M	Steel (spiral)	11.3	100	-	200	420[a]	0.21[b]

[a]Yield strength of steel bars and spiral;
[b]Yield strain of steel bars and spirals

3.3 SPECIMEN DETAILS AND CONSTRUCTION PROCESS

In this study, eleven full-scale GFRP-RC and two steel-RC circular columns were constructed and tested to failure under concentric, eccentric, and four-point bending loads. All test columns are measured 355-mm in diameter. Total thirteen test columns divided into two series, namely Series I and Series II. Series I include six GFRP-RC and one steel-RC short columns of 1,750 mm length corresponding to a slenderness ratio of 20. Series II includes five GFRP-RC and one steel-RC slender columns of 2,450 mm length corresponding to a slenderness ratio of 28. All test columns were designed according to the Canadian standards (CSA 2017 and 2014b) for steel and FRP-RC structures, as appropriate. Eleven GFRP-RC columns were constructed using 6-No. 16 (15.9-mm diameter) sand-coated GFRP longitudinal bars and confined with No. 10 (9.5-mm diameter) continuous GFRP spirals with 50 or 85-mm pitch, as shown in Fig. 3.1 and Fig. 3.2. Two steel-RC control specimens were built using 6-15M (16-mm diameter) steel longitudinal bars and 10M (11.3-mm diameter) continuous steel spiral with a pitch of 85 mm. Table 3.2 provides the test matrix and reinforcement details of the column specimens. Each column identified with two letters and three numbers. The first letter is “S” or “G” referring to steel or GFRP, respectively, while the first number represents the slenderness ratio (20 or 28). The second number represents the spiral pitch (50 or 85 mm). The second letter is “C”, “E” or “F” referring to concentric, eccentric or pure bending loading conditions, and the third number represents the eccentricity of the axial load (00, 30, 60, or 120 mm).

Table 3.2: Test matrix and specimen details

	Specimen ID	f'_c (MPa)	Slenderness ratio	e (mm)	e/D (%)	Longitudinal reinforcements		Transverse Spirals		
			$\frac{kl_u}{r}$			No. of bars	ρ_f (%)	Bar size	Spiral pitch (mm)	ρ_{fs} (%)
Series I	G20-85-C00	37.4	20	0	0	6-No.16	1.20	No.10	85	1.11
	S20-85-E30	35.6		30	0.085	6-15M	1.21	10M	85	1.43
	G20-85-E30	39.4		30	0.085	6-No.16	1.20	No.10	85	1.11
	G20-50-E30	40.7		30	0.085	6-No.16	1.20	No.10	50	1.89
	G20-85-E60	38.0		60	0.17	6-No.16	1.20	No.10	85	1.11
	G20-85-E120	37.3		120	0.34	6-No.16	1.20	No.10	85	1.11
	G20-85-F	38.9		-	-	6-No.16	1.20	No.10	85	1.11
Series II	G28-85-C00	32.5	28	0	0	6-No.16	1.20	No.10	85	1.11
	S28-85-E30	35.3		30	0.085	6-15M	1.21	10M	85	1.43
	G28-85-E30	37.7		30	0.085	6-No.16	1.20	No.10	85	1.11
	G28-85-E60	31.0		60	0.17	6-No.16	1.20	No.10	85	1.11
	G28-85-E120	38.8		120	0.34	6-No.16	1.20	No.10	85	1.11
	G28-85-F	39.6		-	-	6-No.16	1.20	No.10	85	1.11

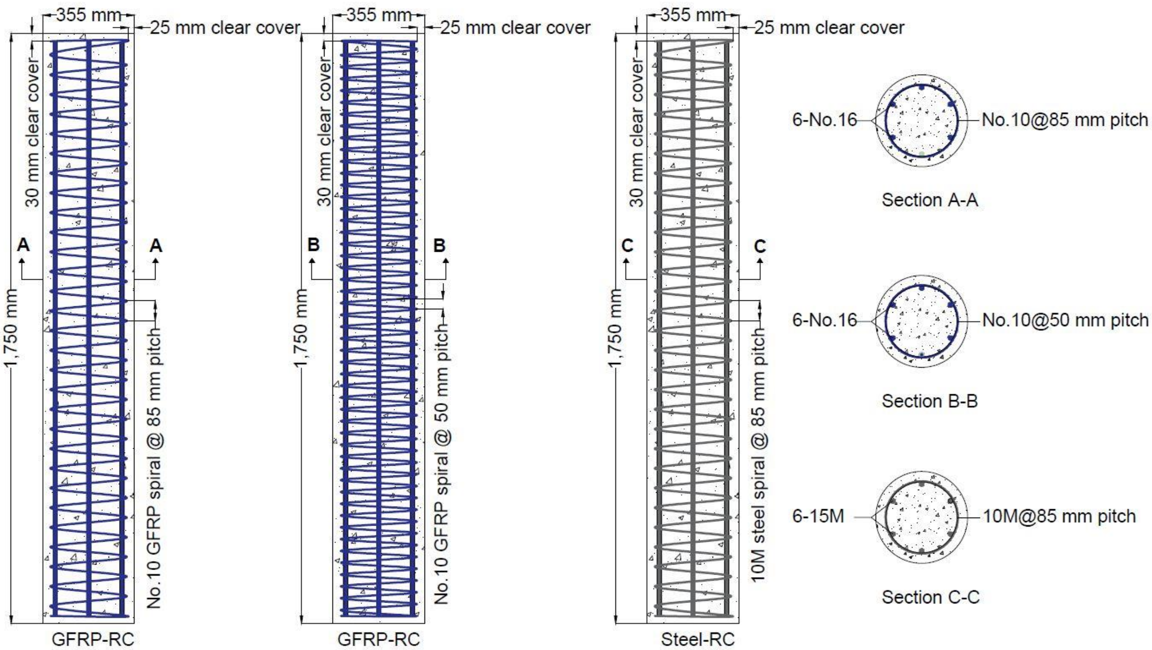

Fig. 3.1: Details of GFRP and steel-RC short columns (Series I)

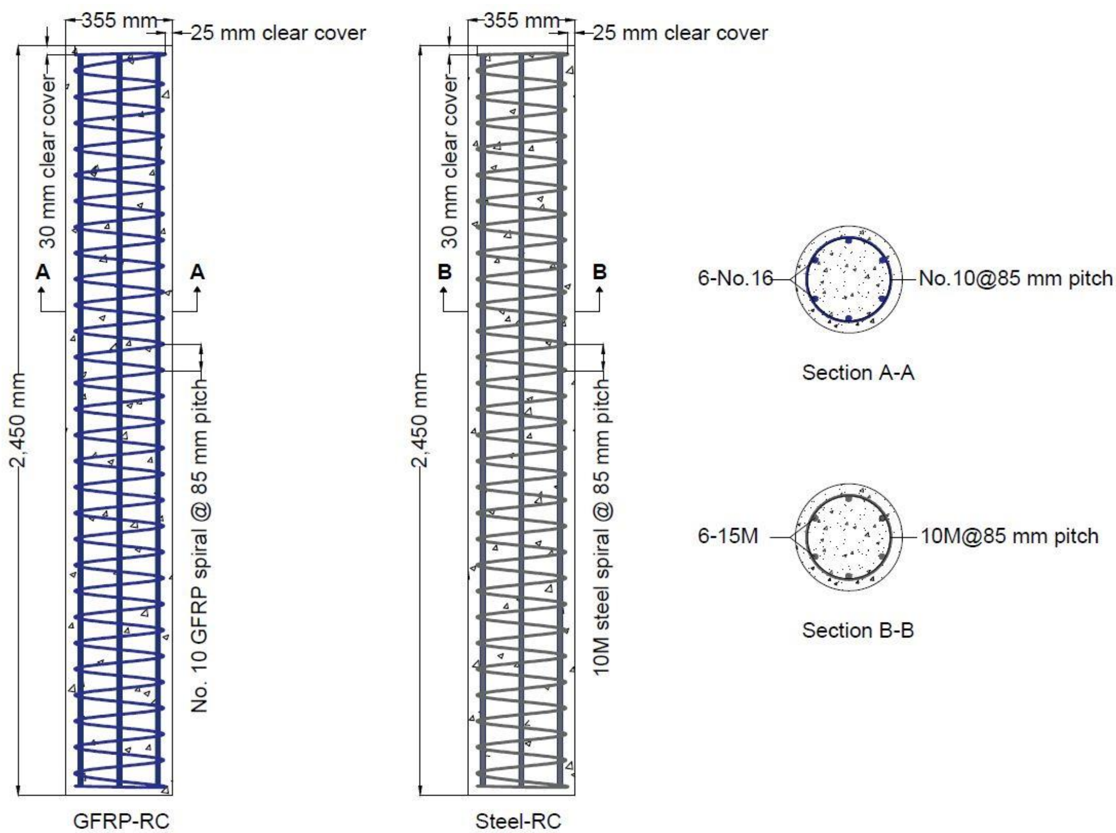

Fig. 3.2: Details of GFRP and steel-RC slender columns (Series II)

All steel and GFRP rebar cages assembled to construct thirteen RC columns, as shown in Fig. 3.3 (a). The concrete cover kept constant at 25 mm to the face of the spirals. Columns were cast vertically using stiff sono-tubes. Wooden formworks were used, as shown in Fig. 3.3 (b), to hold the sono-tubes upright. Then, the cages were inserted into the sono-tubes. All columns were cast vertically to simulate the typical construction practices of columns. A local ready-mix concrete company provided the concrete. The concrete discharged into the column forms in three lifts, and an electric vibrator used to consolidate the concrete and to remove air bubbles.

a) Rebar cages b) Wooden formwork c) Slump test

f) RC column specimens e) Electrical vibration d) Concrete casting

Fig. 3.3: Construction process of RC columns

3.4 INSTRUMENTATION

To measure strains, electrical strain gauges were attached to longitudinal bars, spirals, and concrete surfaces at critical locations as shown in Fig. 3.4 and Fig. 3.5. Also, PI-gauges were placed on concrete surface on both tension and compression sides to measure strains on a longer column length (200 mm). All these gauges were placed at the column mid-height, where maximum strains were expected. To measure lateral displacements, three linear variable displacement transducers (LVDTs) were mounted perpendicular to the axis of each specimen; at the mid-length and quarter-length locations. For axial displacement in columns under axial loads, displacement readings from loading machine were used along with two LVDTs that were installed vertically at mid-height of the column as shown in Fig. 3.4 and Fig. 3.5.

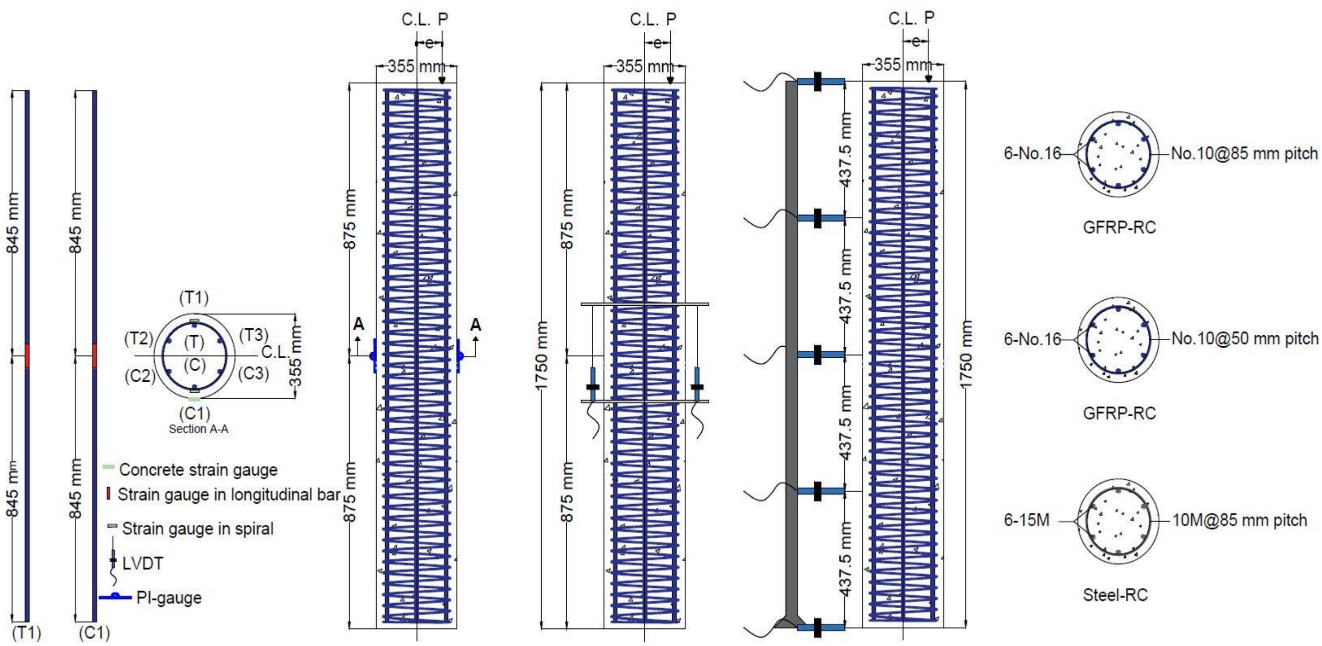

(a)

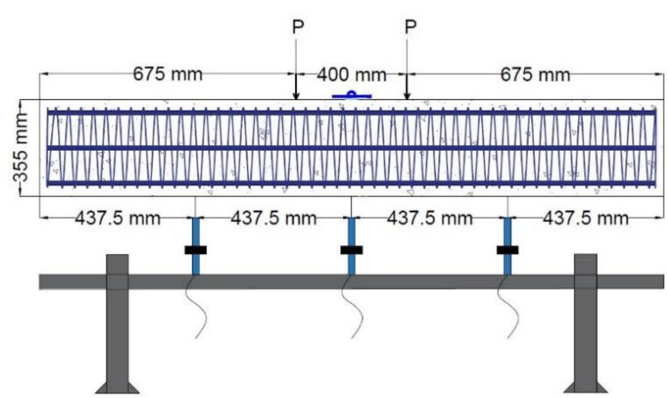

(b)

Fig. 3.4: Instrumentation details for short columns (Series I): (a) Under axial load, and (b) Under four-point bending loads.

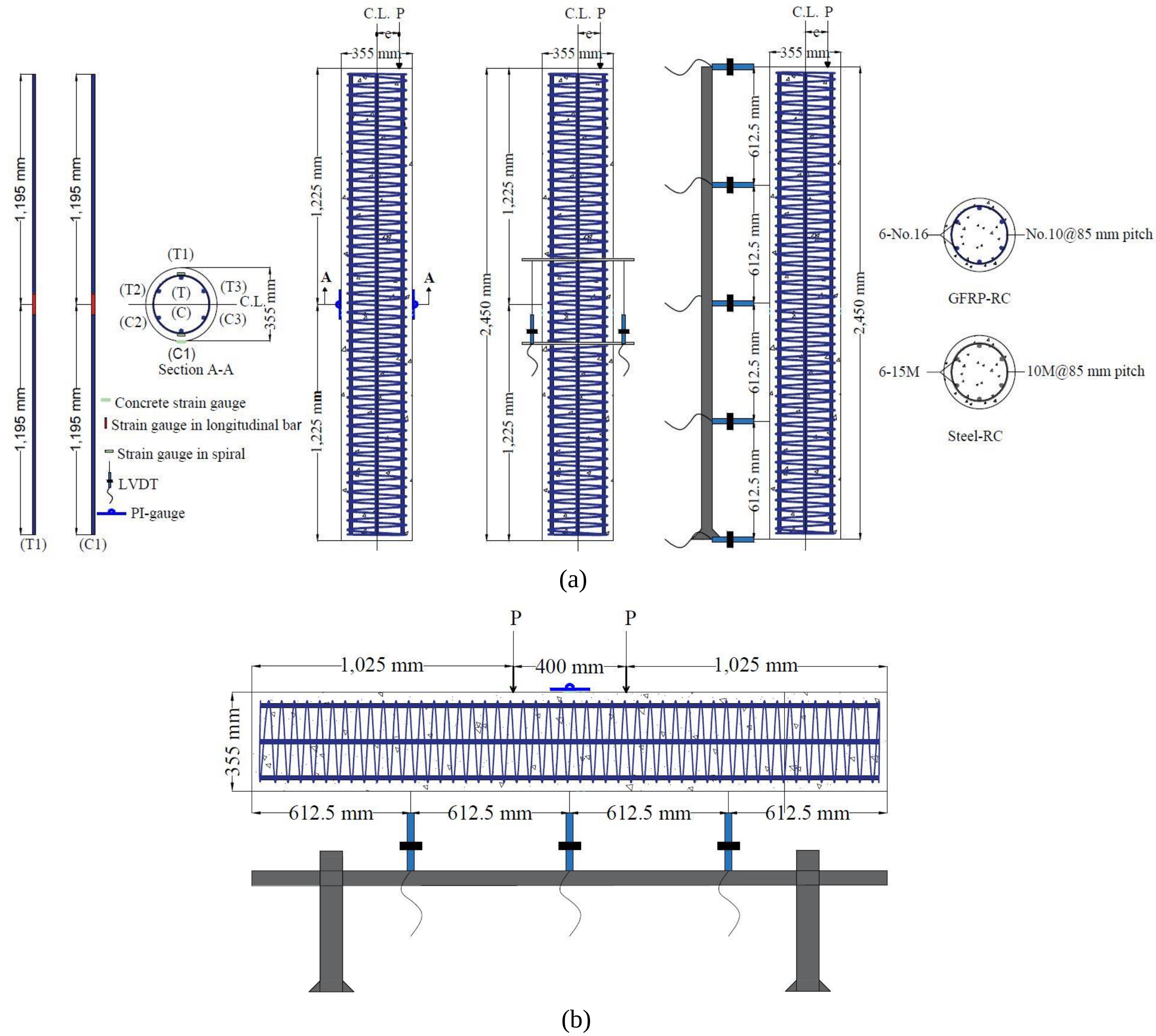

Fig. 3.5: Instrumentation details for slender columns (Series II): (a) Under axial load, and (b) Under four-point bending loads.

3.5 TEST SETUP AND PROCEDURE

A special apparatus to apply axial loading was designed and fabricated in the McQuade Heavy Structures laboratory at the University of Manitoba. The apparatus consists of two high strength steel loading caps measuring 406-mm in diameter and 350-mm in depth that were attached to column ends to apply the concentric and eccentric loads; ensuring no slippage or premature failure at the column ends. The column was centered inside the caps, then the gap between the cap and the column surface was filled with grout. Two GFRP-RC columns were tested under concentric loads as shown in Fig. 3.6 (a) and Fig. 3.7 (a) and nine columns were tested under varying eccentricity-to-diameter ratios (e/D = 0.085, 0.17 and 0.34) as shown in Fig. 3.6 (b) and Fig. 3.7 (b). To change the axial load eccentricity, two half-cylinder steel pins of 50-mm diameter were welded to the top surface of the upper cap, and the bottom surface of the lower cap at the desired eccentricity as listed in Table 3.2, which represented pin-ended support condition. The pins fit into grooved plates aligned with the center of the load, one at the top fixed to the loading machine crosshead and the other at the bottom fixed to the base of the machine. The grooves and pins allowed free rotation of the column ends during the test.

The axial load was applied using a 5000-kN capacity hydraulic machine with a displacement-controlled rate of 1.0 mm/minute. Two specimens were tested under four-point bending loads in a simply supported horizontal layout as shown in Fig. 3.6 (c) and Fig. 3.7 (c). The specimen was loaded through the same hydraulic machine attached to a spreader beam using the same displacement-controlled rate as the axial load. Four semi-circular steel saddles were fabricated matching the curvature of the column. Two of these saddles were welded to the spreader beam at the two loading-points and the other two were welded to the two end supports. All test measurements including machine load, machine stroke, strains, and displacements were recorded with a data acquisition system. The test was stopped when the capacity for the column dropped by 25% of the peak load.

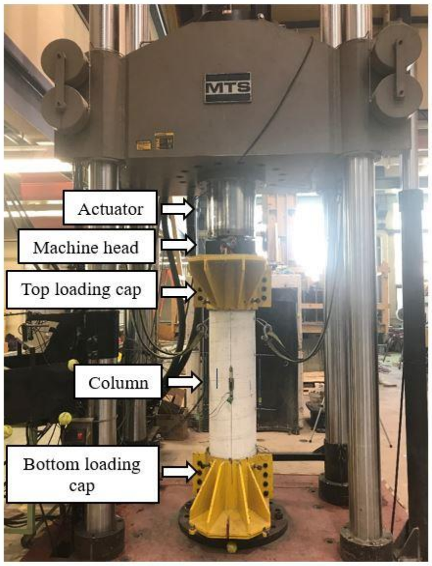

(a)

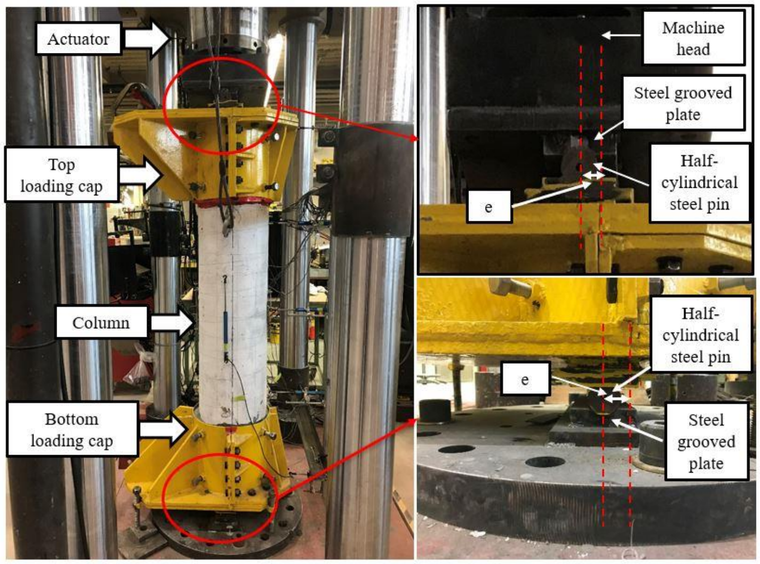

(b)

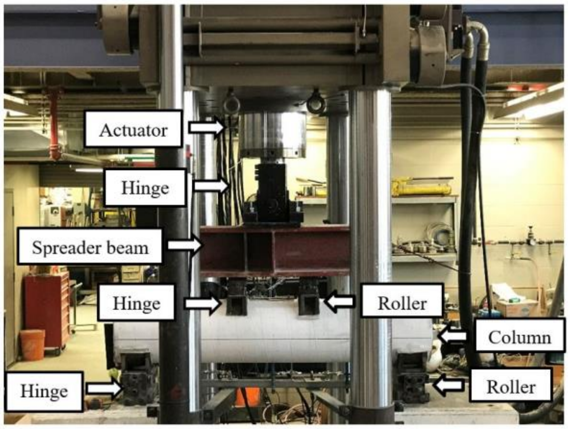

(c)

Fig. 3.6: Test setup (Series I), (a) Concentrically-loaded column; (b) Eccentrically-loaded column; (c) Column under four-point bending loads.

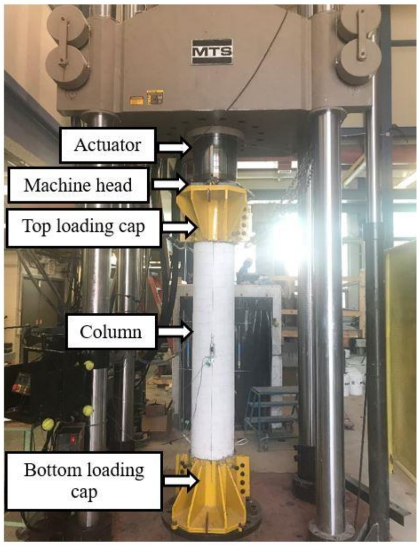

(a)

(b)

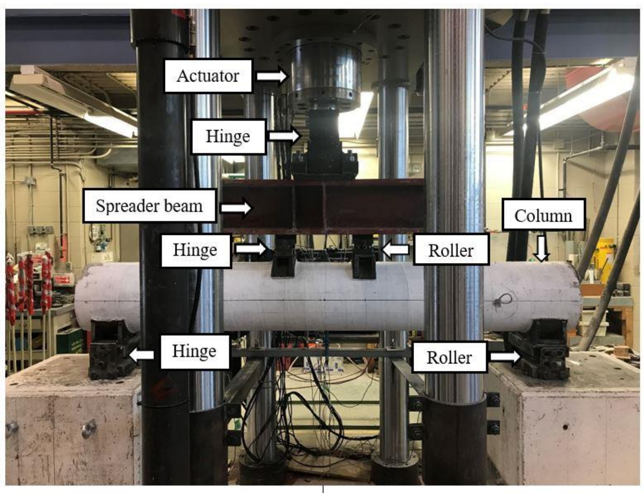

(c)

Fig. 3.7: Test setup (Series II), (a) Concentrically-loaded column; (b) eccentrically-loaded column; (c) Column under four-point bending loads

CHAPTER 4 – RESULTS AND DISCUSSION OF SERIES I

4.1 GENERAL

In this chapter, the test results of seven full-scale steel and GFRP-RC short columns (Series I) are presented and discussed. All short columns are measured 355 mm in diameter, and 1,750 mm in length. One out of seven short columns (Series I) were tested under concentric loads; five were tested with varying eccentricity-to-column diameter ratios (e/D = 0.085, 0.17, and 0.34); and the last one was tested under four-point bending loads. Structural performance of these tested columns are evaluated in terms of load-carrying capacity, axial and lateral displacements, strains in GFRP bars, spirals, and concrete, and failure modes. Since the column's axial capacity is sensitive to concrete strength, the measured loads were adjusted to eliminate the effect of varying concrete strength among tested columns. This is achieved by multiplying the measured load by the ratio of $38/f'_c$, where 38 MPa is the average of obtained concrete strength for all tested column. The adjusted column loads, listed in Table 4.1, were used in the analysis and discussion of results.

4.2 OBSERVED BEHAVIOUR, CRACKS PATTERN, LOAD CAPACITY AND MODE OF FAILURE

The GFRP-RC column G20-85-C00, tested under concentric load, failed in a sudden and explosive manner compared to those tested under eccentric and four-point bending loads. The peak load was 4,292 kN for the concentrically-loaded column. During the test, the first vertical crack was visually observed around the mid-height of the column at load of 2,446 kN, which corresponds to 57% of the peak load. At approximately 95% of the peak load, a large number of vertical cracks were developed on the concrete surface all around the column (Fig. 4.1a and b). Then, at the peak load, spalling of concrete cover started on one side of the column and then rapidly spread on the other sides. In this process, the load capacity suddenly dropped by 29% of the peak. After the concrete cover spalled, the GFRP spiral started confining the concrete core. As a result, the column started to pick up additional loads while the compressive stress in the concrete core and tensile strain in the GFRP spiral were increasing gradually. When the GFRP spirals reached rupture strain, the column failed suddenly, as shown in Fig. 4.1 (d, e, f and g), due to concrete core crushing and buckling of GFRP longitudinal bars followed by rupture of GFRP spiral and crushing of GFRP bars around mid-height. The failure mechanism of this column was similar to that reported by Afifi et al. (2014) and Hadhood et al. (2017b).

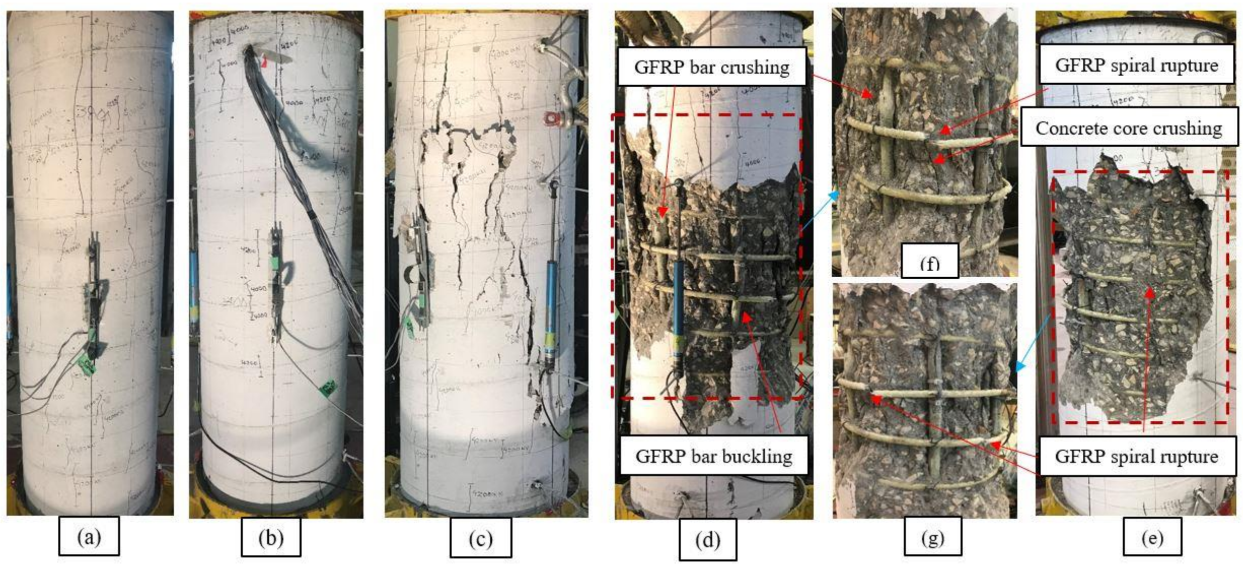

Fig. 4.1: Cracks pattern and mode of failure for concentrically-loaded short column G20-85-C00, (a) At the peak load - side 1, (b) At the peak load - side 2, (c) Concrete cover spalling at peak load - side 1, (d) Failure mode - side 1, (e) Failure mode - side 2, (f) Failure mode - close view to side 1, and (g) Failure mode - close view to side 2.

Columns S20-85-E30, G20-85-E30 and G20-50-E30 were tested under small eccentricity of 30 mm corresponds to the eccentricity-to-column diameter (*e/D*) ratio of 0.085. The peak loads were

3,501, 2,921 and 3,203 kN for columns S20-85-E30, G20-85-E30 and G20-50-E30, respectively. For the three columns, the first vertical crack was noticed on the compression side near mid-height. The first crack was visually observed at a load of 1,290, 1,250 and 1,360 kN for columns S20-85-E30, G20-85-E30, and G20-50-E30, respectively, which is approximately 37, 43 and 42% of respective peak loads. At approximately 80 to 90% of the peak loads, additional vertical cracks appeared on the compression side as shown in Fig. 4.2 (a). These cracks kept widening and new cracks formed on the compression side until maximum capacity was reached and the concrete cover spalling started around the mid-height. At the peak load stage, no flexural-tension cracks were noticed on the tension side as the column was fully under compressive stresses. With the drop in load-carrying capacity, a considerable amount of concrete spalled from the compression side was observed. All three columns experienced higher axial and lateral deformation, which induced higher secondary moments and tensile stresses on the tension side. As a result, flexural-tension cracks appeared rapidly along the length of the column on tension side as shown in Fig. 4.2 (b). When compressive strains in GFRP bars on the compression side and tensile strains in GFRP spirals reached the ultimate, both columns G20-85-E30 and G20-50-E30 failed suddenly in a brittle manner through rupturing of GFRP spirals and crushing of GFRP bars near column mid-height followed by concrete core crushing as shown in Fig. 4.3 (a). Failure of column G20-50-E30, with a 50-mm pitch, was less violent than that of G20-85-E30 with 85-mm pitch. The steel-RC column failed by concrete cover spalling at the peak followed by gradual yielding of the outermost tension and compression bars, and spirals along with concrete core crushing as shown in Fig. 4.3 (b).

Column G20-85-E60 was tested under a moderate eccentricity of 60 mm that corresponds to an *e/D* ratio of 0.17. The peak load was recorded at 2,599 kN, which is 39% less than the concentrically-loaded column G20-85-C00. The first vertical and horizontal flexural-tension cracks were noticed in the mid-height region at a load of 1,300 kN, which corresponds to 50% of the peak load. With the increasing load, the intensity of these cracks increased and propagated along the length of the column as shown in Fig. 4.2 (a and b).

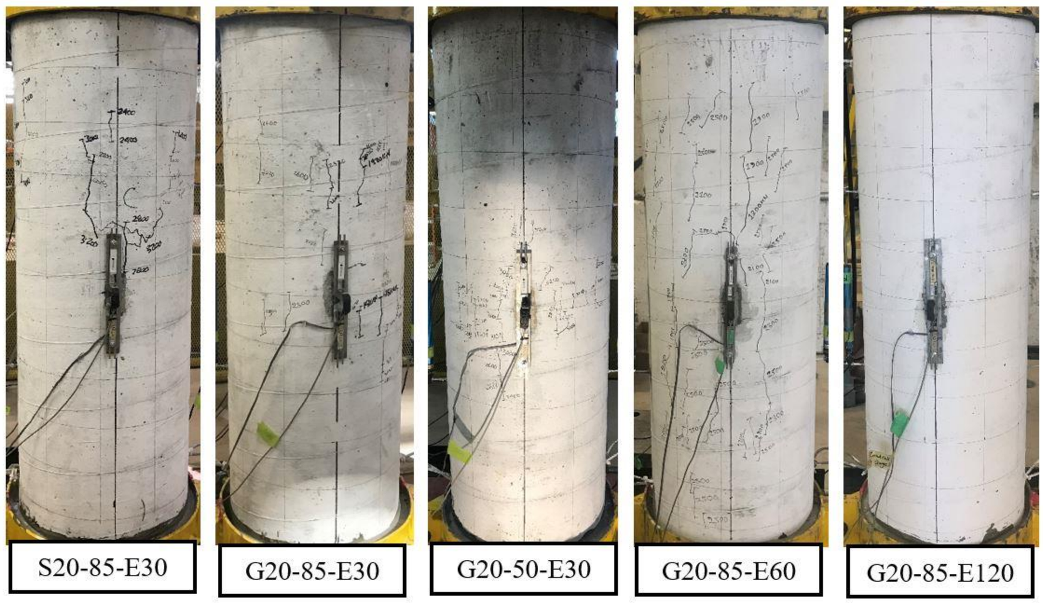

(a)

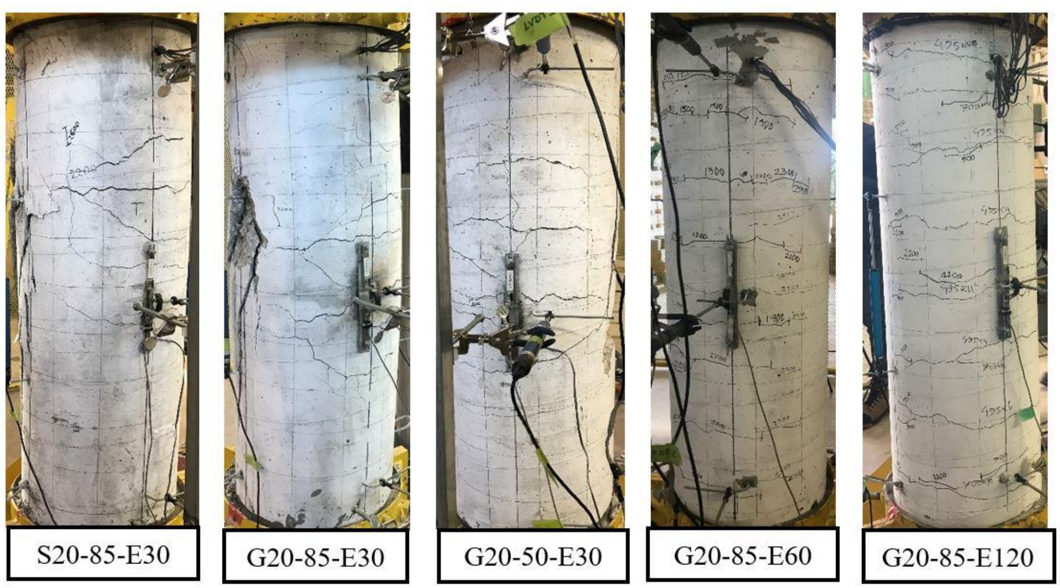

(b)

Fig. 4.2: Cracks pattern for eccentrically-loaded short columns: (a) On compression side at peak load; (b) On tension side at peak and post-peak load.

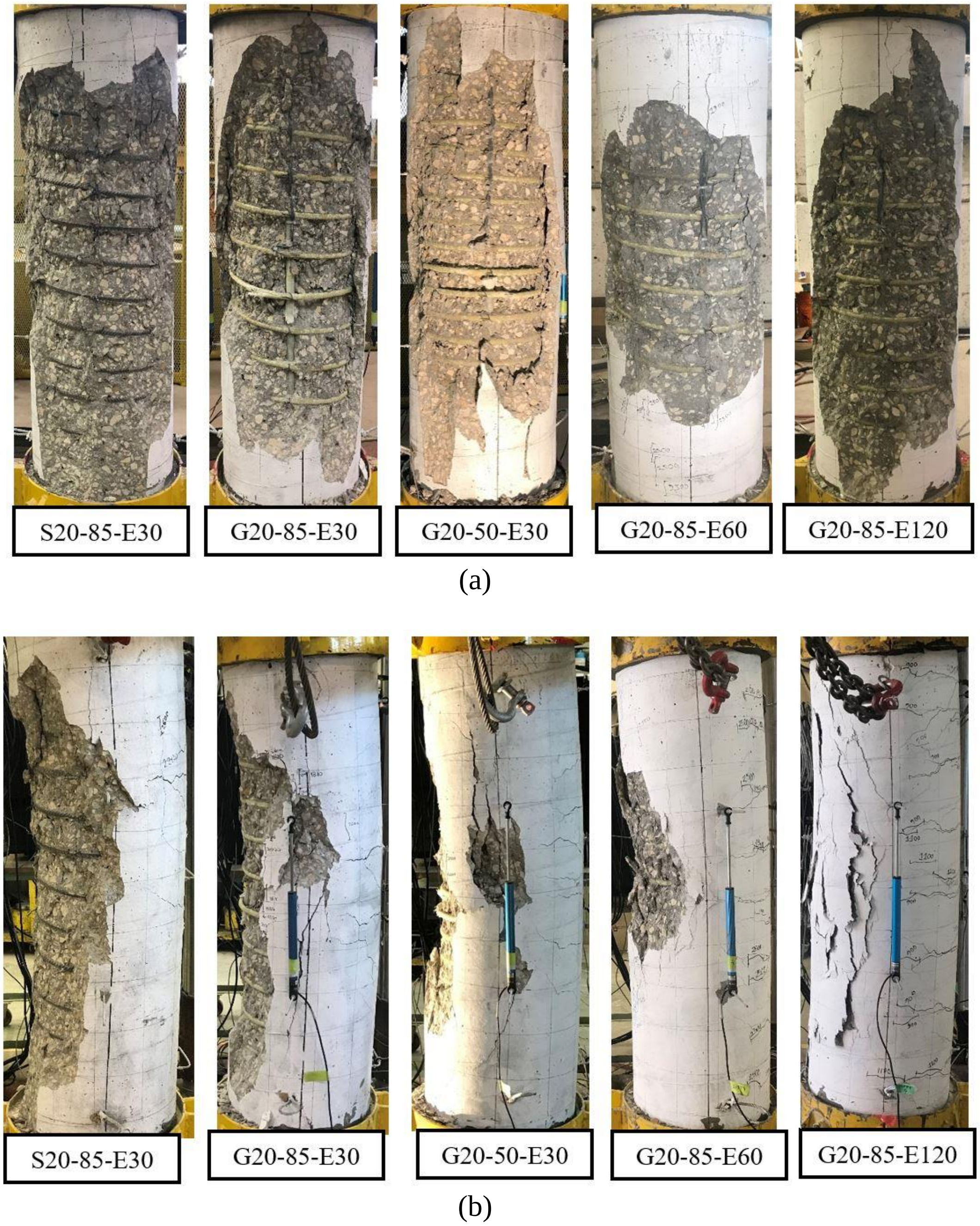

Fig. 4.3: Failure modes of short columns under eccentric loads, (a) Compression side, and (b) Side view.

When the concrete reached its ultimate strain, crushing and spalling of concrete occurred around mid-height of the column on the compression side and the capacity started to drop. At the end of the post-peak stage, no crushing of GFRP bars or rupture of GFRP spirals was noticed (Fig. 4.3a).

A similar type of failure mechanism was reported by Hadhood et al. (2017b) for the GFRP-RC column subjected to moderate eccentric loading. The test was stopped when the column capacity dropped by 25% from the peak.

For column G20-85-E120, subjected to higher eccentric loads (*e/D* = 0.34), several flexural-tension cracks were noticed on the tension side along the length of the column at an early stage of loading. The cracking load was 504 kN, which is about 39% of the load capacity of the column. With the increasing load, existing flexural-tension cracks propagated, and new cracks developed on the tension side as shown in Fig. 4.2 (b)**.** At the peak load of 1,300 kN, the specimen gradually failed by concrete crushing within the mid-height region followed by the spalling of concrete cover as shown in Fig. 4.3 (a and b). After the peak load, the axial and lateral deformations were rapidly increasing, which induced more secondary moments leading to higher strains in longitudinal GFRP bars and spirals. When the drop of the column capacity reached 25%, the test was stopped and no signs of GFRP bar crushing or rupture of GFRP spiral were noticed.

Column G20-85-F was tested under four-point bending loads in a simply-supported condition to determine the pure flexural capacity of the column. The first flexural-tension crack appeared at the mid-span between the two loading points at a load of 49 kN. As the load increased, new cracks developed between the loading points and along the shear span while the existing cracks propagated around the specimen. With further increased load, the cracks within the shear span propagated towards the loading points as shown in Fig. 4.4 (a). The specimen continued to carry load until the gradual concrete spalling started on the compression side at mid-span. The first peak load was 361 kN. Afterwards, a small drop from the first peak was observed but the specimen was able to sustain increased load. After the first peak, the spiral confinement was activated and the strains in the outermost compression and tension GFRP bars increased substantially. Excessive deformation with wider flexural cracks were visible as shown in Fig. 4.4 (c). Finally, the specimen failed when strains in the outermost tension bar reached its ultimate and ruptured. The second peak was recorded at 548 kN, which was approximately 50% higher than that of the first peak.

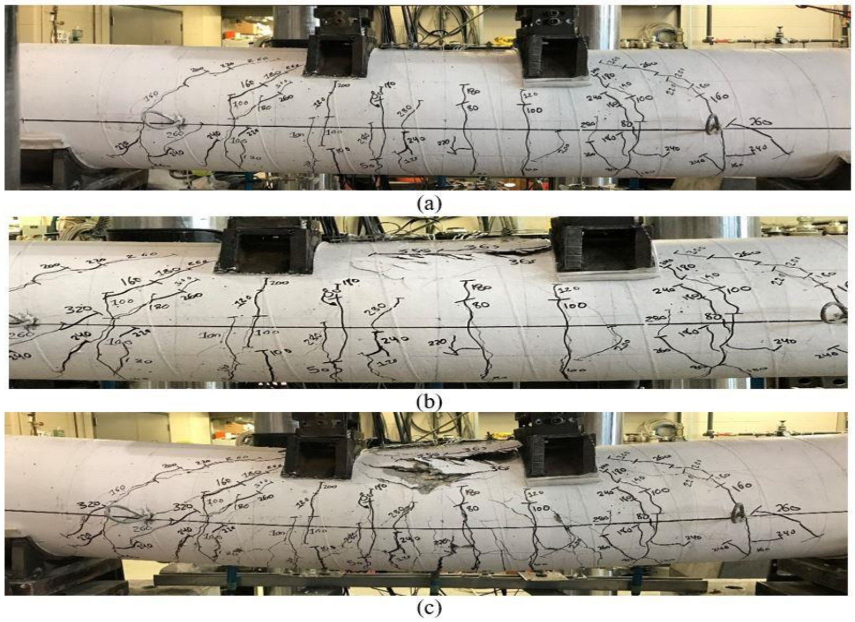

Fig. 4.4: Cracks pattern and failure mode of short column under four-point bending loads, (a) Crack formation pattern; (b) Concrete spalling at the first peak; and (c) Failure at the second peak.

4.3 AXIAL AND MID-HEIGHT LATERAL DISPLACEMENT RESPONSES

Unlike concentrically-loaded columns, the eccentrically-loaded ones had significant bending at the mid-height, which resulted in inaccurate and inconsistent LVDTs readings. Therefore, only the total axial displacements measured by loading machine head are considered. At early loading stages, the axial displacements increased at a very low rate (Fig. 4.5). With the increasing load, micro-cracks were developed in the concrete core that led to a gradual loss of initial axial stiffness of columns and consequently higher axial displacement. Under the same *e/D* ratio of 0.085, column G20-85-E30 experienced 6% higher axial displacement than the steel-RC counterpart S20-85-E30 at the peak loads. This was expected due to the lower elastic modulus of GFRP bars compared to steel. However, column G20-50-E30 with 50-mm pitch exhibited 3% lower axial displacements than column G20-85-E30 with 85-mm pitch at the peak. The maximum recorded axial displacements at peak were 10.0, 10.7, 8.4 and 7.8 mm for columns G20-85-C00, G20-85-E30, G20-85-E60, and G20-85-E120, respectively. It was found that the axial displacement at peak load reduced as the *e/D* ratio increased. At the post-peak stage, axial displacement kept increasing as the capacity reduced gradually. The maximum recorded axial displacement at failure was 16.7, 13.8 and 17 mm for columns G20-85-E30, G20-85-E60, and G20-85-E120, respectively.

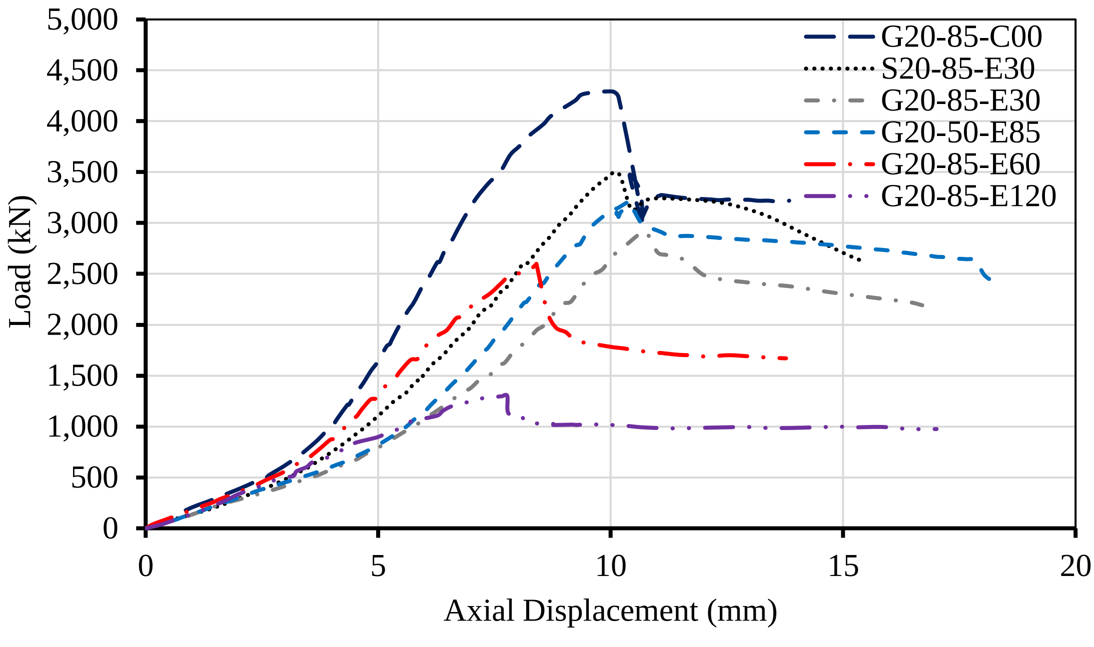

Fig. 4.5: Axial displacement responses for short columns under concentric and eccentric loads.

The lateral displacement behaviour was similar to the axial displacement response for columns under eccentric loads as shown in Fig. 4.6. Under the same *e/D* ratio of 0.085, column G20-85-

E30 showed 67% higher lateral displacement than the steel-RC counterpart S20-85-E30 at the peak load. Again, this was expected because of the lower stiffness of GFRP bars compared to steel. Specimen G20-50-E30 with 50-mm pitch exhibited 5% lower lateral deflection than G20-85-E30 with 85-mm pitch at the peak load. As the eccentricity increased, the GFRP-RC columns experienced higher mid-height lateral deflection at the peak load due to more primary and secondary moments acting on the column. At the peak load, increasing the eccentricity from 30 mm (G20-85-E30) to 60 mm (G20-85-E60) and further to 120 mm (G20-85-E120) resulted in 33 and 130% increase in lateral displacement, respectively. In the post-peak stage, lateral displacement kept increasing gradually until failure. At failure, the maximum lateral displacements were 32, 35 and 41 mm for columns G20-85-E30, G20-85-E60, and G20-85-E120, respectively.

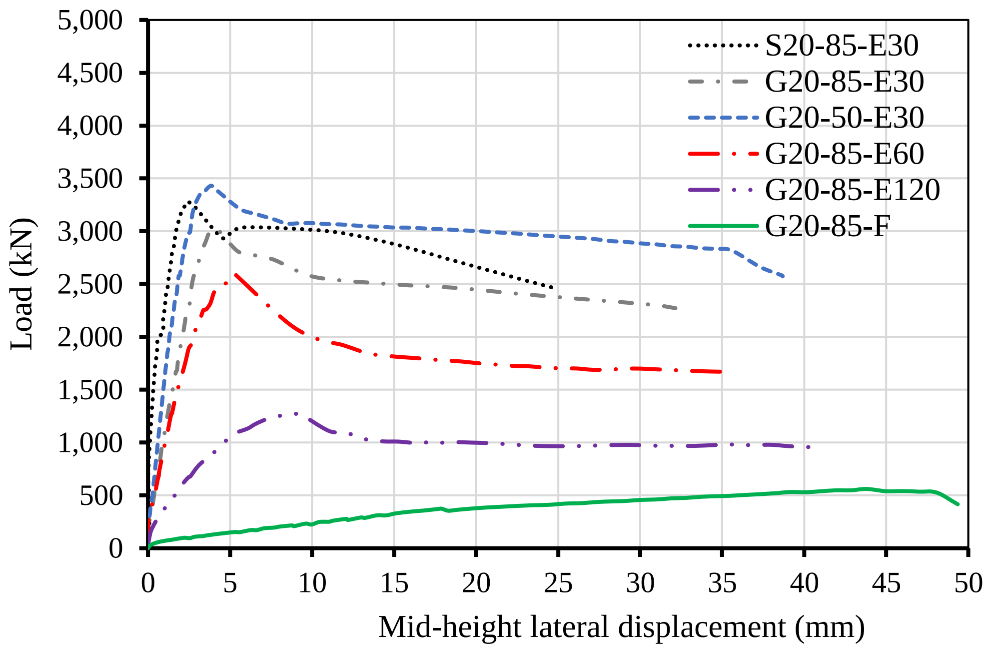

Fig. 4.6: Mid-height lateral displacement responses for short columns under eccentric and four-point bending loads.

For column G20-85-F, the load-lateral displacement relationship was bi-linear, as shown in Fig. 4.6. The first line represents the stiffness of the uncracked specimen, while the second line with less slope started when the first flexural-tension crack developed within the mid-span region. The maximum mid-length lateral displacement was 18 mm at the peak load and 49 mm at failure.

4.4 STRAIN PROFILES OF LONGITUDINAL STEEL AND GFRP BARS

Axial strains, shown in Fig. 4.7, were measured at mid-length of the outermost longitudinal GFRP and steel bars, where maximum compressive and tensile stresses were expected. At early loading stages, strains in the outermost longitudinal bars started to increase slowly. After development of micro-cracks and flexural-tension cracks on compression and tension sides, the bar strains increased gradually up to the peak load. For the concentrically-loaded column G20-85-C00, the cross-section was fully under compressive stresses up to failure. At the peak load, compressive strains of -3,900 and -2,680 micro-strains were recorded in the outermost longitudinal GFRP bars. Significant concrete cover spalling and concrete core dilation at the post-peak stage activated the confining pressure of the GFRP spiral leading to buckling and crushing of GFRP bars and rupture of spiral around mid-height of the column. The maximum recorded compressive strains, before gauge damage, were -9,920 and -10,290 micro-strains.

Similarly, columns S20-85-E30, G20-85-E30 and G20-50-E30, with e/D = 0.085, were also under compression up to the peak load. At peak load, the measured strains in the outermost longitudinal bars on compression side were -2,380, -4,090, and -5,660 micro-strains for S20-85-E30, G20-85-E30 and G20-50-E30, respectively. These values were -420, -720 and -240 micro-strains in the outermost bars on tension side, respectively. When columns reached their maximum capacity, spalling of the concrete cover reduced the stiffness causing more bending stresses on both tension and compression sides. As a result, strains in the outermost longitudinal bars on tension side changed from compression to tension and then progressively increased. At the post-peak stage for columns G20-85-E30 and G20-50-E30, most of the concrete cover was lost and the confinement of concrete core was activated, which was followed by concrete core crushing accompanied by crushing of GFRP longitudinal bars and rupture of spirals on the compression side of the column. Maximum strains recorded for the outermost GFRP longitudinal bars on the compression side were -18,620 and -20,210 micro-strains for column G20-85-E30 and G20-50-E30, respectively, before gauge malfunctioned. Similar strain values were reported by Hadhood et al. (2017b). The highest tensile strains in the outermost GFRP longitudinal bars, measured at failure, were 14,480 and 15,450 micro-strains, for column G20-85-E30 and G20-50-E30, respectively. However, for steel-RC column S20-85-E30, the maximum measured strains in the outermost compression and tension longitudinal bars were -20,930 and 20,110 micro-strains, respectively with a well-defined yielding plateau.

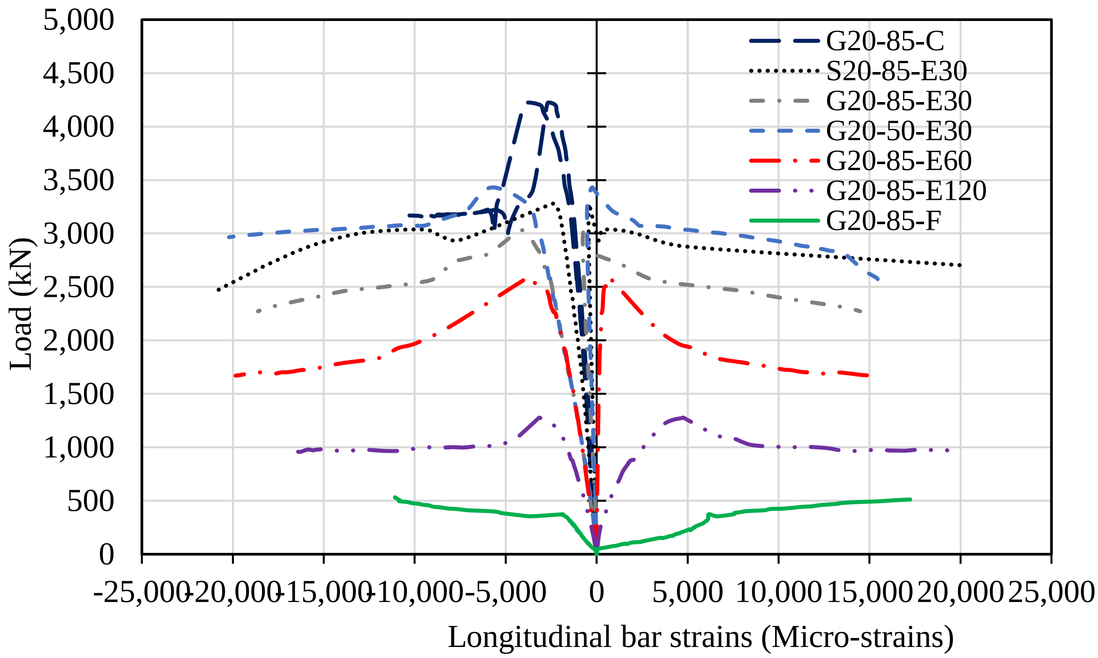

Fig. 4.7: Strain profiles of outermost longitudinal steel and GFRP bars (Series I).

When tested under moderate eccentricity (*e/D* = 0.17), most of the cross-section area of column G20-85-E60 was under compressive stresses, only a small area was experiencing tensile stresses. At the peak load, strains obtained in the outermost compression and tension longitudinal GFRP bars were −3,690 and 650 micro-strains, respectively. These values increased to −19,860 and 15,160 micro-strains, respectively, at failure. On the other hand, nearly half of the section of column G20-85-E120 tested with higher eccentricity (*e/D* = 0.34) was in compression and the rest in tension. At maximum capacity, the recorded strains in the outermost longitudinal GFRP bars on the compression and tension sides were −3,160 and 4,760 micro-strains, respectively. At failure, these values reached −16,410 and 19,480 micro-strains, respectively, with substantial concrete cover spalling and excessive lateral deformation.

For column G20-85-F tested under four-point bending loads, strains in the outermost longitudinal GFRP bars increased substantially after the development of flexural cracks in the tension zone. At the first peak, recorded strains were -1,850 and 6,160 micro-strains in the outermost GFRP longitudinal bars on compression and tension sides, respectively. After the first peak, the capacity of the column slightly reduced due to the concrete cover spalling in the compression zone between the two loading points. Then the specimen was able to carry increased load along with excessive deformation and widening of flexural-tension cracks. In the meantime, strains in GFRP longitudinal bars and spirals were increasing until the second peak was reached. At the second peak, the outermost GFRP longitudinal bar on the tension side ruptured and the capacity of the section dropped suddenly. The highest recorded strains in the outermost longitudinal bars on compression and tension sides were −11,090 and 17,240 micro-strains, respectively, before gauges were malfunctioned. Similar strain values were reported by Mousa et al. (2018).

4.5 STRAIN PROFILES OF STEEL AND GFRP SPIRALS

Spiral strains, shown in Fig. 4.8 and 4.9, were recorded at two opposite sides of a turn located at the column mid-height, where maximum bending stresses were expected. Initial slopes of strain profiles for all columns were similar and the strains measured were minimal at the early loading stage. Up to the peak load, strains in the GFRP spiral of the concentrically-loaded column G20-85-C00 increased slowly. At the peak load, maximum tensile strains recorded in the GFRP spiral were 1,520 and 910 micro-strains at two opposite sides which are only 13 and 8% of its ultimate tensile strain. After a considerable amount of concrete cover spalling in the post-peak stage, dilation of core concrete followed by micro-crack propagation activated the confining pressure of the GFRP spirals and strains stated increasing at a faster rate till rupture. At failure, maximum tensile strains recorded in the GFRP spiral were 9,950 and 8,410 micro-strains at two opposite sides, which represent about 87 and 74% of the rupture strain.

The cross-section of columns S20-85-E30, G20-85-E30 and G20-50-E30, tested with low eccentricity (*e/D* = 0.085), experienced non-uniform compressive stresses up to the peak load at which the maximum recorded spiral strains were 580, 2,430 and 3,140 micro-strains, respectively. Once concrete cover was lost and the confinement of the concrete core started to activate, strain gauges recorded a significant increase in spiral strains at post-peak stages that reached 6,070, 4,730 and 10,490 micro-strains on the compression side for columns S20-85-E30, G20-85-E30 and G20-50-E30, respectively. GFRP-RC columns, G20-85-E30 and G20-50-E30, had a sudden brittle failure due to rupture of GFRP spirals around column mid-height. On the other hand, the steel-RC column failed gradually by yielding of steel spiral. It was found that, under low eccentric loads, the GFRP-RC column confined with a 50-mm spiral pitch was able to enhance the peak load by

10% more than its counterpart with an 85-mm pitch. In addition, the steel-RC column showed a 17% higher capacity than the GFRP-RC counterpart column.

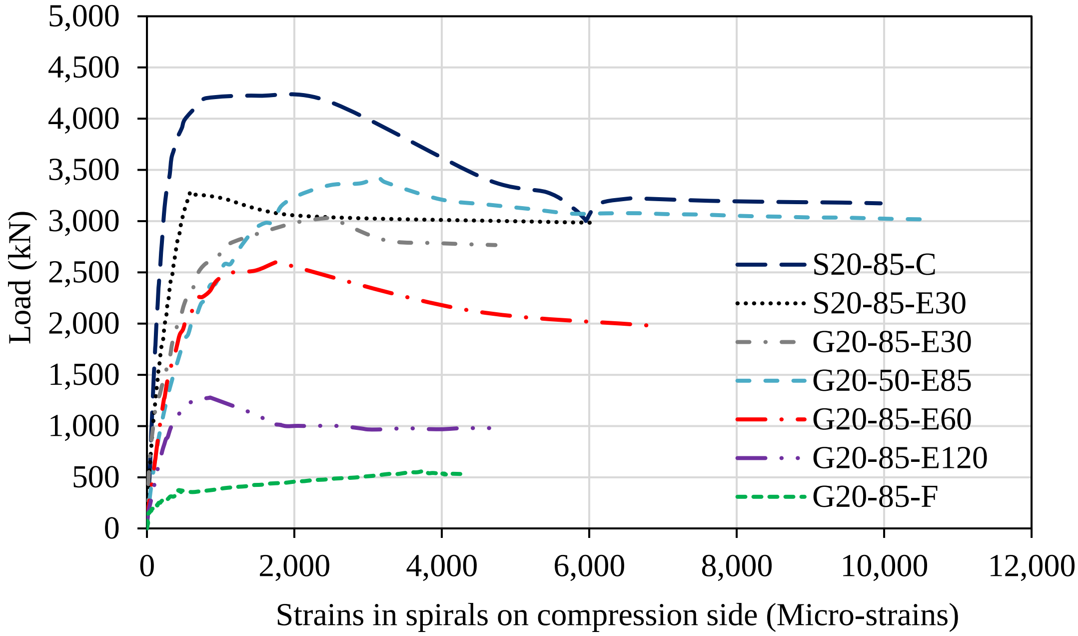

Fig. 4.8: Strain profiles of spirals on compression sides at the mid-height (Series I).

The GFRP spiral was able to prevent buckling of longitudinal bars up to the peak load, then it was able to effectively confine the concrete core at the peak and post-peak stages without any rupture for columns G20-85-E60 and G20-85-E120 tested under the moderate and high *e/D* ratio of 0.17 and 0.34, respectively. Since the amount of concrete under compression was less than the previous cases, strains in GFRP spirals at the peak lower than those measured for columns under concentric and small eccentric loads. At the peak load, strains in GFRP spirals measured on compression sides were 1,770 and 860 micro-strains for column G20-85-E60 and G20-85-E120, respectively. At failure, these values were 6,910 and 4,810 micro-strains, respectively. For column G85-F, tested under four-point bending loads, the maximum measured strain in the GFRP spiral on the compression side was 440 micro-strains at the first peak load (361 kN). However, this value was 4,250 micro-strains at failure (548 kN), which indicates the effectiveness of the GFRP spiral in significantly enhancing the load-carrying capacity without rupture.

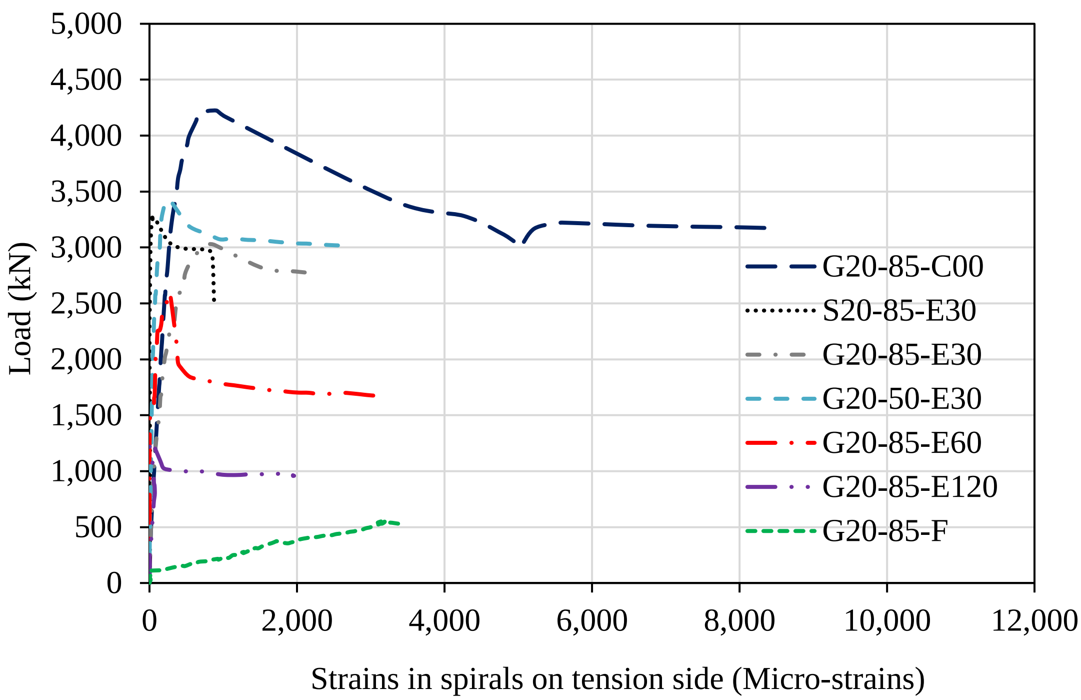

Fig. 4.9: Strain profiles of spirals on tension sides at the mid-height (Series I).

Strain profiles of spirals on tension sides were also affected by the applied loading types. Spiral confinement was activated after the propagation of micro-cracks and flexural-tension cracks. At the peak load, recorded spiral strains on tension side of the column were minimal for columns tested under small, moderate and large eccentricities (*e/D* = 0.085, 0.17 and 0.34), and the spiral confinement was not yet activated. After the peak, micro-cracks and flexural-tension cracks quickly propagated on tension side. As a result, strains in the outermost longitudinal bars increased. Similarly, strains in spirals increased as a result of providing lateral support to the concrete core.

The maximum strains recorded at failure were 880, 2,780, 4,170, 3,200 and 1,960 micro-strains for columns S20-85-E30, G20-85-E30, G20-50-E30, G20-85-E60 and G20-85-E120, respectively. Strains in the outermost longitudinal GFRP bar of the column G20-85-F increased significantly after the first peak. The spiral reacted to provide lateral supports for the GFRP longitudinal bars and strains in the GFRP spiral increased significantly. The measured spiral strains for column G20-85-F were 1,720 and 4,250 micro-strains at the peak load and at failure, respectively.

4.6 CONCRETE COMPRESSIVE STRAIN RESPONSES

At early loading stages, the load-concrete strain relationship was approximately linear, as shown in Fig. 4.10. With the increasing load, micro-cracks and/or flexural-tension cracks developed and the concrete strain graphs started to diverge for columns subjected to different loading types and eccentricities. After that, concrete strains increased non-linearly until it reached the crushing strain and columns reached their maximum capacity.

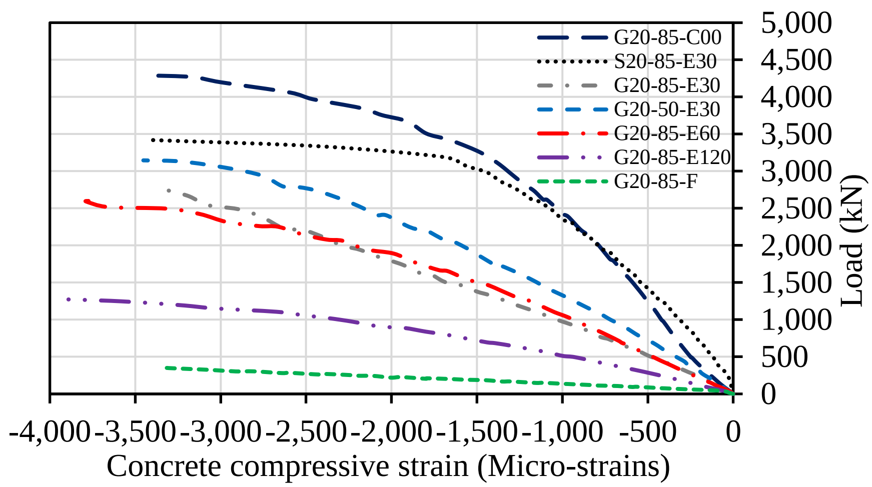

Fig. 4.10: Concrete compressive strain responses at the mid-height (Series I).

The maximum concrete compressive strain recorded at the peak load was -3,450, -3,420, -3,390, -3,380, -3,770, -3,890 and -3,330 micro-strains for columns G20-85-C, S20-85-E30, G20-85-E30, G20-50-E30, G20-85-E60, G20-85-E120 and G20-85-F, respectively, which are close to the specified design limit of -3,500 micro-strains (CSA 2017).

4.7 NORMALIZED INTERACTION DIAGRAM FOR SHORT COLUMN

Fig. 4.11 shows the normalized interaction diagram along with the load path for the GFRP-RC columns tested under concentric, eccentric and four-point bending loads. The difference between the two lines is the point obtained form the pure flexure test. The dotted line represents the first peak moment for the test specimen while the solid line represents the second peak moment for the specimen. It is to be mentioned that the same behavior (the two peaks) was reported by Mousa et al. (2018) for flexural behavior of circular members.

The normalized axial force (K_n) and the normalized bending moment (R_n) are given by:

$$K_n = \frac{P_n}{A_g f'_c} \qquad \text{Eq. 4.1}$$

$$R_n = \frac{M_n}{A_g f'_c D} \qquad \text{Eq. 4.2}$$

$$M_n = M_{n_1} + M_{n_2} = (P_n \times e) + (P_n \times \delta_n) \qquad \text{Eq. 4.3}$$

The value of $\mathrm{P_n}$ is defined as the ultimate nominal peak load and δ_n is the measured lateral mid-height displacement at the peak. The nominal primary moments M_{n_1} are based on the initial applied eccentricity (e), and the nominal secondary moments M_{n_2} are based on the measured lateral mid-height displacement at the peak load as mentioned in Table 4.1, *Ag* is the gross sectional area, f'_c is the average cylindrical concrete compressive strength, and *D* is the overall column diameter. Circular GFRP-RC short columns exhibited a “knee” shaped interaction diagram similar to the steel-RC columns in which the moment resistance increases as the axial capacity decreases until the inflection point is reached, known as the balance point for steel-RC columns. A similar “knee” shaped interaction diagram for GFRP-RC circular columns was reported by Hadhood et al.

(2017b). Results show that, as the *e/D* ratio increased from 0.085 (column G20-85-E30) to 0.17 (column G20-85-E60), the axial capacity was decreased by 11% and the moment capacity was increased by 72%. However, when the *e/D* ratio increased from 0.17 (column G20-85-E60) to 0.34 (column G20-85-E120), the axial and moment capacity was decreased by 50% and 1%, respectively. Therefore, after the inflection point, axial and flexural resistances started to decrease simultaneously. This point is known to establish the compression and tension-controlled regions for steel-RC columns. The axial capacity decreased by 32, 39 and 70% for columns G20-85-E30, G20-85-E60, and G20-85-E120, respectively compared to column G20-85-C00 as the *e/D* ratio increased from 0 to, 0.085 and further to 0.34. The pure flexure point obtained from second peak load was recorded approximately 52% higher than that of the first peak load. The solid line is in good agreement with the findings of the previous research studies (Mirmiran et al., 2001; Karim et al. 2017)

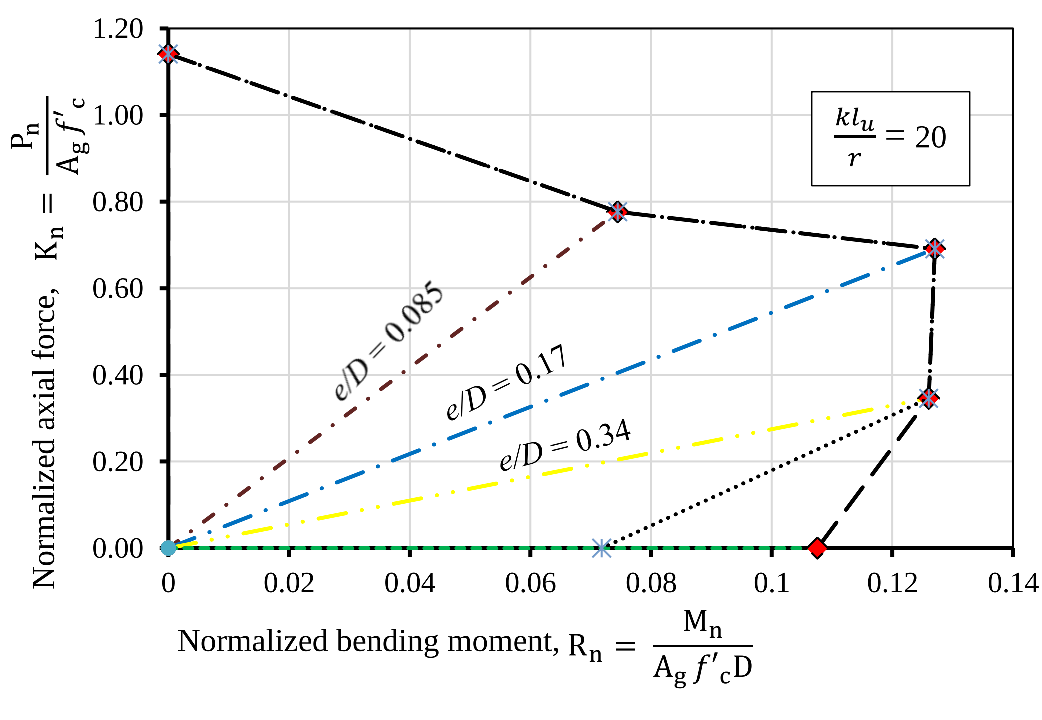

Fig. 4.11: Normalized interaction diagram for GFRP-RC circular short column

Table 4.1: Experimental test results for short columns (Series I)

Specimen ID	e (mm)	P_n (kN)	P_n (38/f'_c) (kN)	δ_n (mm)	Δ_n (mm)	M_{n1} (kN.m)	M_{n2} (kN.m)	M_n (kN.m)
						$P_n \times e$	$P_n \times \Delta_n$	$M_{n1} + M_{n2}$
G20-85-C00	0	4,224	4,292	-	10.0	0	0	0
S20-85-E30	30	3,280	3,501	2.4	10.1	105	8	113
G20-85-E30	30	3,029	2,921	4.0	10.7	87	12	99
G20-50-E30	30	3,431	3,203	3.8	10.4	96	12	108
G20-85-E60	60	2,599	2,599	5.3	8.4	156	14	170
G20-85-E120	120	1,278	1,300	9.2	7.8	160	12	168
G20-85-F	-	369[a](561[b])	361[a](548[b])	17.9	-	-	-	95[c](144[c])

[a] First peak load
[b] Second peak load

[c]$M_n = (P_n/2) \times$ Shear span

CHAPTER 5 – RESULTS AND DISCUSSION OF SERIES II

5.1 GENERAL

In this chapter, the test results of six large-scale steel and GFRP-RC slender columns (Series II) are presented and discussed. All slender columns measured 355 mm in diameter, and 2,450 mm in length. One out of six slender columns (Series II) was tested under concentric loads; four were tested with varying eccentricity-to-column diameter ratios (e/D = 0.085, 0.17, and 0.34); and the last one was tested under four-point bending loads. Structural performance of these tested columns are evaluated in terms of load-carrying capacity, axial and lateral displacements, strains in GFRP bars, spirals, and concrete, and failure modes. Since the column's axial capacity is sensitive to concrete strength, the measured loads were adjusted to eliminate the effect of varying concrete strength among tested columns. This is achieved by multiplying the measured load by the ratio of $36/f'_c$, where 36 MPa is the average of obtained concrete strength for all tested column. The adjusted column loads, listed in Table 5.1, were used in the analysis and discussion of results.

5.2 OBSERVED BEHAVIOUR, CRACK PATTERN, LOAD CAPACITY AND MODES OF FAILURE

The GFRP-RC slender column G28-85-C00 tested under concentric loads failed in a sudden and explosive manner, similar to the short column G20-85-C00. The peak load was 3,231 kN for the concentrically-loaded column. During the test, the first vertical compression crack was visually observed around the mid-height of the column at 1,110 kN load, which corresponds to 34% of the peak load. As the load increased, more vertical cracks appeared along the length of the column. At approximately 96% of the peak load, a large number of vertical cracks was developed on the concrete surface all around the column (Fig. 5.1a and b). Then, at the peak, spalling of concrete cover started on one side of the column and then rapidly spread on the other sides. In this process, the load capacity suddenly dropped by 9% from the peak. After the concrete cover spalled, the GFRP spiral started confining the concrete core. As a result, the column started to pick up additional loads while the compressive stress in the concrete core and tensile strain in the GFRP spiral were increasing gradually. When the GFRP spirals reached rupture strain, the column failed suddenly, as shown in Fig. 5.1 (d, e, f and g), due to concrete core crushing and buckling of GFRP longitudinal bars followed by rupture of GFRP spiral and crushing of GFRP bars around mid-height.

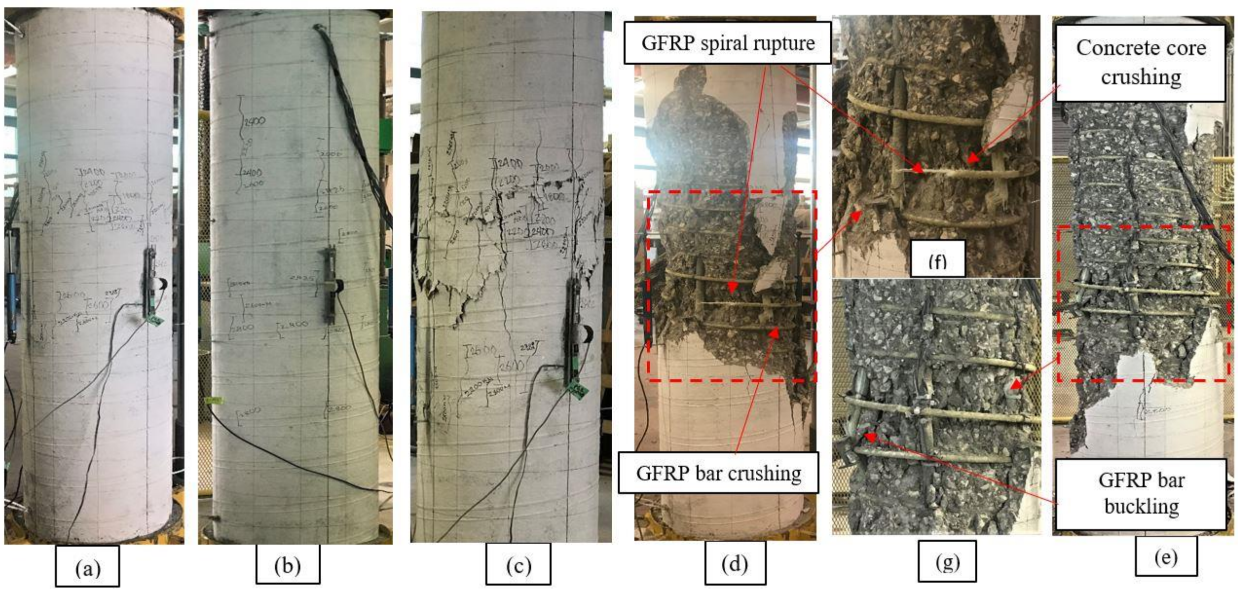

Fig. 5.1: Crack pattern and failure mode of concentrically-loaded slender column (G28-85-C00), (a) At the peak load (side 1); (b) At the peak load (side 2); (c) Concrete cover spalling at peak load (side 1); (d) Failure mode (side 1); (e) Failure mode (Side 2); (f) Failure mode (Close view to side 1); (g) Failure mode (Close view to side 2).

Columns S28-85-E30 and G28-85-E30 were tested under small eccentricity of 30 mm corresponds to the eccentricity-to-column diameter (*e/D*) ratio of 0.085. The peak loads were 2,221 and 2,279 kN for columns S28-85-E30 and G28-85-E30, respectively. For both steel and GFRP-RC column, no cracks were visible prior to cover spalling at the peak load (Fig. 5.2a). At peak load of 2,221 and 2,279 kN, concrete cover started to spall around mid-height of the column S28-85-E30 and G28-85-E30, respectively. At the peak load stage, no flexural-tension cracks were noticed on the tension side as the column was fully under compressive stresses. With the drop in load-carrying capacity, a considerable amount of concrete spalled from the compression side was observed. Both the columns experienced higher axial and lateral deformation, which induced higher secondary moments and tensile stresses on the tension side. As a result, flexural-tension cracks appeared rapidly along the length of the column on tension side as shown in Fig. 5.2 (b). At the end of the post-peak stage, no crushing of GFRP bars or rupture of GFRP spirals was noticed for the slender column G28-85-E30 (Fig. 5.3a) unlike the short column G20-85-E30. The GFRP-RC slender column G28-85-E30 failed gradually, whereas, the short column G20-85-E30 failed in a sudden and explosive manner. However, the steel-RC column failed by concrete cover spalling at the peak followed by gradual yielding of the outermost tension and compression bars, and spirals along with concrete core crushing as shown in Fig. 5.3 (b).

Column G28-85-E60 was tested under a moderate eccentricity of 60 mm that corresponds to an *e/D* ratio of 0.17. The peak load was recorded at 2,042 kN, which is 37% less than the concentrically-loaded column G28-85-C00. Several vertical and the first horizontal flexural-tension cracks were noticed in the mid-height region at a load of 1,975 kN, which corresponds to 97% of the peak load. With the increasing load, the intensity of these cracks increased and propagated along the length of the column as shown in Fig. 5.2 (a and b). When the concrete reached its ultimate strain, crushing and spalling of concrete occurred around mid-height of the column on the compression side and the capacity started to drop. At the end of the post-peak stage, no crushing of GFRP bars or rupture of GFRP spirals was noticed (Fig. 5.3a). A similar type of failure mechanism was noticed for the GFRP-RC short column G20-85-E60 subjected to the same moderate eccentric loading. The test was stopped when the column capacity dropped by 25% from the peak.

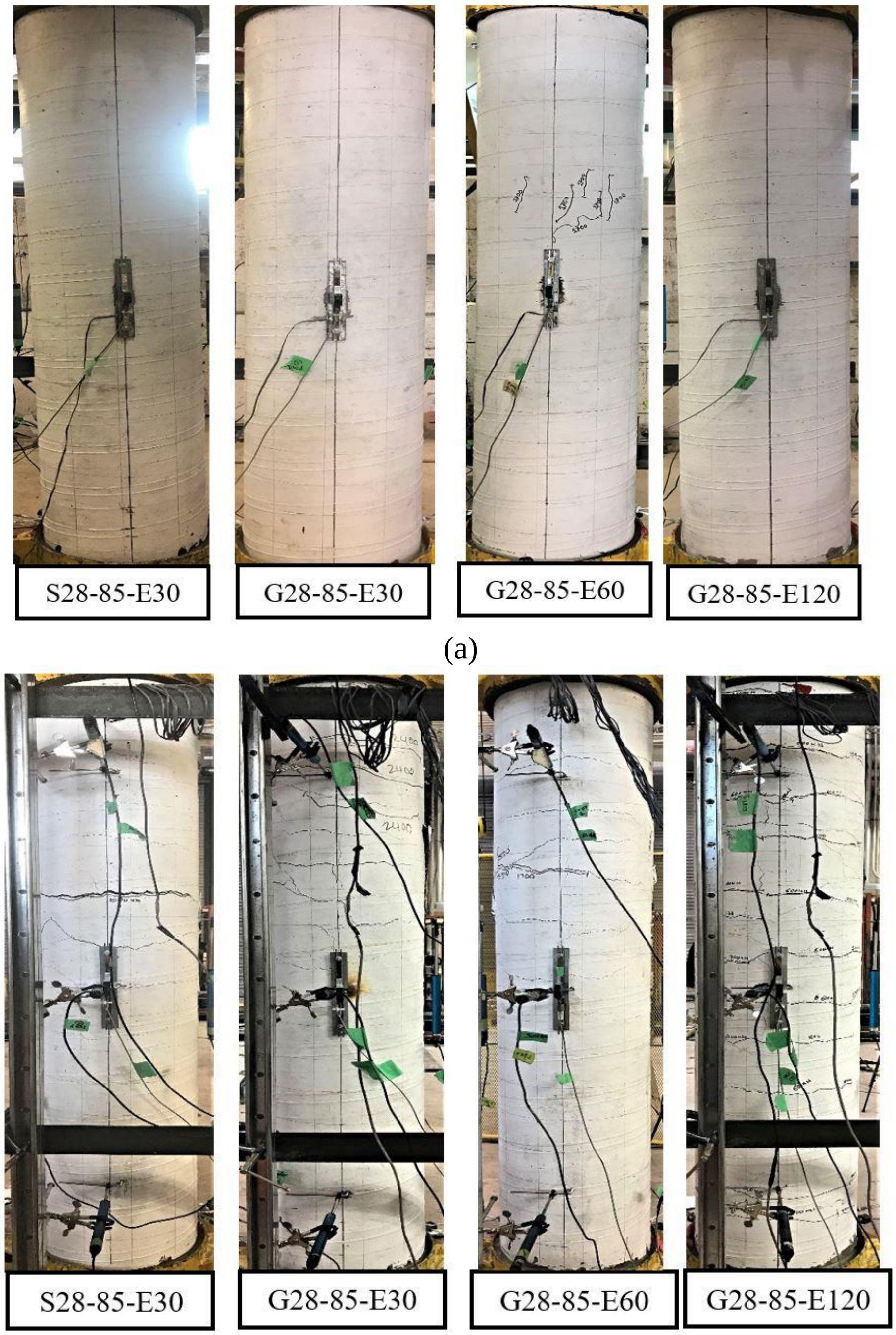

(b)

Fig. 5.2: Crack pattern for eccentrically-loaded slender columns: (a) On compression side at peak load; (b) On tension side at peak and post-peak load.

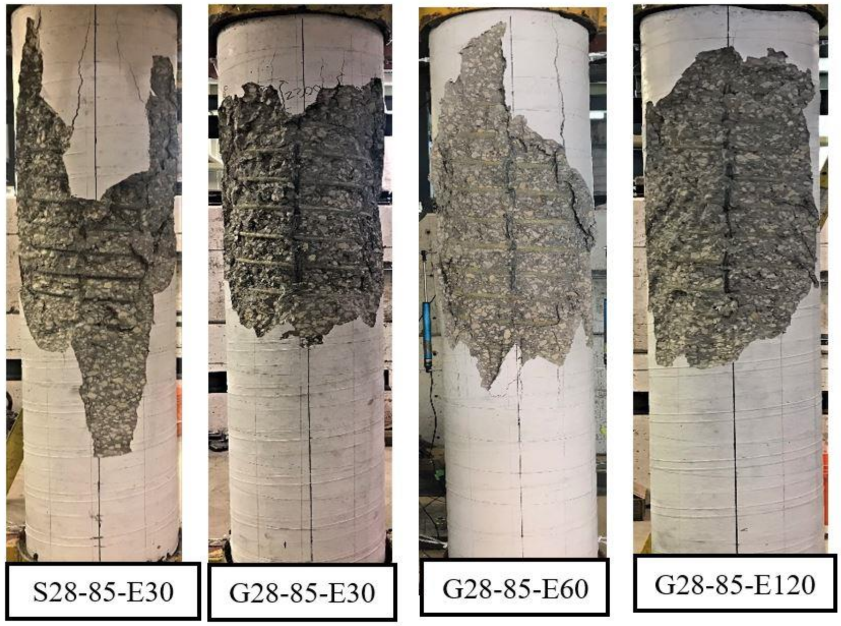

(a)

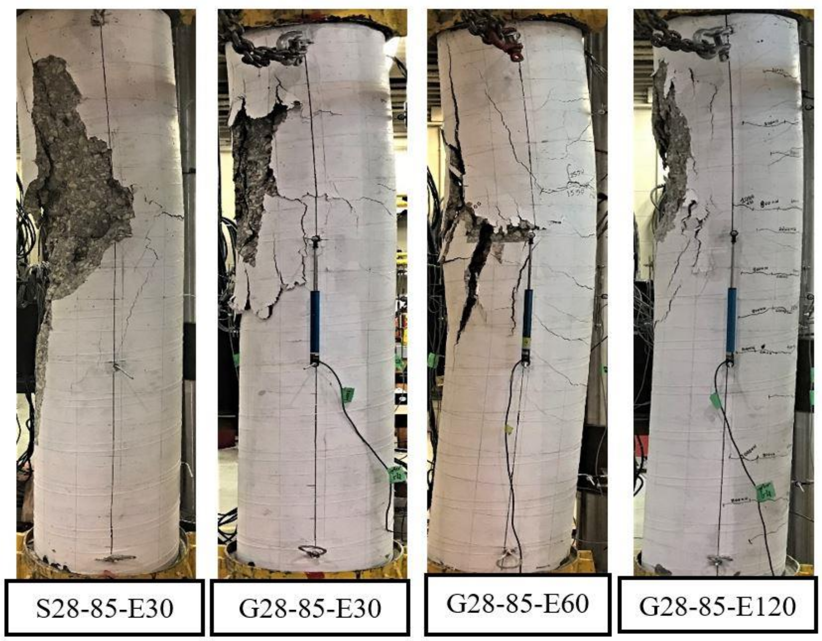

(b)

Fig. 5.3: Failure modes of slender columns under eccentric loads: (a) Compression side, and (b) Side view.

Several flexural-tension cracks were noticed on the tension side along the length of the column at an early stage of loading for the slender column G28-85-E120 subjected to higher eccentric loads (*e* =120 mm; *e/D* = 0.34). The cracking load was 338 kN, which is about 34% of the load capacity of the column. With the increasing load, existing flexural-tension cracks propagated, and new cracks developed on the tension side as shown in Fig. 5.2 (b). At the peak load of 992 kN, the specimen gradually failed by concrete crushing within the mid-height region followed by the spalling of concrete cover as shown in Fig. 5.3 (a and b). Before the crushing of concrete, the concrete surface on the compression side was completely free from any visible cracks. After the peak, strength decay started with progressive axial and lateral deformation inducing more secondary moments leading to higher strains in longitudinal GFRP bars and spirals. After considerable concrete spalling on the compression side, the test was stopped and no sign of rupture of GFRP bars and spiral was noticed. The failure mechanism was noticed similar to the short column G20-85-E120.

Column G28-85-F was tested under four-point bending loads in a simply-supported condition to determine the pure flexural capacity of the specimen. The first flexural-tension crack appeared at the mid-span between the two loading points at 30 kN, which is corresponding to 15% of the first peak load on the tension side when the concrete reached its tensile strength. As the load increased, new cracks developed between the loading points and along the shear span while the existing cracks propagated around the specimen. With further increased loads, the cracks within the shear span propagated towards the loading points as shown in Fig. 5.4 (a). The specimen continued to carry loads until the gradual concrete spalling started on the compression side at the mid-span. The first peak was 192 kN. Afterwards, a small drop from the peak was observed and again the specimen was able to sustain increased loads. At the post-peak stage, the spiral confinement was activated and the strains in the outermost compression and tension GFRP bars increased substantially. Degradation of the concrete compression block, excessive deformation with wider flexural cracks were visible as shown in Fig. 5.4 (c). The specimen carried load until strains in the outermost tension bar reached its ultimate strain and ruptured. The second peak was recorded at 286 kN, which was 49% higher than that of the first peak. Similar failure pattern was observed for the short column G20-85-F.

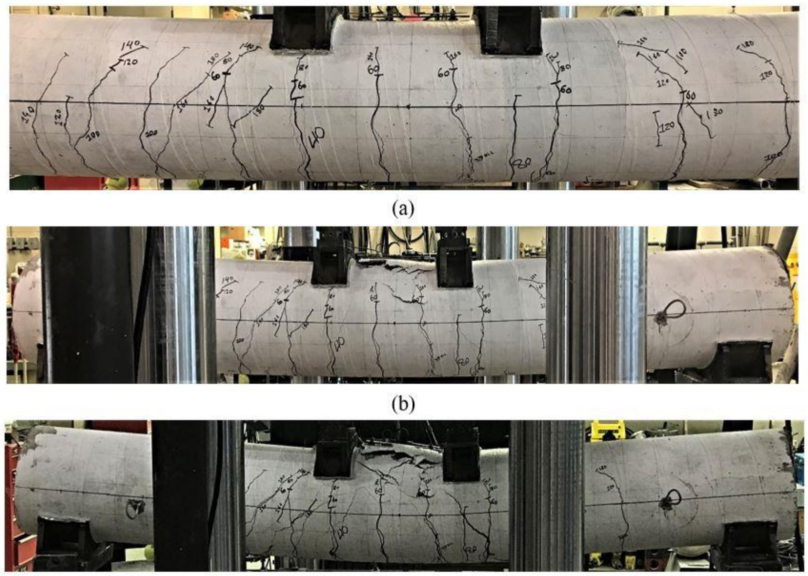

(a) (b) (c)

Fig. 5.4: Crack formation and failure mode of slender column under four-point bending loads, (a) Crack formation pattern; (b) Concrete spalling at the first peak; and (c) Failure at the second peak.

5.3 AXIAL AND MID-HEIGHT LATERAL DISPLACEMENT RESPONSES

Eccentrically-loaded columns had significant bending at the mid-height unlike the concentrically-loaded one, which resulted in inaccurate and inconsistent LVDTs readings. Therefore, only the total axial displacements measured by loading machine head are considered. At early loading stages, the axial displacements (Series II) increased at a very low rate (Fig. 5.5). With the increasing load, micro-cracks were developed in the concrete core that led to a gradual loss of initial axial stiffness of columns and consequently higher axial displacement. Under the same *e/D* ratio of 0.085, column G28-85-E30 experienced 25% higher axial displacement than the steel-RC counterpart S28-85-E30 at the peak loads. This was expected due to the lower elastic modulus of GFRP bars compared to steel. The maximum recorded axial displacements at failure were 12, 10, 9 and 9 mm for slender columns G28-85-C00, G28-85-E30, G28-85-60, and G28-85-E120, respectively. At the post-peak stage, axial displacement kept increasing as the capacity reduced gradually. The maximum recorded axial displacement at failure was 25, 16 and 19, and 23 mm for slender columns G28-85-C00, G28-85-E30, G28-85-60, and G28-85-E120, respectively.

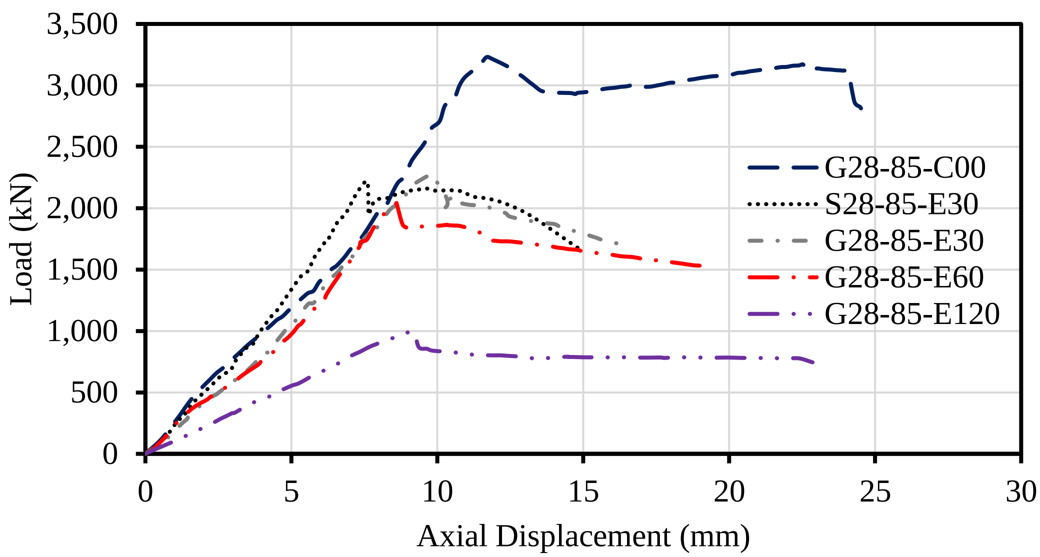

Fig. 5.5: Axial displacement responses for slender columns under concentric and eccentric loads.

The lateral displacement behaviour was similar to the axial displacement response for slender columns under eccentric loads as shown in Fig. 5.6. Under the same *e/D* ratio of 0.085, column G28-85-E30 showed 67% higher lateral displacement than the steel-RC counterpart S28-85-E30 at the peak load. Again, this was expected because of the lower stiffness of GFRP bars compared to steel. As the eccentricity increased, the GFRP-RC columns experienced higher mid-height lateral deflection at the peak load due to more primary and secondary moments acting on the column. At the peak load, increasing the eccentricity from 30 mm (G28-85-E30) to 60 mm (G28-85-E60) and further to 120 mm (G28-85-E120) resulted in 20 and 160% increase in lateral displacement, respectively. In the post-peak stage, lateral displacement kept increasing gradually until failure. At failure, the maximum lateral displacements were 36, 60 and 64 mm for slender columns G28-85-E30, G28-85-E60, and G28-85-E120, respectively.

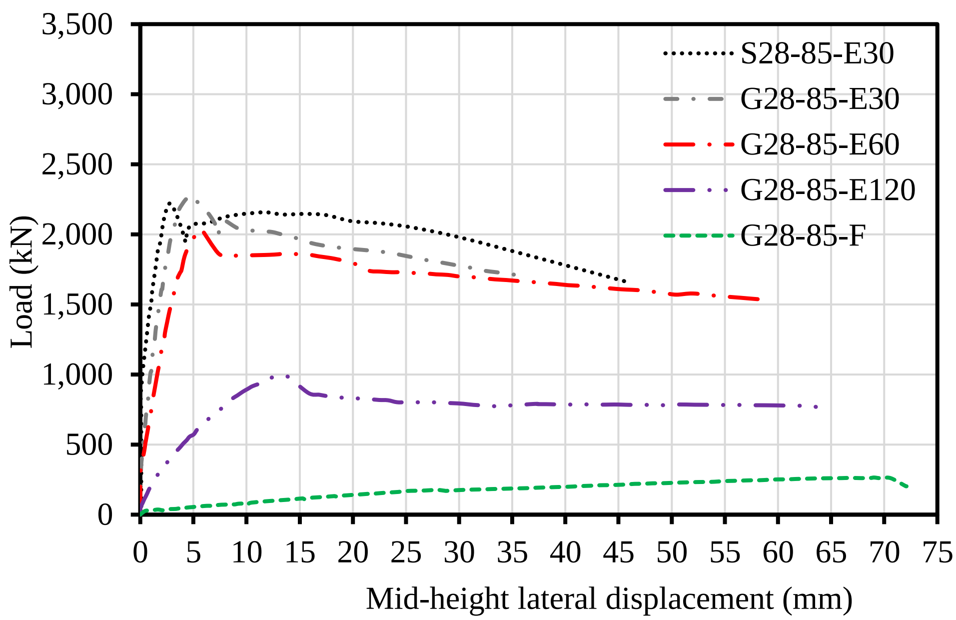

Fig. 5.6: Mid-height lateral displacement responses for slender columns under eccentric and four-point bending loads.

For column G28-85-F, the load-lateral displacement relationship was also bi-linear, as shown in Fig. 5.6. The first line represents the stiffness of the uncracked specimen, while the second line with less slope started when the first flexural-tension crack developed within the mid-span region. The maximum mid-length lateral displacement was 28 mm at the peak load and 72 mm at failure.

5.4 STRAIN PROFILES OF LONGITUDINAL STEEL AND GFRP BARS

Axial strains, shown in Fig. 5.7, were measured at mid-length of the outermost longitudinal GFRP and steel bars, where maximum compressive and tensile stresses were expected. At early loading stages, strains in the outermost longitudinal bars started to increase slowly. After development of micro-cracks and flexural-tension cracks on compression and tension sides, the bar strains increased gradually up to the peak load. For the concentrically-loaded slender column G28-85-C00, the cross-section was fully under compressive stresses up to failure. At the peak load, compressive strains of -2,850 and -2,500 micro-strains were recorded in the outermost longitudinal GFRP bars. Significant concrete cover spalling and concrete core dilation at the post-peak stage activated the confining pressure of the GFRP spiral leading to buckling and crushing of GFRP bars and rupture of spiral around mid-height of the column. The maximum recorded compressive strains, before gauge damage, were -16,900 and -13,550 micro-strains.

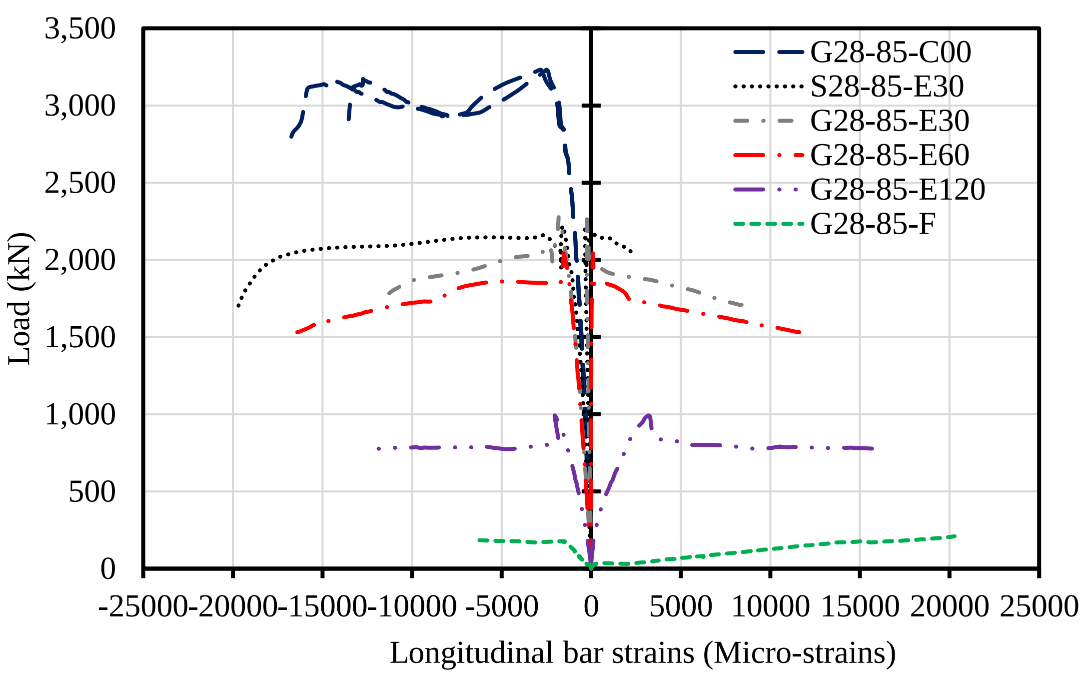

Fig. 5.7: Strain profiles of outermost longitudinal steel and GFRP bars (Series II).

Similarly, slender columns S28-85-E30 and G28-85-E30, with *e/D* = 0.085, were also under compression up to the peak load. At peak load, the measured strains in the outermost longitudinal steel and GFRP bars on compression side were -1,590 and -1,820 micro-strains for S28-85-E30 and G28-85-E30, respectively. These values were -340 and -245 micro-strains in the outermost bars on tension side, respectively. When columns reached their maximum capacity, spalling of the concrete cover reduced the stiffness causing more bending stresses on both tension and compression sides. As a result, strains in the outermost longitudinal bars on tension side changed from compression to tension and then progressively increased. At the post-peak stage for columns S28-85-E30 and G28-85-E30, most of the concrete cover was lost and the confinement of concrete core was activated. At failure, maximum compressive and tensile strains recorded for the outermost GFRP longitudinal bars were -11,460 and 8,400 micro-strains, respectively, for the column G28-85-E30. However, for steel-RC column S28-85-E30, the maximum measured strains in the outermost compression and tension longitudinal bars were -19,800 and 2,220 micro-strains, respectively with a yielding plateau.

When tested under moderate eccentricity (*e/D* = 0.17), most of the cross-section area of slender column G28-85-E60 was under compressive stresses, only a small area was experiencing tensile stresses. At the peak load, strains obtained in the outermost compression and tension longitudinal GFRP bars were −1,530 and 105 micro-strains, respectively. These values increased to −16,400 and 11,620 micro-strains, respectively, at failure. On the other hand, nearly half of the section of column G28-85-E120 tested with higher eccentricity (*e/D* = 0.34) was in compression and the rest in tension. At maximum capacity, the recorded strains in the outermost longitudinal GFRP bars on the compression and tension sides were −2,040 and 3,200 micro-strains, respectively. At failure, these values reached −12,060 and 16,090 micro-strains, respectively, with substantial concrete cover spalling and excessive lateral deformation.

For slender column G28-85-F tested under four-point bending loads, strains in the outermost longitudinal GFRP bars increased substantially after the development of flexural cracks in the tension zone. At the first peak, recorded strains were -1,610 and 15,120 micro-strains in the outermost GFRP longitudinal bars on compression and tension sides, respectively. After the first peak, the capacity of the column slightly reduced due to the concrete cover spalling in the compression zone between the two loading points. Then the specimen was able to carry increased load along with excessive deformation and widening of flexural-tension cracks. In the meantime, strains in GFRP longitudinal bars and spirals were increasing until the second peak was reached. At the second peak, the outermost GFRP longitudinal bar on the tension side ruptured and the capacity of the section dropped suddenly. The highest recorded strains at failure in the outermost longitudinal bars on compression and tension sides were −6,660 and 20,280 micro-strains, respectively.

5.5 STRAIN PROFILES OF STEEL AND GFRP SPIRALS

Spiral strains as shown in Fig. 5.8 and 5.9 were recorded at two opposite sides of a turn located at the mid-height of columns, where maximum bending stresses were expected. Strain profiles of spirals were affected by loading types and varying eccentricity-to-column diameter ratios (0, 0.085, 0.17 and 0.34). Initial slopes of strain profiles for all columns were almost similar and the strains measured were minimal at the early loading stage. However, activation of spiral confinement primarily depended on the volume and dilation of the concrete compression block. Strains in the GFRP spiral of the Concentrically-loaded slender column G28-85-C00 increased slowly at the initial loading stage. At the peak, maximum tensile strains in the GFRP spiral were recorded 1,530 and 1,220 micro-strains at two opposite sides which are only 13 and 11% of its ultimate tensile strain. After a considerable amount of cover spalling in the post-peak stage, dilation of core concrete followed by micro-crack propagation activated the confining pressure of the GFRP spirals and strains kept increasing at a faster rate till rupture. At failure, maximum tensile strains in the GFRP spiral were recorded 9,670 and 9,440 micro-strains at two opposite sides which are about 85 and 83% of the ultimate rupture strain.

Slender column sections S28-85-E30 and G28-85-E30 tested with small eccentricity (e/D = 0.085), experienced non-uniform compressive stresses up to the peak load. At maximum capacity, spiral strains were recorded 200 and 870 micro-strains for column S28-85-E30 and G28-85-E30, respectively. After a significant amount of cover spalling, the GFRP spiral began to confine the concrete core. Therefore, strain gauges recorded a significant increase in spiral strains at post-peak stages. Maximum spiral strains at failure on compression sides were recorded 2,055 and 5,545 micro-strains for columns S28-85-E30 and G28-85-E30, respectively. The GFRP-RC column showed a 3% higher capacity than the steel-RC column under small eccentric (e/D = 0.085) loads, while both having the same 85 mm spiral pitch. For column G28-85-E60 and G28-85-E120 tested under moderate and high eccentricity (e/D = 0.17 and 0.34), strains in GFRP spirals on compression sides were measured 840 and 480 micro-strains at peak, and 7,880 and 3,440 micro-strains at failure, respectively. The confinement provided by the GFRP spiral was able to prevent buckling of longitudinal bars up to failure for columns tested under eccentric (e/D = 0.085, 0.017 and 0.34) loads. GFRP spirals were able to effectively confine the core concrete at the peak and post-peak stages without rupture for eccentrically-loaded slender columns G28-85-E30, G28-85-E60 and G28-85-E120. For column G28-85-F, tested under four-point bending loads, the maximum measured strain in the GFRP spiral on the compression side was 390 micro-strains at the first peak load (192 kN). However, this value was 1,290 micro-strains at failure (286 kN), which indicates the effectiveness of the GFRP spiral in significantly enhancing the load carrying capacity without rupture.

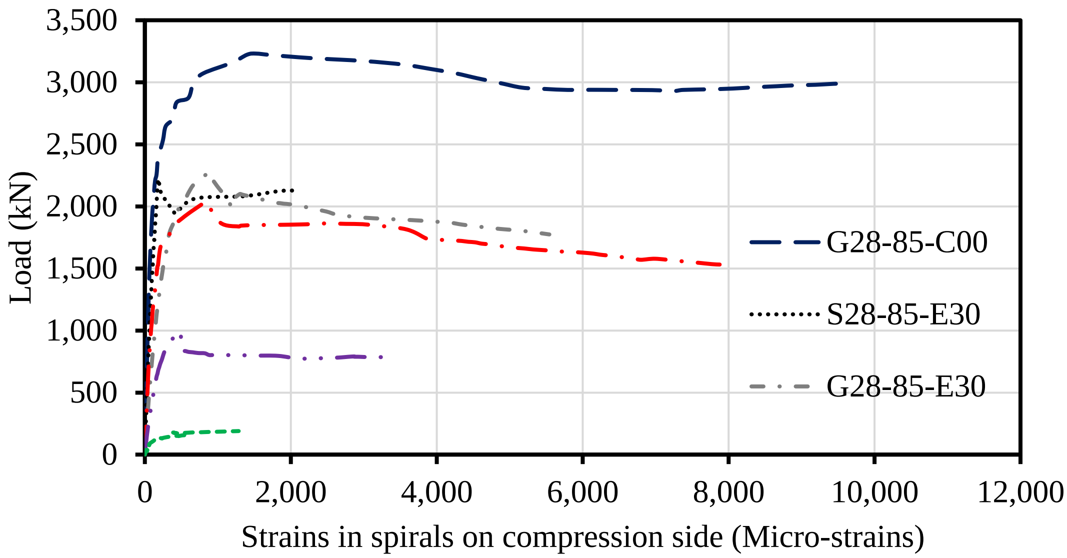

Fig. 5.8: Strain profiles of spirals on compression sides at the mid-height (Series II).

Strain profiles of spirals on tension sides were also affected by the applied loading types. Spiral confinement significantly activated after the propagation of microcracks and flexural-tension cracks. At the peak, spiral strains on tension sides were recorded minimal for columns tested under small, moderate and high eccentricity (*e/D* = 0.085, 0.17 and 0.34), and the spiral confinement was not yet activated. After the peak, microcracks and flexural-tension cracks quickly propagated on tension sides. As a result, strains in the outermost longitudinal bars increased. Similarly, strains in spirals increased as a result of providing lateral support to the concrete core. The maximum strains at failure were recorded 370, 940, 4,360 and 2,575 micro-strains for slender columns S28-85-E30, G28-85-E30, G28-85-E60 and G28-85-E120, respectively. Strains in the outermost longitudinal GFRP bar of the column G28-85-F increased significantly after the first peak. The spiral reacted to provide lateral supports for the GFRP longitudinal bars and strains in the GFRP spiral increased significantly. The measured spiral strains for the column G28-85-F were recorded 1,210 and 5,040 micro-strains at the peak and failure, respectively.

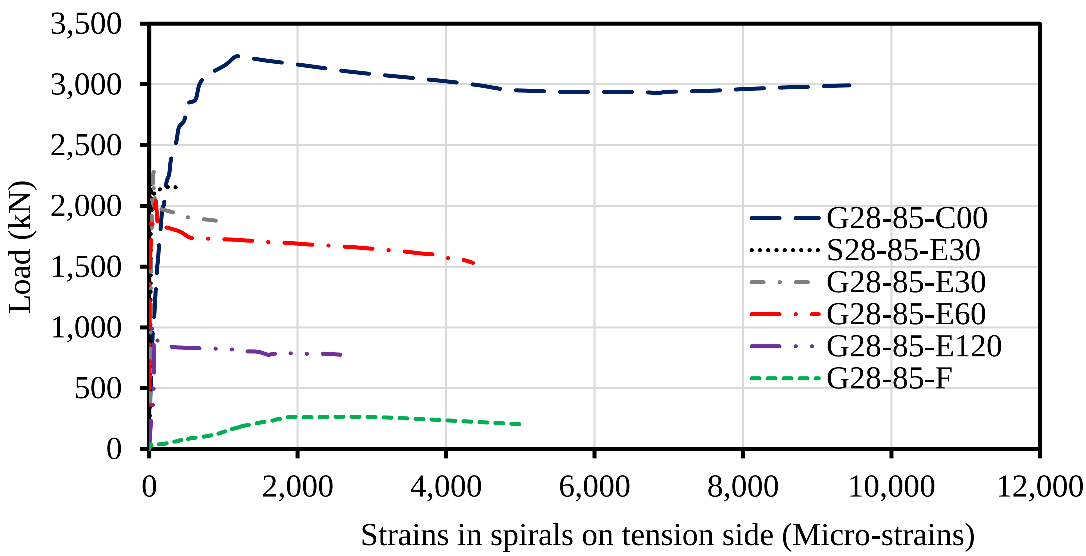

Fig. 5.9: Strain profiles of spirals on tension sides at the mid-height (Series II).

5.6 CONCRETE COMPRESSIVE STRAIN RESPONSES

At early loading stages, the load-concrete strain relationship was approximately linear, as shown in Fig. 5.10. With the increasing load, micro-cracks and/or flexural-tension cracks developed and the concrete strain graphs started to diverge for columns subjected to different loading types and eccentricities. After that, concrete strains increased non-linearly until it reached the crushing strain and columns reached their maximum capacity. The maximum concrete compressive strain recorded at the peak load was -3,430, -3,410, -3,480, -3,340, -3,365, and -3,565 micro-strains for slender columns G28-85-C00, S28-85-E30, G28-85-E30, G28-85-E60, G28-85-E120 and G28-85-F, respectively, which are close to the specified design limit of -3,500 micro-strains (CSA 2017).

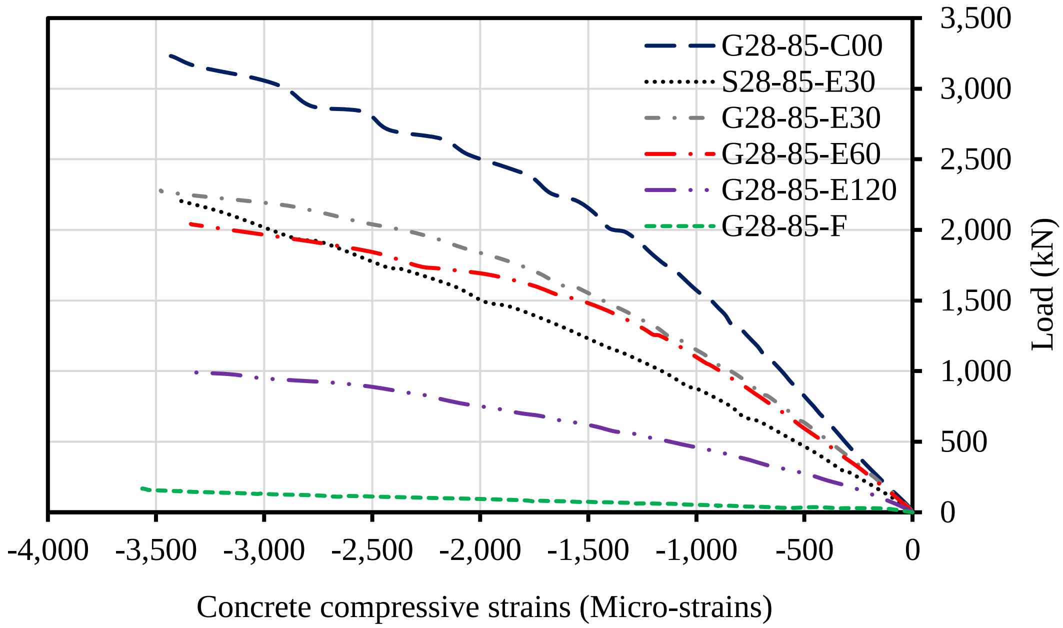

Fig. 5.10: Concrete compressive strain responses at the mid-height (Series II).

5.7 NORMALIZED INTERACTION DIAGRAM FOR SLENDER COLUMN

Fig. 5.11 shows the normalized interaction diagram along with the load path for the GFRP-RC slender (kl_u/r = 28) circular columns tested under concentric, eccentric and four-point bending loads. The difference between the two lines is the point obtained form the pure flexure test. The dotted line represents the first peak moment for the test specimen while the solid line represents the second peak moment for the specimen. It is to be mentioned that the same behavior (the two peaks) was reported by Mousa et al. (2018) for flexural behavior of circular members.

The normalized axial force (K_n) and the normalized bending moment (R_n) are given by:

$$K_n = \frac{P_n}{A_g f'_c} \quad \text{Eq. 5.1}$$

$$R_n = \frac{M_n}{A_g f'_c D} \quad \text{Eq. 5.2}$$

$$M_n = M_{n_1} + M_{n_2} = (P_n \times e) + (P_n \times \delta_n) \quad \text{Eq. 5.3}$$

The value of P_n is defined as the ultimate nominal peak load and δ_n is the measured lateral mid-height displacement at the peak. The nominal primary moments M_{n_1} are based on the initial applied eccentricity (e), and the nominal secondary moments M_{n_2} are based on the measured lateral mid-height displacement at the peak load as mentioned in Table 5.1, *Ag* is the gross sectional area, f'_c is the average cylindrical concrete compressive strength, and *D* is the overall column diameter. Like GFRP-RC short columns, slender columns also exhibited a "*knee*" shaped interaction diagram similar to the steel-RC columns in which the moment resistance increases as the axial capacity decreases until the inflection point is reached, known as the balance point for steel-RC columns.

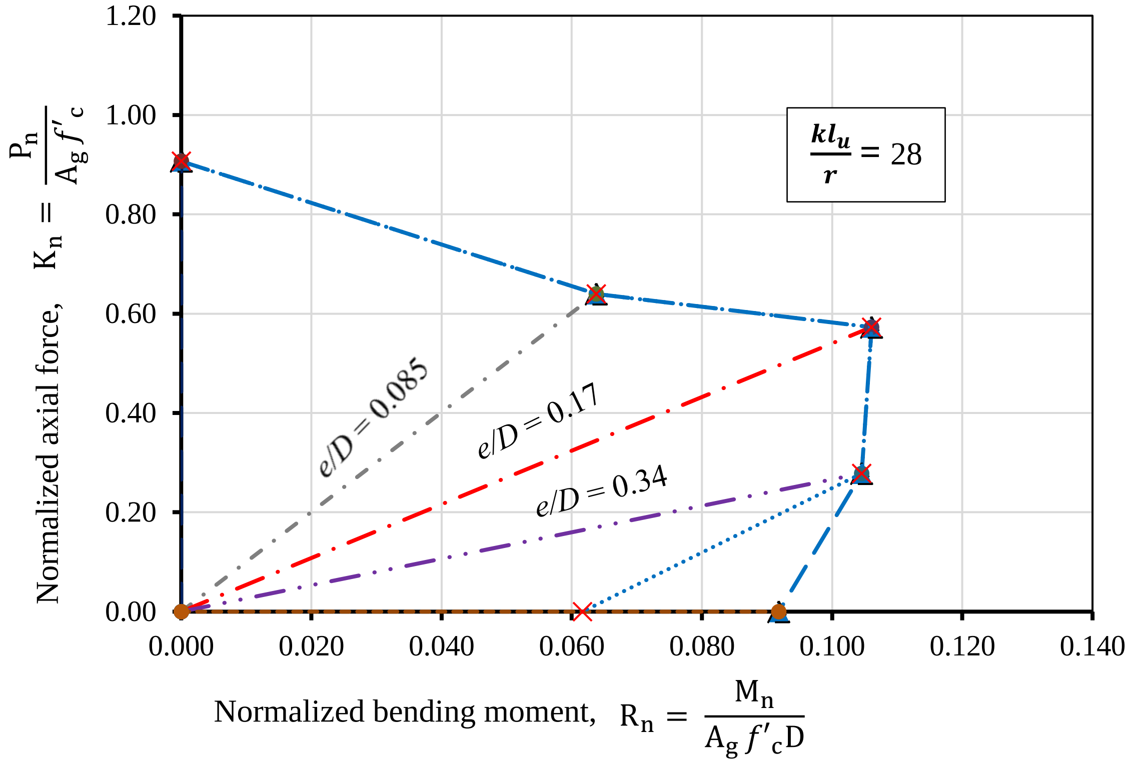

Fig. 5.11: Normalized interaction diagram for GFRP-RC circular slender column.

Results show that, for slender GFRP-RC columns as the *e/D* ratio increased from 0.085 (column G28-85-E30) to 0.17 (column G28-85-E60), the axial capacity was decreased by 11% and the moment capacity was increased by 70%. However, when the *e/D* ratio increased from 0.17 (column G28-85-E60) to 0.34 (column G28-85-E120), the axial and moment capacity was decreased by 52% and 2%, respectively. Therefore, after the inflection point, axial and flexural resistances started to decrease simultaneously. This point is known to establish the compression and tension-controlled regions for steel-RC columns. The axial capacity decreased by 30, 37 and

70% for slender columns G28-85-E30, G28-85-E60, and G28-85-E120, respectively compared to column G28-85-C00 as the *e/D* ratio increased from 0 to, 0.085 and further to 0.34.

As an effect of slenderness, circular GFRP-RC slender columns showed lower axial capacity than the shorter ones similar to the steel-RC columns (Fig. 4.11 and 5.11). This happened because slender columns experienced higher mid-length lateral deformation than shorter ones which eventually induced more secondary moments. Results show that, circular GFRP-RC slender columns G28-85-C00, G28-85-E30, G28-85-E60 and G28-85-120 showed a peak load of 25, 22, 21 and 23% less than the shorter columns G20-85-C00, G20-85-E30, G20-85-E60 and G20-85-E120, respectively. The pure flexure point obtained from second peak load was recorded approximately 49% higher than that of the first peak load. The solid line is in good agreement with the findings of the previous research studies (Mirmiran et al., 2001; Karim et al. 2017).

Table 5.1: Experimental test results for slender columns (Series II)

Specimen ID	e (mm)	P_n (kN)	P_n (36/f'_c) (kN)	δ_n (mm)	Δ_n (mm)	M_{n1} (kN.m)	M_{n2} (kN.m)	M_n (kN.m)
						$P_n \times e$	$P_n \times \Delta_n$	$M_{n1} + M_{n2}$
G28-85-C00	0	2,917	3,231	-	12	0	0	0
S28-85-E30	30	2,178	2,221	3	8	67	6	73
G28-85-E30	30	2,387	2,279	5	10	68	11	79
G28-85-E60	60	1,758	2,042	6	9	122.5	11.5	134
G28-85E120	120	1,069	992	13	9	119	13	132
G28-85-F	-	211[a] (314[b])	192[a] (286[b])	28	-	-	-	84[c](125[c])

[a] First peak load
[b] Second peak load
[c] $M_n = (P_n/2) \times$ Shear span

CHAPTER 6 – SUMMARY, CONCLUSIONS AND FUTURE WORK

6.1 SUMMARY

This section presents the findings from the current investigation and the recommendations for future work. The current study investigated the performance of circular-shaped concrete columns reinforced with GFRP bars and spirals. The experimental scheme included two different series, namely, Series I and Series II. Series I include seven full-scale GFRP-RC circular short columns, and Series II include six full-scale GFRP-RC circular slender columns. Columns were tested under concentric, eccentric, and four-point bending loads conditions.

A total of thirteen GFRP-RC circular columns were constructed and tested to failure in the experimental phase. The test variables in Series I were the reinforcement type (GFRP and steel), the GFRP spiral pitch (50 and 85 mm), and varying ratios of eccentricity-to-column diameter (*e/D* = 0, 0.085, 0.17 and 0.34). In Series II, test variables were the reinforcement type (GFRP and steel), and varying ratios of eccentricity-to-column diameter (*e/D* = 0, 0.085, 0.17 and 0.34). Also, two different slenderness ratios (*klu/r* = 20 and 28) were used for two separate series (Series I and Series II) to evaluate the effect of varying slenderness ratios on the normalized axial load-moment interaction diagram for GFRP-RC circular columns. After the analysis, some conclusions regarding both series are made and given in the following sections.

6.2 CONCLUSIONS FROM SERIES I

Based on the experimental results of Series I, the following conclusions can be drawn:

- The obtained capacity of GFRP-RC short column tested with small eccentricity was less than the counterpart steel-RC column. However, reducing the GFRP spiral pitch resulted in a similar capacity to the steel-RC columns. The peak load of the GFRP-RC column with 85-mm spiral pitch was 17% less than that of the steel-RC counterpart; both tested under the same eccentricity (*e/D* = 0.085) and having the same pitch. However, this peak load increased by 10% when the GFRP spiral pitch decreased to 50 mm.

- The GFRP-RC column experienced higher axial and lateral deformation than the steel-RC control specimen. This was due to the lower elastic modulus of GFRP bars compared to steel. However, reducing the GFRP spiral pitch resulted in less axial and lateral deformation. The GFRP-RC column experienced 6 and 67% higher axial and mid-height lateral displacements than the steel-RC counterpart at the peak load. However, the column with 50-mm pitch exhibited 3 and 5% lower axial and mid-height lateral displacements than column with 85-mm pitch at the peak.
- The mode of failure of GFRP-RC columns under concentric and small eccentric (*e/D* = 0.085) axial loads was brittle compression failure due to concrete cover spalling at the peak around mid-height followed by concrete core crushing, bar buckling, sudden rupture of GFRP spiral and crushing of GFRP bars at the post-peak stage. The steel-RC column failed by concrete cover spalling at the peak followed by gradual yielding of the outermost steel bars and spirals along with concrete core crushing. However, at the post-peak stage, the linear elastic behaviour of GFRP bars and spirals up to the failure caused sudden and brittle failure of the GFRP-RC columns, whereas, the yielding plateau of steel reinforcements caused the gradual failure of the steel-RC column.
- Under moderate and large eccentricity (*e/D* = 0.17 and 0.34), GFRP-RC columns failed by concrete crushing and concrete cover spalling around mid-height on the compression side followed by large deformation and gradual degradation of the concrete compression block. The failure mode of GFRP-RC columns under four-point bending loads was compression

failure due to concrete cover spalling in the mid-span region at the peak followed by excessive deformation and gradual rupture of the outermost GFRP bar on the tension side.

- Size No. 10 GFRP spirals with 85-mm pitch, corresponding to 1.11% volumetric ratio in concentric and low eccentric (*e/D* = 0.085) circular GFRP-RC columns, were able to fulfill their function as transverse reinforcement by providing lateral support to the compression and tension bars and by confining the compressive concrete core up to the peak load but was not sufficient at the post-peak stage to provide enough warning before sudden and brittle failure. However, in case of columns under moderate and large eccentricity (*e/D* = 0.17 and 0.34) and under four-point bending loads, the same amount of transverse reinforcements was able to effectively confine the concrete core and enhance the overall performance of the specimens without any rupture of GFRP spiral at the peak or post-peak stages.

- Results showed that GFRP longitudinal bars were able to sustain high strains. The maximum strains measured in GFRP longitudinal bars were approximately 80% of the ultimate. However, GFRP bars in columns under small and moderate eccentricity (*e/D* = 0.085 and 0.17) experienced a higher amount of compressive strains compared to columns under high eccentric (*e/D* = 0.34) and four-point bending loads. On the other hand, GFRP bars within columns under high eccentricity and four-point bending loads experienced higher tensile strains.

- A “knee” shaped axial load-bending moment interaction diagram for circular GFRP-RC short column was developed from experimental results in which axial capacity decreases and flexural capacity increases until the inflection point is reached, then both axial and flexural capacity decreases simultaneously. As the *e/D* ratio increases from 0 to 0.17 and further to 0.34 the axial capacity reduced by 32, 39 and 70% from the capacity of the concentric column.

6.3 CONCLUSIONS FROM SERIES II

Based on the experimental results of Series II, the following conclusions can be drawn:

- The GFRP-RC slender circular column exhibited similar capacity to that of the steel-RC control specimen. The GFRP-RC slender column carried 3% higher load than that of the steel-RC counterpart, while both tested under the same eccentricity (e/D = 0.085) and having the same 85-mm spiral pitch.
- The GFRP-RC column experienced 25 and 67% higher axial and mid-height lateral displacements than the steel-RC counterpart at the peak load. This was expected due to the lower elastic modulus of GFRP bars compared to steel. As the eccentricity increased, the GFRP-RC slender circular columns experienced higher mid-height lateral deflection than the respective short columns due to more secondary moments acting on the column. The slender columns showed 25, 13, and 41% higher mid-height lateral displacements than the short column counterparts.
- The mode of failure of GFRP-RC slender column under concentric loads was brittle compression failure due to concrete cover spalling at the peak followed by concrete core crushing, bar buckling, sudden rupture of GFRP spiral and crushing of GFRP bars at the post-peak stage. The failure mode of GFRP-RC slender column under small eccentricity (e/D = 0.085) was compression failure due to concrete cover spalling around mid-height at the peak followed by gradual concrete core crushing. The steel-RC column tested under the same eccentricity failed by concrete cover spalling at the peak followed by gradual yielding of the outermost steel bars and spirals along with concrete core crushing.

- Under moderate and large eccentricity (*e/D* = 0.17 and 0.34), GFRP-RC slender circular columns failed by concrete crushing and cover spalling around mid-height on the compression side followed by large deformation and gradual degradation of the concrete compression block. The failure mode of GFRP-RC slender column under four-point bending loads was compression failure due to concrete cover spalling in the mid-span region at the peak followed by excessive deformation and gradual rupture of the outermost GFRP bar on the tension side.

- No. 10 GFRP spirals with 85-mm pitch, corresponding to 1.11% volumetric ratio in concentric circular GFRP-RC slender column, were able to fulfill their function as transverse reinforcement by providing lateral support to the bars and by confining the compressive concrete core up to the peak load but was not sufficient after peak to provide enough warning before sudden and brittle failure. However, in case of columns under low to large eccentricity (*e/D* = 0.085, 0.17, and 0.34) and under four-point bending loads, the same amount of transverse reinforcements was able to effectively confine the concrete core and enhance the overall performance of the specimens without any rupture of GFRP spiral at the peak or post-peak stages.

- A “knee” shaped axial load-bending moment interaction diagram for circular GFRP-RC slender column was developed from experimental results in which axial capacity decreases and flexural capacity increases until the inflection point is reached, then both axial and flexural capacity decreases simultaneously. As the *e/D* ratio increases from 0 to 0.17 and further to 0.34 the axial capacity reduced by 30, 37 and 70% from the capacity of the concentric column.

- As an effect of slenderness, circular GFRP-RC slender columns showed lower axial capacity than the shorter ones similar to steel-RC columns. This occurred because slender columns experienced higher mid-length lateral deformation than shorter ones, which eventually induced more secondary moments. Results indicated that, circular GFRP-RC slender columns showed 25, 22, 21 and 23% less axial capacity than their short column counterparts.

6.4 FUTURE WORK

The following are suggestions for further studies on behaviour of GFRP-RC columns subjected to concentric, eccentric and four-point bending loads:

1. Study the behaviour of GFRP reinforced high strength concrete short and slender columns under axial and flexural loads.
2. Study the behaviour of CFRP and BFRP reinforced normal and high strength concrete short and slender columns under axial and flexural loads.
3. Establish normalized interaction diagram for GFRP and CFRP-RC rectangular and square shaped short and slender columns.
4. Develop a confinement model for FRP-RC circular columns subjected to axial and flexural loads.
5. Analytical and experimental study of slenderness effects on the performance of FRP-RC column.
6. Conduct section analysis and validate the interaction diagrams developed in this study.

REFERENCES

ACI Committee 318 (1995). “Building Code Requirements for Structural Concrete and Commentary”, American Concrete Institute, Farmington Hills, MI.

ACI Committee 318 (2005). “Building Code Requirements for Structural Concrete (ACI 318-05) and Commentary (318R-05)”, American Concrete Institute, Farmington Hills, MI.

ACI Committee 318 (2019). “Building Code Requirements for Structural Concrete and Commentary”, American Concrete Institute, Farmington Hill, MI.

ACI Committee 440 (2015). “Guide for the Design and Construction of Structural Concrete Reinforced with FRP Bars (ACI440.1R-15)”, American Concrete Institute, Farmington Hills, MI.

ASTM (2015). “Standard Test Method for Compressive Properties of Rigid Plastics (D695)”, West Conshohocken, Pennsylvania, United States.

ASTM (2016). “Standard Test Method for Compressive Properties of Polymer Matrix Composite Materials with Unsupported Gage Section by Shear Loading (D3410/D3410M)”, West Conshohocken, Pennsylvania, United States.

Afifi, M. Z., Mohamed, H. M., and Benmokrane, B. (2014). “Axial Capacity of Circular Concrete Columns Reinforced with GFRP Bars and Spirals”, Journal of Composites for Construction, ASCE, 18(1): 1-11.

Alsayed, S. H., Al-Salloum, Y. A., Almusallam, T. H. and Amjad, M. A. (1999). “Concrete Columns Reinforced by Glass Fiber Reinforced Polymer Rods”, ACI Structural Journal, Special Publication, 188:103-112.

Alves, J., El-Ragaby, A., and El-Salakawy, E. (2010). “Durability of GFRP Bars’ Bond to Concrete under Different Loading and Environmental Conditions”, Journal of Composites for Construction, ASCE, 15(3): 249-262.

Benmokrane, B., El-Salakawy, E., El-Ragaby, A. and El-Gamal, S. (2007). “Performance Evaluation of Innovative Concrete Bridge Deck Slabs Reinforced with Fiber-Reinforced Polymer Bars”, Canadian Journal of Civil Engineering, 34(3): 298–310.

Brown, J. (2015). “Glass Fibre Reinforced Polymer Bars in Concrete Compression Members”, International Conference on Performance-based and Life-cycle Structural Engineering, School of Civil Engineering, The University of Queensland, 1590-1599.

Canadian Standards Association (CSA). (2017). “Design and construction of building structures with fiber-reinforced polymers”, CSA/S806-12 (R2017), Canadian Standards Association, Toronto, Ontario, Canada.

Canadian Standards Association (CSA). (2014a). “Design of concrete structures”, CSA/A23.1-14, Canadian Standards Association, Toronto, Ontario, Canada.

Canadian Standards Association (CSA). (2014b). “Design of concrete structures”, CSA/A23.3-14, Canadian Standards Association, Toronto, Ontario, Canada.

Canadian Standards Association (CSA). (2019a) “Canadian highway bridge design code”, CSA/S6-19, Canadian Standards Association, Toronto, Ontario, Canada.

Canadian Standards Association (CSA). (2019b) “Canadian specification for fibre-reinforced polymers”, CSA/S807-19, Canadian Standards Association, Toronto, Ontario, Canada.

Carreira, D. J., and Chu, K. (1985). “Stress-Strain Relationship for Plain Concrete in Compression”, ACI Journal, 82 (6): 797-804.

Choo, C. C., Harik, I. E., and Gesund, H. (2006). “Strength of Rectangular Concrete Columns Reinforced with Fiber-Reinforced Polymer Bars”, ACI Structural Journal, 103(3): 452-459.

Deitz, D. H., Harik, I. E., and Gesund, H. (2003). “Physical Properties of Glass Fiber Reinforced Polymer Rebars in Compression”, Journal of Composites for Construction, ASCE, 7(4): 363–366.

De Luca, A., Matta, F., and Nanni, A. (2010). “Behavior of Full-Scale Glass Fiber-Reinforced Polymer Reinforced Concrete Columns under Axial Load”, ACI Structural Journal, 107(5): 589-596.

El-Gendy, M. G. and El-Salakawy, E. F. (2018). “Lateral Displacement Deformability of GFRP-RC Slab-Column Edge Connections”, ACI Structural Journal, Special Publication, 327: 52.1-52.20.

El-Nemr, A., Ahmed, E. A., and Benmokrane, B. (2013). “Flexural behavior and serviceability of normal- and high-strength concrete beams reinforced with glass fiber-reinforced polymer bars”, ACI Structural Journal, 110 (6):1077-1088.

El-Salakawy, E., Benmokrane, B. and Desgagné, G. (2003). “FRP composite bars for the concrete deck slab of Wotton Bridge”, Canadian Journal of Civil Engineering, 30(5): 861–870.

Ghomi, S.K. and El-Salakawy, E.F. (2016). “Seismic Performance of GFRP-RC Exterior Beam-Column Joints with Lateral Beams”, Journal of Composites for Construction, ASCE, 20(1), 04015019: 1-11.

Hadhood, A., Mohamed, H. M. and Benmokrane, B. (2017a). “Experimental Study of Circular High-Strength Concrete Columns Reinforced with GFRP Bars and Spirals under Concentric and Eccentric Loading”, Journal of Composite Construction, ASCE, 21(2): 1-12.

Hadhood, A., Mohamed, H. M. and Benmokrane, B. (2017b). “Failure Envelope of Circular Concrete Columns Reinforced with GFRP Bars and Spirals”, ACI Structural Journal, 114(6): 1417-1428.

Hadi, M. N. S., Hasan, H. A., and Sheikh, M. N. (2017). “Experimental Investigation of Circular High-Strength Concrete Columns Reinforced with Glass Fiber-Reinforced Polymer Bars and Helices under Different Loading Conditions”, Journal of Composites for Construction, ASCE, 21(4): 4017005.

Issa, M. S., Metwally, I. M., and Elzeiny, S. M. (2011). “Structural Performance of Eccentrically Loaded GFRP Reinforced Concrete Columns”, International Journal of Civil and Structural Engineering, *2* (1): 395-406.

Karim, H., Sheikh, M. N., and Hadi, M. N. (2017). “Axial Load-Axial Deformation Behaviour of Circular Concrete Columns Reinforced with GFRP Bars and Helices”, Construction and Building Materials, 112, 1147-1157.

Kassem, C., Farghaly, A. S., and Benmokrane, B. (2011). “Evaluation of flexural behaviour and serviceability performance of concrete beams reinforced with FRP bars”, Journal of Composites for Construction, ASCE, 15(5): 682-695.

Lotfy, E. M. (2010). “Behavior of Reinforced Concrete Short Columns with Fiber Reinforced Polymers Bars”, International Journal of Civil and Structural Engineering, 1(3): 545-557.

Macgregor, J.G., and Wight, J.K. (2012). "Reinforced Concrete: Mechanics and Design", Prentice Hall, 1177.

Mahmoud, K., and El-Salakawy, E. (2016). "Size Effect on Shear Strength of GFRP-RC Continuous Beams without Shear Reinforcement", ACI Structural Journal, 113 (1): 125-134.

Maranan, G. B., Manalo, A. C., Benmokrane, B., Karunasena, W., and Mendis, P. (2016) "Behavior of Concentrically Loaded Geopolymer-Concrete Circular Columns Reinforced Longitudinally and Transversely with GFRP Bars", Engineering Structures, 117(15): 422-436.

Mirmiran, A., Yuan, W., and Chen, X. (2001). "Design for Slenderness in Concrete Columns Internally Reinforced with Fiber-Reinforced Polymer Bars", ACI Structural Journal, 98, (1): 116-125.

Mohamed, H., Afifi, M., and Benmokrane, B. (2014). "Performance Evaluation of Concrete Columns Reinforced Longitudinally with FRP Bars and Confined with FRP Hoops and Spirals under Axial Load", Journal of Bridge Engineering, ASCE, 19(7): 04014020.

Mosley, C. P., Tureyen, A. K., and Frosch, R. J. (2008). "Bond Strength of Nonmetallic Reinforcing Bars", ACI Structural Journal, 105(5): 634–642.

Mousa, S., Mohamed, H. M., and Benmokrane, B. (2018). "Flexural Strength and Design Analysis of Circular Reinforced Concrete Members with Glass Fiber-Reinforced Polymer Bars and Spirals", ACI Structural Journal, 115(5): 1353-1364.

Nanni, A. (1993). "Flexural behaviour and design of RC members using FRP reinforcement", Journal of Structural Engineering, ASCE 119(11): 3344-3359.

Naqvi, S., and El-Salakawy, E. (2016). “Lap Splice in GFRP-RC Rectangular Columns Subjected to Cyclic-Reversed Loads”, Journal of Composites for Construction, ASCE, 21(4): 1–13.

National Association of Corrosion Engineers (NACE) International. “Corrosion costs and preventive strategies in the United States”, Pub. No. FHWA-RD-01-156, <http://www.nace.org> (Jul. 15, 2013).

Pantelides, C. P., Gibbons, M. E., and Reaveley, L. D. (2013). “Axial Load Behavior of Concrete Columns Confined with GFRP Spirals”, Journal of Composites for Construction, ASCE, 17 (3): 305-313.

Park, R., and Paulay, T. (1975). “Reinforced Concrete Structures”, John Wiley and Sons, New York, 769.

Phillips, L.N. (1989). “Design with Advanced Composite Materials”, Springer- Verlag.

Prachasaree, W., Piriyakootorn, S., Sangsrijun, A., and Limkatanyu, S. (2015). “Behavior and Performance of GFRP Reinforced Concrete Columns with Various Types of Stirrups”, International Journal of Polymer Science, 1-9.

Pultrall Inc. (2019). Private Communications, ADS Comp. Group. Thetford Mines, QC, Canada.

Rizkalla, S., Hassan, T. and Hassan, N. (2003). “Design Recommendations for the use of FRP for Reinforcement and Strengthening of Concrete Structures”, Journal of Progress in Structural Engineering and Materials, 5(1): 16-28.

Saatcioglu, M., and Razvi, S. R. (2002). “Displacement based design of reinforced concrete columns for confinement”, ACI Structural Journal, 90(1): 3–11.

Tavassoli, A., Liu, J., and Sheikh, S. (2015). “Glass Fiber-Reinforced Polymer-Reinforced Circular Columns under Simulated Seismic Loads”, ACI Structural Journal, 110(6): 941–951.

Theriault, M., and Benmokrane, B. (1998). “Effects of FRP reinforcement ratio and concrete strength on flexure behavior of concrete beams”, Journal of Composites for Construction, ASCE, 2(1): 7-16.

Tikka, T. K., Francis, M., and Teng, B. (2010). “Strength of Concrete Beam Columns Reinforced with GFRP Bars”, 2nd International Structures Specialty Conference, Winnipeg, MB, Canada, pp. 1194-1203.

Tobbi, H., Farghaly, A. S., and Benmokrane, B. (2012). “Concrete Columns Reinforced Longitudinally and Transversally with Glass Fiber-Reinforced Polymer Bars”, ACI Structural Journal, 109 (4): 551-558.

Tobbi, H., Farghaly, A. S., and Benmokrane, B. (2014). “Strength Model for Concrete Columns Reinforced with Fiber-Reinforced Polymer Bars and Ties”, ACI Structural Journal, 111(4): 789-798.

Xiao, Y. (2004). “Applications of FRP Composites in Concrete Columns”, Journal of Advances in Structural Engineering, 7(4): 335–343.

Xue, W., Peng, F., and Fang, Z. (2018), “Behavior and Design of Slender Rectangular Concrete Columns Longitudinally Reinforced with Fiber-Reinforced Polymer Bars”, ACI Structural Journal, 115 (2): 311-322.

Zadeh, H. and Nanni, A. (2013). “Design of RC columns using glass FRP reinforcement”, Journal of Composite Construction, ASCE, 17(3): 294–304.

APPENDIX A: DESIGN OF GFRP-RC SPECIMEN

Column dimension:

D = 355 mm; lu = 1,750 mm (Series I: Short columns); lu = 2,450 mm (Series II: Slender columns)

Cross-sectional properties:

D = 355 mm; $R = 177.5$ mm;

$A_g = \pi R^2 = 3.1416 \times 177.5^2 = 98980.035$ mm^2

Concrete properties:

f_c' = 35 MPa; ϕ_c = 1;

$E_c = 4500\sqrt{f_c'}$ = 26622 MPa;

α_1= 0.85 - 0.0015 f_c' = 0.797 [CSA 2012 (8.4.1.5)];

β_1 = 0.97 - 0.0025f_c' = 0.883 [CSA 2012 (8.4.1.5)];

ε_{cu}= 0.0035;

Longitudinal reinforcement: GFRP bars (No. 16)

f_{Fu} = 1558 MPa; ϕ_F = 1; E_F = 64 GPa; A_b = 199 mm^2; ε_{Fu} = 2.4%;

Transverse reinforcement: GFRP spiral (No. 10)

f_{Fu} = 667 MPa; ϕ_F = 1; E_F = 58 GPa; A_{sp} = 71 mm^2; ε_{Fu} = 1.14%;

Slenderness ratio:

k= 1 for pin-ended support condition

Series I (Short column): $\frac{\boldsymbol{kl_u}}{\boldsymbol{r}} = \frac{\mathbf{1\times1750}}{\mathbf{0.25\times355}}$ = 19.72 < 22 [CSA 2012 (8.4.3.3)]

Series II (Slender column): $\frac{kl_u}{r} = \frac{1\times2450}{0.25\times355}$ = 27.61 > 22 [CSA 2012 (8.4.3.3)]

Longitudinal reinforcement ratio:

According to CSA 2012 (8.4.3.10), minimum number of longitudinal reinforcing bars in circular columns shall be six and the bar size shall be not less than 15 mm in diameter.

Selecting 6-No.16 bars for all GFRP-RC specimens.

$\rho_f = \frac{A_F}{A_g} = \left[\frac{(6 \times 199)}{98980.035}\right] \times 100 = 1.20\ \% > 1\% < 8\%$ [CSA 2012 (8.4.3.8)]

Spiral pitch and transverse reinforcement ratio:

$$D_c = [\{355 - (2 \times 22.5) - 9.5\}] = 300.5\ mm$$

$$A_c = \frac{3.1416 \times 300.5^2}{4} = 70921.816\ mm^2$$

According to CSA 2012 (8.4.3.13), FRP spiral shall conform to the following:

a. Spiral reinforcement shall have a minimum diameter of 6 mm:

So, No. 10 (9.5-mm diameter) GFRP spiral selected.

b. The pitch or distance between turns of the spirals shall not exceed 1/6 of the core diameter:

So, spiral pitch = $\frac{D_c}{6} = \frac{300.5}{6} = 50.08\ mm$

c. The clear spacing between successive turns of a spiral shall not exceed 75 mm nor be less than 25 mm: Spiral pitch = $75 + 9.5 = 84.5 \approx 85\ mm$

d. The volumetric ratio of spiral reinforcement shall be not less than the value given by

$$\frac{P}{P_0} = 0.3 > 0.2$$

$$\frac{A_g}{A_c} = \frac{98980.035}{70921.816} = 1.3956 > 0.3$$

$f_{Fh} = \emptyset_F F_{Fu} = 1 \times 667 = 667\ MPa$ or

$f_{Fh} = 0.006 E_F = 0.006 \times 58 \times 10^3 = 348\ MPa\ (Least)$

$$\rho_{Fs_{Req.}} = \frac{f'_c}{f_{Fh}}\left(\frac{A_g}{A_c} - 1\right)\left(\frac{P}{P_0}\right) = \frac{35}{348}\left(\frac{98980.035}{70921.816} - 1\right)(0.3) = 0.011 \times 100 = 1.1\%$$

For spiral pitch = 50 mm,

$$\rho_{Fs_{Prov.}} = \frac{Volume\ of\ spiral}{Volume\ of\ core} = \frac{4A_{sp}}{D_c s} = \frac{4 \times 71}{300.5 \times 50} = 0.0189 \times 100 = 1.89\% > 1.1\%$$

For spiral pitch = 85 mm,

$$\rho_{Fs_{Prov.}} = \frac{Volume\ of\ spiral}{Volume\ of\ core} = \frac{4A_{sp}}{D_c s} = \frac{4 \times 71}{300.5 \times 85} = 0.0111 \times 100 = 1.11\% > 1.1\%$$

<u>Design axial capacity:</u>

According to CSA 2012, Nominal axial capacity,

$$P_0 = \alpha_1 f'_c\left(A_g - A_F\right) = [0.797 \times 35 \times (98980.035 - (6 \times 199)] \times 10^{-3} = \boldsymbol{2727.74\ kN}$$

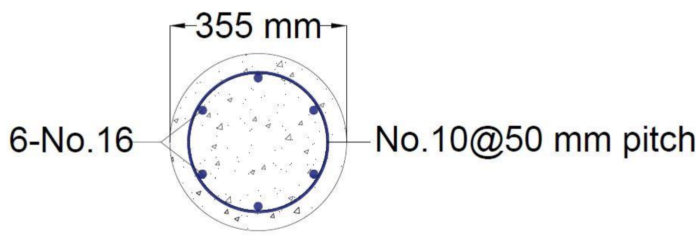

GFRP-RC

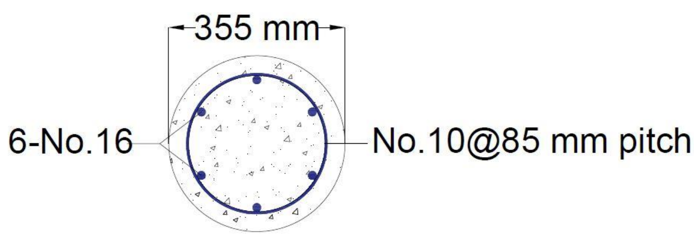

GFRP-RC

APPENDIX B: DESIGN OF STEEL-RC SPECIMEN

Column dimension:

D = 355 mm; lu = 1,750 mm (Series I: Short columns); lu = 2,450 mm (Series II: Slender columns)

Cross-sectional properties:

D = 355 mm; $R = 177.5$ mm;

$A_g = \pi R^2 = 3.1416 \times 177.5^2$ = 98980.035 mm^2

Concrete properties:

f_c' = 35 MPa; ϕ_c = 1;

$E_c = 4500\sqrt{f_c'}$ = 26622 MPa [CSA 2014 (8.6.2.3)];

α_1= 0.85 - 0.0015 f_c' = 0.797 [CSA 2014 (10.1.7)];

β_1 = 0.97 - 0.0025f_c' = 0.883 [CSA 2014 (10.1.7)];

ε_{cu}= 0.0035;

Longitudinal reinforcement: Steel bars (15M)

f_y = 400 MPa; ϕ_s = 1; E_s = 200 GPa; A_{st} = 200 mm^2; ε_y = 0.002;

Transverse reinforcement: GFRP spiral (10M)

f_y = 400 MPa; ϕ_s = 1; E_s = 200 GPa; A_{st} = 100 mm^2; ε_y = 0.002;

Slenderness ratio:

According to CSA 2014 (10.15.2), in non-sway frames slenderness effects may be ignored for compression members that satisfy the following equation:

$$\frac{kl_u}{r} \leq \frac{25 - 10\left(\frac{M1}{M2}\right)}{\sqrt{\frac{P_f}{A_g f'_c}}} = \frac{25 - (10 \times 0.5)}{\sqrt{\frac{3207.57 \times 10^3}{(98980.035 \times 35)}}} = 20.78$$

Where, $\frac{M1}{M2}$ is not taken less than -0.5. $\frac{M1}{M2}$ shall be taken as positive if the member bent in a single curvature.

k= 1 for pin-ended support condition

Nominal axial capacity [CSA 2014 (10.10.4)],

$P_o = \propto_1 \emptyset_c f'_c (A_g - A_{st}) + \emptyset_s f_y A_{st}$ = $[0.797 \times 1 \times 35 \times \{(98980.035 - (6 \times 200)\}] \times 10^{-3} + [(1 \times 400 \times (6 \times 200)] \times 10^{-3} = \mathbf{3207.57\ kN}$

Series I (Short column): $\frac{\boldsymbol{kl_u}}{\boldsymbol{r}} = \frac{\mathbf{1 \times 1750}}{\mathbf{0.25 \times 355}}$ = 19.72 < 20.78 [CSA 2014 (10.15.2)]

Series II (Slender column): $\frac{kl_u}{r} = \frac{1 \times 2450}{0.25 \times 355}$ = 27.61 > 20.78 [CSA 2014 (10.15.2)]

<u>Longitudinal reinforcement ratio:</u>

According to CSA 2014 (10.9.3), minimum number of longitudinal reinforcing bars in circular columns shall be six.

Selecting 6-15M bars for all steel-RC specimens.

$\rho_f = \frac{A_{st}}{A_g} = \left[\frac{(6 \times 200)}{98980.035}\right] \times 100 = 1.21\ \% > 1\% < 8\%$ [CSA 2014 (10.9.1 & 10.9.2)]

<u>Spiral pitch and transverse reinforcement ratio:</u>

$D_c = [\{355 - (2 \times 27.5)\}] = 300\ mm$

$$A_c = \frac{3.1416 \times 300^2}{4} = 70686\ mm^2$$

According to CSA 2014 (10.9.4), the ratio of spiral reinforcement shall be not less than the value given by,

$\rho_{S_{req}} = 0.5 \left(\frac{A_g}{A_c} - 1\right)^{1.4} \frac{f'_c}{f_y} = 0.5 \left(\frac{98980.035}{70686} - 1\right)^{1.4} \frac{35}{400} = 0.0121 \times 10^2 = 1.21\%$

$$\rho_{s_{Req.}} = \frac{Volume\ of\ spiral}{Volume\ of\ core} = \frac{4A_{sp}}{D_c s_{Req.}}$$

$$s_{Req.} = \frac{4A_{sp}}{D_c \rho_{s_{Req.}}} = \frac{4 \times 100}{300 \times 0.0121} = 110.19\ mm = 110.19 - 11.3 = 98.89\ mm$$

To keep same spiral pitch as GFRP-RC specimen, selecting $s = 85\ mm$

$$\rho_{s_{Prov..}} = \frac{Volume\ of\ spiral}{Volume\ of\ core} = \frac{4A_{sp}}{D_c s_{Prov..}} = \frac{4 \times 100}{300 \times (85 + 11.3)} = 0.0138 \times 100 = 1.38\% > 1.21\%$$

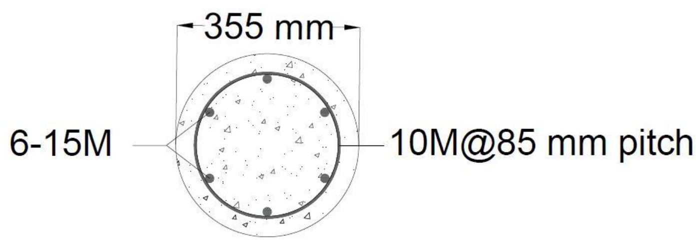

Steel-RC

APPENDIX C: FLEXURAL CAPACITY OF GFRP-RC SPECIMEN

Column dimension:

D = 355 mm; lu = 1,750 mm (Series I: Short columns); lu = 2,450 mm (Series II: Slender columns)

Cross-sectional properties:

D = 355 mm; $R = 177.5$ mm;

$A_g = \pi R^2 = 3.1416 \times 177.5^2 = 98980.035$ mm^2

Concrete properties:

f_c' = 35 MPa; ϕ_c = 1;

$E_c = 4500\sqrt{f_c'}$ = 26622 MPa;

α_1= 0.85 [ACI440.1R-15]

$\beta_1 = 0.85 - \frac{0.05(f'_c - 28)}{7} \geq 0.65 = 0.85 - \frac{0.05(35-28)}{7} = 0.80 \geq 0.65$ [ACI440.1R-15]

ε_{cu}= 0.003;

Longitudinal reinforcement: GFRP bars (No. 16)

6-No.16 GFRP bars; $\rho_f = 1.20$ %

f_{Fu} = 1558 MPa; ϕ_F = 1; E_F = 64 GPa; A_b = 199 mm^2; ε_{Fu} = 2.4%;

Transverse reinforcement: GFRP spiral (No. 10)

f_{Fu} = 667 MPa; ϕ_F = 1; E_F = 58 GPa; A_{sp} = 71 mm^2; ε_{Fu} = 1.14%;

Flexural capacity using simplified method proposed by Mousa et al. 2018:

$$D_r = \left[355 - \left\{2 \times (22.5 + 9.5 + \frac{15.9}{2}\right\}\right] = 275.1\ mm$$

$$d = \frac{D}{2} + \frac{D_r}{2} = \frac{355}{2} + \frac{275.1}{\pi} = 265.07\ mm$$

Distance from extreme tension bar to top compression fiber,

$d_{eff.} = 355 - (22.5 + 9.5 + \frac{15.9}{2}) = 315.05$ mm.

Balanced reinforced ratio,

$$\rho_{fb} = 0.85 \frac{f'_c}{f_{fb}} \frac{R^2(\theta_b - \sin\theta_b \cos\theta_b)}{Dd}$$

$$C_b = \left(\frac{\varepsilon_{cu}}{\varepsilon_{cu} + \varepsilon_{fb}}\right) d = \left(\frac{0.003}{0.003 + \frac{1558}{64000}}\right) \times 265.07 = 29.08\, mm$$

$$\theta_b = \cos^{-1}\left(1 - \frac{\beta_1 C_b}{R}\right) = \cos^{-1}\left(1 - \frac{0.8 \times 29.08}{177.5}\right) = 0.518\, rad = \frac{0.518 \times 180}{\pi} = 29.66^{\circ}$$

$$f_{fb} = \left(\frac{d - C_b}{d_{eff} - C_b}\right) f_{Fu} = \frac{(265.07 - 29.08)}{(315.05 - 29.08)} \times 1558 = \ \ 1285.70\, MPa$$

$$\rho_{fb} = \left[0.85 \times \frac{35}{1285.70} \times \left\{\frac{177.5^2 \times (0.518 - \sin 29.66^{\circ} \cos 29.66^{\circ})}{(355 \times 265.07)}\right\}\right] = 0.000682$$

$$A_{ft} = (3 \times 199) = 597\, mm^2$$

$$\rho_{ft} = \frac{A_{ft}}{Dd} = \frac{597}{355 \times 265.07} = 0.006153 > (1.4 \ \times 0.000682) = 0.000955$$

So, the section is compression controlled.

$$\theta = 2.14 \rho_f{}^{0.18} \left\{1.03 - 0.69 \left(\frac{f'_c}{E_F}\right)^{0.17}\right\} = 2.14 \times 1.2^{0.18} \left\{1.03 - 0.69 \left(\frac{35}{64}\right)^{0.17}\right\} = 0.901\, rad$$

$$= \frac{0.901 \times 180}{\pi} = 51.6^{\circ}$$

$$f_f = 0.85 \frac{f'_c}{A_{ft}} R^2(\theta - \sin\theta \cos\theta) = 0.85 \times \frac{35}{597} \times 177.5^2 (0.901$$

$$- \mathit{sin}\, 51.6^{\circ}\, \mathit{cos} 51.6^{\circ}) = \ 650.33\, MPa$$

$$\bar{y} = \frac{2R}{3} \left(\frac{\sin\theta^3}{\theta - \sin\theta \cos\theta}\right) = \frac{2 \times 177.5}{3} \left(\frac{\sin 51.6^3}{0.901 - \sin 51.6^{\circ} \times \cos 51.6^{\circ}}\right) = 137.51\, mm$$

$$M_n = A_{ft} f_f \left(\bar{y} + \frac{D_r}{\pi}\right) = 597 \times 650.33 \times \left(137.51 + \frac{275.1}{\pi}\right) 10^{-6} = \mathbf{87.38\ KN.m}$$